Towards the Optimization of the Accelerated Crucible Rotation Technique Applied to the Gradient Freeze Growth of Cadmium Zinc Telluride via the Finite Element Method

A DISSERTATION
SUBMITTED TO THE FACULTY OF THE GRADUATE SCHOOL
OF THE UNIVERSITY OF MINNESOTA
BY

Mia Shakti Divecha

IN PARTIAL FULFILLMENT OF THE REQUIREMENTS
FOR THE DEGREE OF
DOCTOR OF PHILOSOPHY

Jeffrey J. Derby

December, 2017

Acknowledgements

First and foremost, I am forever indebted to my adviser, Professor Jeffrey Derby, without whom this journey or document would not have been possible. From the early days, Jeff has been unwavering in his optimism and encouragement of my work. He has not only taught me a great deal about the fundamentals of crystal growth and the many fascinating, nonlinear phenomena that accompany it, but also about giving strong presentations, developing lifelong relationships, and writing (which is still a work in progress!). Jeff allowed me the space and freedom to explore my research and make it completely my own, while pushing me to take risks and dive into areas I feel uncomfortable. He has created a space where I have developed not only strong technical skills but also confidence and a voice. When I think back to who I was upon graduating college, I am appalled at how little I knew. While I know I have so much more to still learn, I am a far better researcher and engineer because of Jeff. I am grateful for my relationship with him and his wife Ann, and I look forward to a lifelong connection.

Much of this work would not have been possible without the advice, support, help and conversations with my group mates: Yutao Tao, Jeff Peterson, Kerry Wang, Chang Zhang, John Roerig, and Scott Dossa. In particular, I must credit much of my early development to Jeff Peterson, with whom I spent many days discussing the fundamentals of thermodynamics and transport phenomena. He enthusiastically welcomed all of my questions in the early days, and patiently explained many of the details of our code and inner workings to me. He was kind enough to help prepare me for my candidacy exam, and I have many fond memories sitting in the office late discussing fun and challenging questions. I have also enjoyed many memories traveling with the group, particularly with Jeff Peterson and Kerry Wang, to places like Montana, Belgium (and Iceland!), Berkeley, Japan, and Santa Fe. It's hard to find a group you can travel with and I have

enjoyed exploring these places with you all.

I am also indebted to my classmates with whom I have slogged through coursework and candidacy exams. I truly believe I would not have passed my courses without their help. In particular, I am grateful to Mike Harris, Michail Vlysidis, Andrew Allman, Ron Lewis, Peter Schmidt, and many more to name. These are some of the smartest people I know, and I'm lucky to call them friends. In particular, my friendship with Mike Harris and his wife Beth has been one of the highlights of graduate school and I look forward to a lifelong friendship with them and many others.

I would be remiss to not mention the many outstanding faculty members here who educated, guided, and supported me throughout this journey. I have a lifelong respect and admiration for Professor Victor Barocas, with whom this journey really started. Victor welcomed me into his group early in my first year, and then graciously and generously helped me transition to a new group when I learned biomechanics was not for me. I will never count those months as wasted because I got to see what true leadership and mentorship in academia really means. Professor Eray Aydil's thermodynamics class was one of the best courses I've ever taken, and I was lucky to have TA'd the course the following year. Eray encouraged and supported opportunities for me to teach and I have enjoyed many conversations with him regarding career and triathlons since. Professor Prodromos Daoutidis' numerical methods class confirmed my love for math, and I will miss saying hello to him daily in the hallways. Most recently, I've had the pleasure of working with Professor Kevin Dorfman, for whom I have a profound respect. I am grateful for the opportunity to teach in my last semester here and for the various conversations we have had regarding academia. But it was in Professor Satish Kumar's fluid mechanics course that I really found my passion. The thoughtfulness and care with which Satish approached the class created a learning environment unlike any other. I finally felt like I understood fluid mechanics, and thus could appreciate it. It was in his class that sparked a lifelong love of these incredible phenomena, and I knew I needed my career to involve fluid mechanics in some capacity. I am enthralled with his work and, if I had ambitions to be a professor, it would be in his area of expertise. Lastly, I must thank the Chair of CEMS, Professor Dan Frisbie, who has always welcomed me into his office to discuss items pertaining to the department. I appreciate his constant support of student activities and I know the department will thrive under his leadership.

I am very proud to call myself a CEMS alum, and I look forward to being an active, connected alum in the years to come.

This department, along with my and many others' experiences here would not have been the same without the constant support, joy, and infrastructure provided by Julie Prince and Teresa Brehdal. Not only have they provided advice, comfort, and support for me during my PhD, they also have cultivated a strong community of respect, hard work, and of course good fun. They are the glue that holds this department together, and I feel fortunate to have spent my time under their tenure.

I must thank many friends and family whom have helped make my transition to Minnesota smooth and fun - from friends like Percia Safar, Showly Wang, Sarah Bindman, Laurie Russell, Justine Hong, Nupur Kantamneni, and more for visiting me in the dead of winter; to family like Jessie Westlund, Andy Westlund, Kelly Merchant, Sahil Merchant, Mitch Johnson, Vicki Johnson, Julie Westlund, John Westlund, Kurt Johnson, Wendy Johnson, and more for making Minnesota really feel like home for me. I am grateful in particular to my sister Zai who has made many frequent trips here to visit, and who has always been my number one fan.

It is my parents who truly deserve to take all the credit. From an early age, my mother recognized my aptitude for math, and promoted and supported my love for it. My father instilled a love for questioning the world around me through a scientific lens, which has prepared me to be the engineer I am today. They have provided me with unconditional love, support, help, and guidance through many rocky transitions, and I would not be the person I am today without them.

Lastly, none of this would be possible without my partner Nima. From the time when I had just declared my major as chemical engineering, he has been my biggest cheerleader. He sees potential in me when I do not see it myself, he picks me up when I am down, and he pushes me to be a better engineer, researcher, and person. He moved across the country, leaving his work, his family, and his friends to support me and my education. I feel so lucky to be in a partnership with someone that recognizes me and my career as an equal priority. I look forward to a lifetime of pushing and supporting each other to be the best we can be.

Dedication

To my husband, Nima, and my parents, Diana and Arjun.

Abstract

Cadmium zinc telluride (CZT) is a semiconductor used for gamma ray detection in applications ranging from nuclear weapons monitoring to medical imaging. The production of CZT via the vertical gradient freeze (VGF) method is plagued by tellurium rich inclusions in the crystal that significantly decrease the detector performance. The accelerated crucible rotation technique (ACRT) is a promising approach for improving the production of detector-grade CZT crystals. ACRT, which repeatedly spins the crucible at varying rotation rates, was designed by Scheel and Schulz Du-Bois in the early 1970s as a means of controlling nucleation of new grains and reducing the size and density of inclusions. Despite the many improvements made in crystalline quality with the application of ACRT, little is understood with regard to how ACRT works to reduce inclusions, and few guidelines exist to help aid the selection of rotation schedules.

Toward these ends, we have developed a realistic, comprehensive model based on the experimental set up at Washington State University (WSU). Finite-element methods are employed to solve the coupled phenomena of fluid mechanics, heat transfer, and solute transport in the VGF-ACRT system. We track the transport of tellurium and incorporate its thermodynamic effects on solidification phenomena. We show for the first time that the segregation of tellurium during growth drives constitutional supercooling. This supercooling is an indicator that a morphological instability has the potential to form and yield inclusions. Through a series of transient calculations, we aim to reduce the amount of supercooling via assessment of the transport phenomena and solidification dynamics. We present a thermodynamically based metric, which employs the classic instability criterion developed by Mullins and Sekerka, that represents the effect of ACRT on the stability along the solid-liquid interface. This metric is utilized for the comparison and optimization of rotation schedules. We find that, in contrast to conventional wisdom, slower rotation schedules that promote disruption of the solute field without disruption of the local interface velocities are found to be most favorable for the WSU system. Preliminary experimental evidence is presented that supports these findings.

Contents

List of Tables

List of Figures

Chapter 1

Introduction

1.1 Cadmium zinc telluride as a gamma ray detector material

In 2009, the president of the United States declared that the non-proliferation of nuclear weapons is a top priority for the safety and security of the country and its inhabitants [6]. An important component of this declaration is the commitment to develop high-resolution gamma detector materials that can detect and block the transmission of nuclear material into the country [7]. Detector materials also have applications in a variety of medical imaging device, such as single photon emission computed tomography myocardial perfusion imaging for the non-invasive diagnosis of coronary artery disease [8–10]. Together, these applications motivate a need for high volume, low cost gamma detector materials.

Scintillator materials such as sodium iodide and cesium iodide are commonly used for gamma detection. However, many of these materials suffer from low energy resolutions. Cadmium zinc telluride (CZT) is a promising semiconductor for gamma detection due to its wide band gap, high resistivity, and ability to operate at room temperature [11–17]. CZT is generally grown via the Bridgman method [18, 19], which directionally solidifies monocrystalline material by translating an ampoule through a stationary temperature gradient. However, CZT is difficult to grow, and yields are typically very low. Thus, with the current growth methods, CZT is still too expensive for widespread adoption.

Of the many problems that arise during the Bridgman growth of CZT, the most vexing is arguably the propensity of the crystal to exhibit micron-sized tellurium particles called inclusions [20,21]. These act as electron traps that are detrimental to the device's performance. There is evidence that the application of repeated crucible rotation via the accelerated crucible rotation technique (ACRT) during growth can ameliorate these inclusions [1], however its exact mechanism is unknown. Moreover, there are few guidelines to aid selection of optimal rotation schedules, e.g., how fast to rotate and for how long. Through the use of computational models, this work aims to provide fundamental insight into the reduction of inclusions via ACRT and the transport mechanisms that accompany the process.

1.2 The Bridgman method for growth of CZT

The Bridgman method begins with a charge of material sealed in an ampoule that is heated above the material's melting point to a molten state. The ampoule is then drawn axially downwards through a stationary furnace gradient, which encourages a single nucleation event and subsequent directional solidification of material in the axial direction. The Bridgman method is favored for its fast growth rates (on the order of 1 mm/hr) over other techniques. The vertical gradient freeze method (VGF) is a variation of the Bridgman method [22], where the ampoule is stationary and a dynamically changing furnace temperature profile is applied that encourages the directional solidification of material. This is depicted schematically in Figure 1.1.

During directional solidification, species such as zinc and tellurium segregate to form inhomogeneous distributions within the crystal. Zinc, for example, has a segregation coefficient that is greater than one. Subsequently, zinc is preferentially incorporated into the solid, resulting in a depletion boundary layer in the melt during solidification. The effect is compounded as growth continues, such that the final boule exhibits significant axial (and radial) variations in the zinc composition. This is shown experimentally in Figure 1.2 for the VGF growth of CZT. This inhomogeneity means that material cut from the first-to-freeze region will have different electronic properties than last-to-freeze material. While the growth of CZT and the effects of segregation are well understood [23–31], particularly with respect to zinc segregation [32–37], the segregation

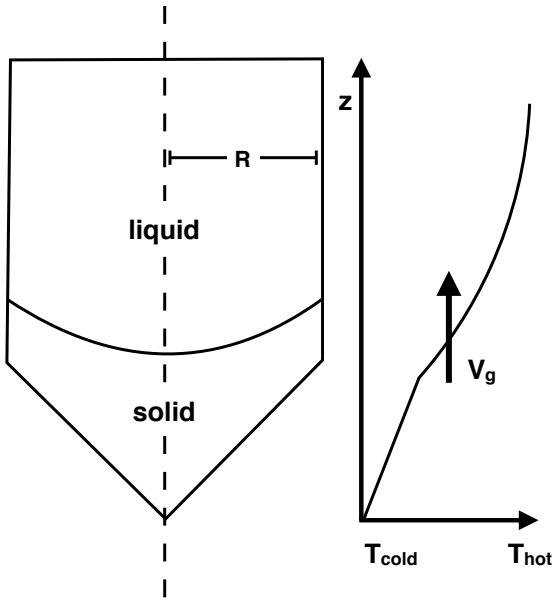

Figure 1.1: Schematic of the gradient freeze method (VGF), which is a variation on the Bridgman method.

of tellurium is often overlooked.

Tellurium has a segregation coefficient that is less than one, meaning material is rejected into the melt during growth. This creates a concentrated boundary layer in the melt, depicted schematically in the left of Figure 1.3. While this affects the composition of the solid, segregation can also cause constitutional supercooling via the following mechanism: the liquidus temperature, depicted schematically in the right of Figure 1.3, is a strong function of the composition. In the presence of large concentration gradients, the corresponding liquidus temperature will be adjusted. Under certain conditions, if the local temperature determined by the thermal field is lower than the composition-dependent liquidus temperature, the liquid is considered supercooled. This comparison of thermal gradients is depicted schematically in the bottom of Figure 1.3. The presence of constitutional supercooling is problematic, as it can cause problems with solidification at the solid-liquid interface.

Many simulations of the directional solidification methods exhibit a planar morphology of the solid-liquid interface, with some concavity depending on the thermal field and material properties [38]. However, under conditions of constitutional supercooling, the

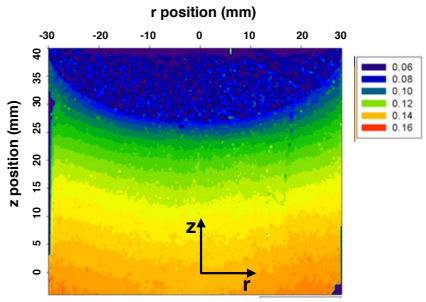

Figure 1.2: Photoluminescence mapping of zinc distribution in CZT grown via VGF. The lower zinc concentration (blue color) corresponds to the last to freeze and the higher zinc concentration (red color) to the first to freeze. The scale corresponds to the fraction of cadmium sites occupied by zinc. From [1].

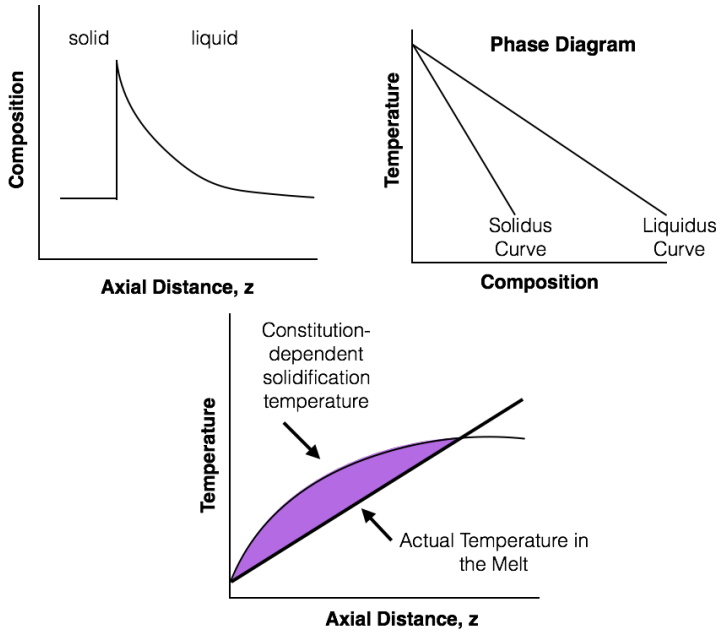

Figure 1.3: Left: schematic of a concentration boundary layer that arises due to segregation during solidification. Right: comparison of the composition-dependent solidification temperature to the local temperature. The shaded purple indicates a region of supercooled material.

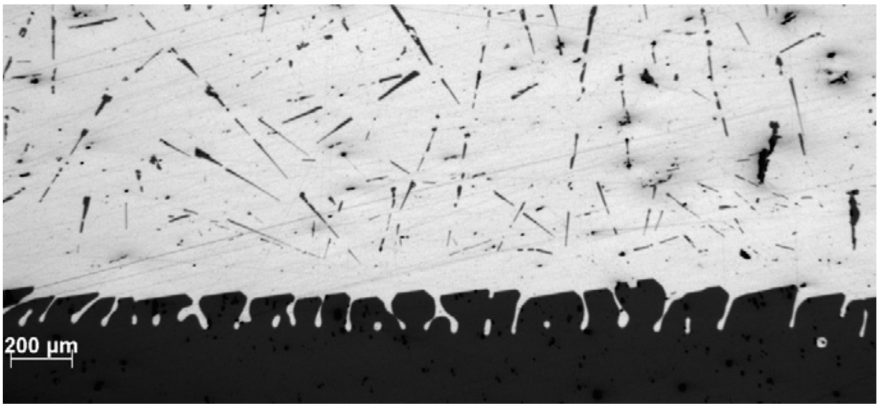

Figure 1.4: Morphology of the growth interface of CZT via the traveling heater method depicting a cellular morphology. The space in between the cells traps liquid to form inclusions. From [2]

interface is known to take on a cellular morphology [39], as shown in Figure 1.4 for the growth of CZT via the traveling heater method [2,40]. Over time, these cells can deepen and the space between them can trap and shed droplets of tellurium rich liquid [41,42]. These droplets solidify into the micron-sized inclusions that are deleterious to detector performance [43].

Conventional wisdom postulates that a cellular morphology will form if the following classical supercooling criterion developed by Tiller et al. [44] is satisfied:

$$G - mG_c < 0, \tag{1.1}$$

where G, m, and G_c represent the thermal gradient in the liquid, the local slope of the liquidus curve, and the concentration gradient in the liquid, respectively. In short, this value compares the gradients identified in the bottom of Figure 1.3 to determine if supercooling will occur.

1.3 The accelerated crucible rotation technique as a means of improving CZT

The accelerated crucible rotation technique (ACRT) is postulated to reduce the size and density of tellurium inclusions via adjustment of the local thermal and solutal gradients. The idea is that repeated acceleration and deceleration of the crucible during growth will enhance the convection within the melt, thus enhancing the solute transport. The adjusted concentration gradients can delay or prevent the accumulation of supercooled material via Equation 1.1, thus preventing an instability and subsequent inclusion formation.

First developed in 1972 by Hans J. Scheel, ACRT was proposed as a method to reduce unwanted nucleation events, minimize constitutional supercooling, increase stable growth rates, and homogenize the temperature and concentration fields during growth of $GdAlO_3$ [45]. Crystals grown under ACRT conditions yielded larger single crystalline regions and achieved higher growth rates [45]. With these promising results in hand, Scheel's colleague Erich O. Schulz-DuBois identified the relevant rotational fluid physics that govern the ACRT system, including Taylor-Görtler instabilities and Ekman flow (to be discussed in Chapter 5), and how these dominate over the underlying natural convection [46]. Shortly after, Wald and Bell applied the concept of accelerated rotation to the growth of CdTe under the traveling heater method [47]. While the positive effects were described as modest given the strong underlying natural convection, the growth rates were increased by a factor of two. These results were corroborated by Bloedner and Gille over a decade later [48].

Starting from 1984 through present day, Capper and coworkers have published a series of papers [49–55] which detail in-depth experimental and theoretical analyses of ACRT applied to the Bridgman growth of II-VI materials. Along with much experimental work outlining the beneficial effects of ACRT on compositional uniformity and crystalline quality [49,50], Capper was also the first to make concrete recommendations for the design of rotation schedules [52]. Capper's work will be discussed at length in Chapter 7.

In 1999 Lan and Chian performed the first two-dimensional numerical simulation of ACRT applied to the traveling heater method growth of GaAs [56]. This model

included the nonlinear interdependence of the flow and thermal field, and included the Boussinesq approximation to the Navier-Stokes equation that allowed for temperature dependent density differences. The impact of steady and accelerated rotation on the interface shape and local growth velocities were analyzed. At the same time, Yeckel and Derby performed a series of calculations assessing the impact of steady rotation on the zinc composition field during Bridgman growth of CZT [57]. The steady rotation was found to have minimal, if not deleterious, effects on the zinc compositional field and constitutional supercooling. Shortly after, Yeckel and Derby published a series of comprehensive simulations with ACRT applied to the Bridgman growth of CZT [58], which identified the impact of rotation on the zinc distribution within the melt. The periodic Ekman flows and Taylor-Görtler vortices homogenized the zinc composition in the melt, and the redistributed thermal fields adjusted the local interface shape and velocities during the transient simulations.

In 2000, Liu et al. published a series of computational studies of ACRT applied to the Bridgman growth of II-VI materials [59, 60]; however, their computations neglected natural convection, which Yeckel and Derby [61] determined to be crucial to the accurate representation of the physics.

Additional simulations followed that aimed at further optimization and fine-tuning of the process conditions. Work by Moon et al. [62], Liu et al. [63], Juncheng [64], Bellmann et al. [65], and Yin et al. [66, 67] attempted to optimize rotation schedules. Various rotation schedules were tested, e.g., trapezoidal versus sawtooth, symmetric versus asymmetric, pulse waves, etc., and were compared via qualitative assessment of the streamlines and concentration gradients. Some authors [64, 65, 67] used local concentration gradients to assess the degree of homogenization and others [62, 63] used the local interface deflection or interface velocities to understand the impact of rotation. While all studies resulted in interesting insights, overwhelming agreement was not found between studies. Simultaneously, applied experimental work like that done by Distanov and Kirdyashkin [68], Wang et al. [21,69], and Datta et al. [1,70] highlighted the positive impact of rotation on detector performance metrics such as the mobility-lifetime product, resistivity, and inclusion densities. However, due to limited resources and length of experiments, none of these authors were able to do a systematic comparison of multiple rotation schedules to assess the influence of varying schedules.

The prior experimental studies have demonstrated the effectiveness of ACRT to improve material quality, and the many computational models have elucidated the relevant rotational fluid dynamic phenomena that occur in the system. While previous authors included most the relevant physics into their models, none thus far have incorporated the thermodynamic effects of tellurium, which we believe is important for the reduction of inclusions. Additionally, few have provided concrete recommendations regarding rotation schedule selection, and most have relied solely on qualitative measures to compare rotation schedules. We address these shortcomings via a comprehensive model that incorporates flow, heat, and solute transport of tellurium within the system. We propose a thermodynamically based metric that is used to quantitatively compare rotation schedules, and we employ this metric to provide insight into many of the factors influencing the growth of CZT under ACRT.

This thesis is an amalgam of the many interesting factors that influence the VGF-ACRT system. Each chapter addresses a new component of the system variables, and subsequently may read as stand-alone. Regardless, it is our hope that by the end, new insight and understanding is gained into the VGF-ACRT system. We begin in Chapter 2 with a description of the geometry, relevant equations and boundary conditions that govern the physics of the problem. Chapter 3 briefly describes the numerical method employed by the code (Cats2D). In Chapter 4, a base case result for a VGF system without rotation is be presented in order to identify the underlying physics and introduce how to interpret contour plots. In Chapter 5, we discuss the relevant rotational fluid dynamic phenomena that arise during rotation through a base case simulation of VGF with applied rotation. Chapter 6 identifies the impact that tellurium has on constitutional supercooling under both steady conditions and ACRT. A thermodynamically-based metric is also proposed that will be used as an assessment tool for rotation schedule comparison. Next, the recommendations put forth by Capper in his 1988 paper [51] are analyzed in Chapter 7, paying particular attention to how his recommendations affect supercooling. In an effort to provide more insight into rotation schedule selection, a statistical analysis of rotation schedules is performed in Chapter 8 that identify the influence of schedule parameters on the interface stability. Then, we investigate the influence of differing furnace profiles on the solidification dynamics in Chapter 9. The model and the metric are compared to experimental results in Chapter

10 for model validation purposes. Lastly, a short summary and directions for future work are presented in Chapter 11.

Chapter 2

Model Development

There are additional challenges to the modeling of the vertical gradient freeze growth (VGF) method with applied rotation compared to classic crystal growth processes. Whereas in many crystal growth systems a quasi-steady state approximation is valid, the time-dependent nature of rotation necessitates transient simulations to be performed. The addition of tellurium in the model requires faithful representation of the thermodynamics, which will be accomplished by incorporating phase diagram information into the system. The ensuing chapter describes the governing equations and boundary conditions that specify the energy, momentum, and solute transport within the VGF method with the accelerated crucible rotation technique (ACRT).

The geometry, physical properties, and thermal boundary conditions are based on the experimental set up in Professor Kelvin Lynn's group at Washington State University (WSU). Specifications of the WSU ampoule and charge are shown in Figure 2.1. The cylindrical ampoule has an inner diameter of 65mm, a wall thickness of 2 mm, and a full length of approximately 40 cm. Material is placed in the ampoule such that it fills only a fraction of the ampoule. A graphite plug is placed at the top of the charge that is assumed to completely wet the liquid upon melting. Thus, the scope of the model is limited to this region, with a total height of 8.5 cm. The ampoule is placed on a pedestal which rests inside a furnace, over which 43 furnace zones dynamically adjust to encourage the directional solidification of material. A representation of the furnace set up is shown in figure 2.2. The pedestal is connected to a motor that can drive rotation around the z axis.

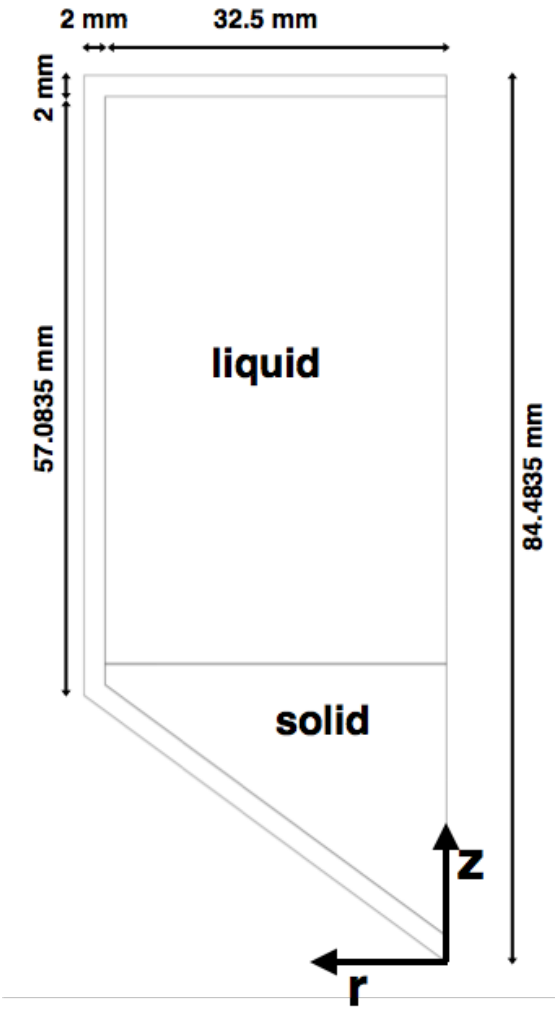

Figure 2.1: Schematic of ampoule regions with relevant dimensions. Half the dimension is shown due to assumed axisymmetry.

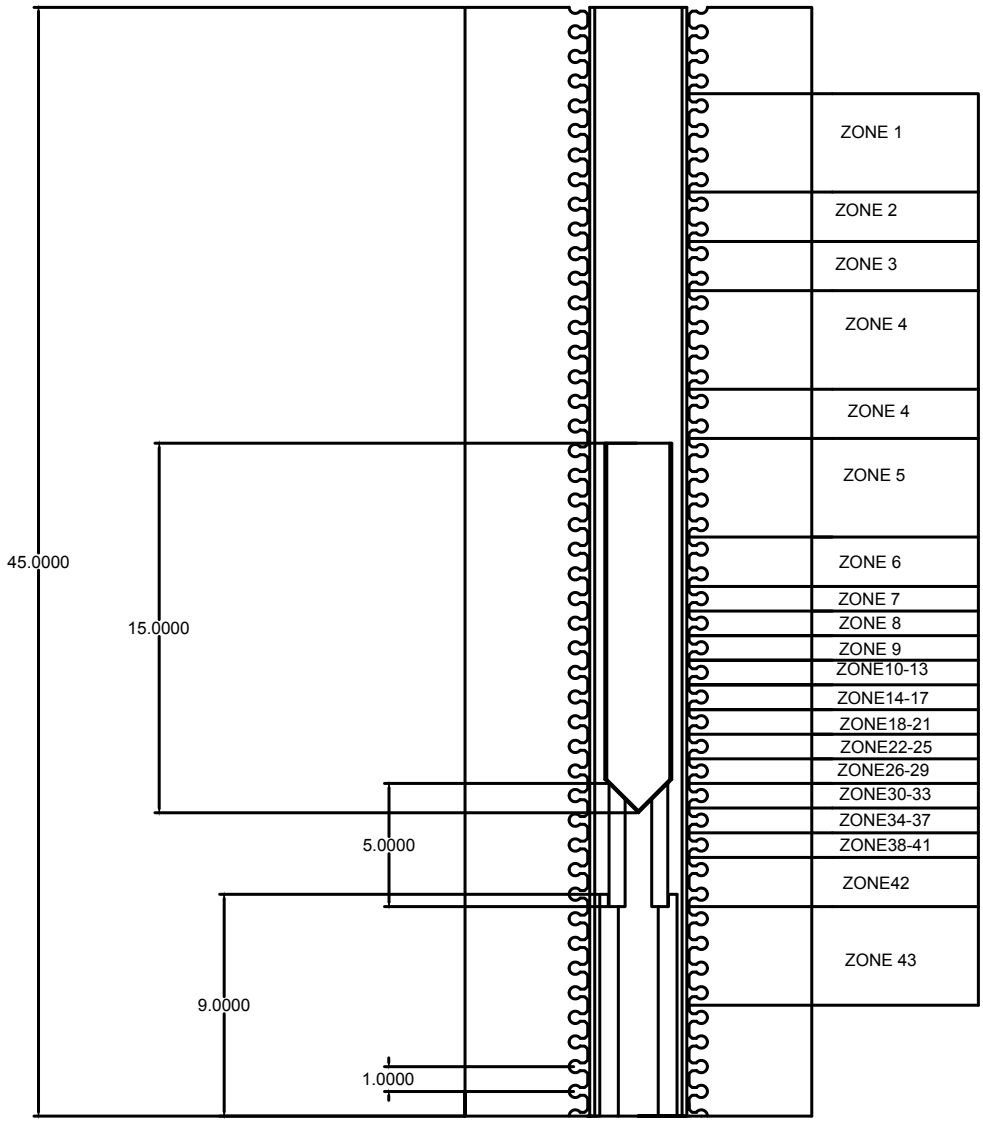

Figure 2.2: Schematic of furnace set up. A 43-zone furnace is dynamically controlled via set points along the furnace wall. All dimensions are shown in inches.

The problem is specified in cylindrical coordinates (r,θ,z), with assumed symmetry in the azimuthal direction. This allows for half the domain to be solved in two dimensions, which decreases the computational load and reduces the coordinate system to r and z only. In the ensuing equations, r and z are defined to be fixed to the ampoule, thus the governing equations are solved in reference to the lab frame.

2.1 Equations and boundary conditions

2.1.1 Field equations

Unsteady heat transfer is solved within all material regions as governed by the conservation of energy. While this and other governing equations can be presented in dimensionless form which results in a nice discussion of dimensionless groups, we choose to present them in dimensional form.

In order to solve for the temperature field, $T(r, z)$, in the domain, conservation of energy is applied to all material regions:

$$\rho_i c_{p,i} \left(\frac{\partial T}{\partial t} + \mathbf{u} \cdot \nabla T \right) = k_i \nabla^2 T, \ i = l, \tag{2.1}$$

$$\rho_i c_{p,i} \frac{\partial T}{\partial t} = k_i \nabla^2 T, \ i = s, a, \tag{2.2}$$

where ρ_i, $c_{p,i}$, and k_i represent the density, constant pressure heat capacity, and thermal conductivity in region i, respectively. The subscript i indicates the phase in which the equation is relevant, with l, s, and a corresponding to the liquid, solid, and ampoule, respectively. While convective and diffusive heat transport exists in the liquid, only diffusive heat transport occurs in the solid and the ampoule. The lowercase t corresponds to time, the vector $\mathbf{u}$ represents the velocity field, and the gradient operator $\nabla \equiv (\partial/\partial r)\mathbf{e_r} + (\partial/\partial z)\mathbf{e_z}$ where $\mathbf{e_r}$ and $\mathbf{e_z}$ are the unit vectors in the r and z directions.

The continuity and Navier-Stokes equations govern the velocity and pressure field in the liquid, represented by the vector $\mathbf{u}(r, z)$ and the scalar $p(r, z)$ respectively. The equations below represent the conservation of mass and momentum for an incompressible fluid with the Boussinesq approximation. This approximation allows the Navier-Stokes

equations to be coupled with the energy equation to account for temperature dependent density differences:

$$\nabla \cdot \mathbf{u} = 0 \tag{2.3}$$

$$\rho_l \left(\frac{\partial \mathbf{u}}{\partial t} + \mathbf{u} \cdot \nabla \mathbf{u} \right) = \nabla \cdot \mathbf{T} + \rho_l \left[1 + \beta (T_{mp} - T(r,z)) \right] \mathbf{g}. \tag{2.4}$$

In the above equation, $\mathbf{T}$ represents the total stress tensor for a Newtonian fluid, defined by:

$$\mathbf{T} = -p\mathbf{I} + \mu \left(\nabla \mathbf{u} + (\nabla \mathbf{u})^T \right), \tag{2.5}$$

where $\mathbf{I}$ is the identity tensor and μ is the dynamic viscosity of the liquid. The coefficient of thermal expansion is represented by β, and a reference temperature from which the density deviates is defined by T_{mp}, and is chosen to be the melting point of CZT. The gravity vector is represented by $\mathbf{g}$.

In order to track the varying composition of tellurium in the melt, conservation of species for a dilute binary mixture is applied to solve for $C(r,z)$, the concentration of tellurium in the melt:

$$\frac{\partial C}{\partial t} + \mathbf{u} \cdot \nabla C = D \nabla^2 C. \tag{2.6}$$

In the above equation, D represents the diffusion coefficient of tellurium in the liquid. Solid-state diffusion of tellurium is neglected. This is expanded upon in section 2.1.3.

2.1.2 Boundary conditions

A representative furnace profile is applied to the system as a simplified radiation heat transfer boundary condition along the outer ampoule side walls. This condition is formulated in the following manner,

$$-k_a \mathbf{n} \cdot \nabla T = \sigma \epsilon \left(T(r,z)^4 - T_a^4 \right), \tag{2.7}$$

where σ and ϵ represent the Stefan-Boltzmann constant and the emissivity of the ampoule, respectively. Heat is exchanged between the ampoule wall and furnace heating elements at an effective temperature T_a, which has been formulated via view factors with an enclosure method. More details on the functional form of T_a are presented in section 2.2. The unit normal vector, $\mathbf{n}$, points out of the ampoule region. At the centerline, the no-flux boundary condition is applied in order to satisfy the symmetry assumption:

$$-k_i \mathbf{n} \cdot \nabla T = 0. \tag{2.8}$$

Across the solidification interface, latent heat is released as a function of the growth rate and captured by the following flux balance across the interface:

$$k_l \mathbf{n} \cdot \nabla T|_l - k_s \mathbf{n} \cdot \nabla T|_s = \rho_l \Delta H \mathbf{n} \cdot \dot{\mathbf{x}}, \tag{2.9}$$

where ΔH is the latent heat of fusion, and $\dot{\mathbf{x}}$ is the local instantaneous growth velocity of the interface which is computed from the local motion of the nodes along the interface (more on this in Chapter 3). This value can deviate from the applied translation rate of V_{pull} in a transient simulation due to a lag in heat transfer.

For the flow, no-slip and no-penetration boundary conditions are applied on all surfaces in contact with the ampoule wall. Specifically, this corresponds to the following:

$$\mathbf{t} \cdot \mathbf{u} = 0 \tag{2.10}$$

$$\mathbf{n} \cdot \mathbf{u} = 0 \tag{2.11}$$

where $\mathbf{t}$ corresponds to the unit tangent vector defined by the boundary of the domain.

Azimuthal flow is specified as a no-slip condition in the θ direction along liquid-ampoule surfaces. The azimuthal velocity must equal the time-dependent rotation rate, $\omega(t)$, that is specified by the user:

$$\mathbf{e}_\theta \cdot \mathbf{u} = \omega(t), \tag{2.12}$$

where $\mathbf{e}_\theta$ is the unit vector that points in the θ direction.

2.1.3 Segregation and solidification

Of particular interest is the segregation of tellurium within the system. However, before diving into a discussion on the appropriate boundary conditions, a discussion on the phase diagram of CZT is warranted.

The stoichiometry of CZT is denoted by $Cd_{1-x}Zn_xTe$, where x represents the percentage of cadmium sites occupied by zinc atoms. The phase diagram for varying amounts of tellurium is presented at four distinct zinc compositions in Figures 2.3-2.6. Figure 2.3 shows the phase diagram for CdTe (i.e., no zinc), where the open circles represent the solidus line and the circles with a line through it represent the liquidus line, taken from [3]. The liquidus line has a negative slope, indicating material will be rejected during solidification. This is reflected in the segregation coefficient, $k_p = C_s/C_l < 1$, where C_s and C_l are the concentrations of tellurium in the solid and the liquid, respectively. The solidus line, which is blown up 1250x, has as protrusion that fractionally increases the composition of solidification.

CZT is commonly grown from an excess of Te, as it has been found to improve the resistivity [31, 71]. Material solidified from a tellurium-rich melt will also contain excess tellurium. As this solid cools, it will become supersaturated with tellurium as a consequence of the retrograde solidus line, leading to solid-state precipitation. The resulting nanometer size particles are called precipitates and are commonly found in CZT boules. While both precipitates and inclusions have deleterious effects on detector performance, they have fundamentally different origins. Moreover, precipitates are believed to be the inevitable consequence of a thermodynamic effect, while inclusions may be able to be controlled via adjustment of the growth conditions.

Increasing the zinc composition has a negligible impact on the liquidus line and a moderate impact on the solidus line, particularly in the homogeneity region [72–76]. The homogeneity region is the range over which the solid phase can exist out of its stoichiometric ratio without forming a second phase, and is shown for x=0.05, x=0.10, and x=0.15 in Figures 2.4, 2.5, and 2.6, respectively.

The maximum solidus concentration within the homogeneity region in the case of zero zinc is 50.014%. As the zinc is increased to x=0.05, the solidius line extends to a larger maximum value of 50.015%. This effect continues; as zinc is increased to x=0.10, the solidus line extends further to a maximum tellurium composition of 50.05%.

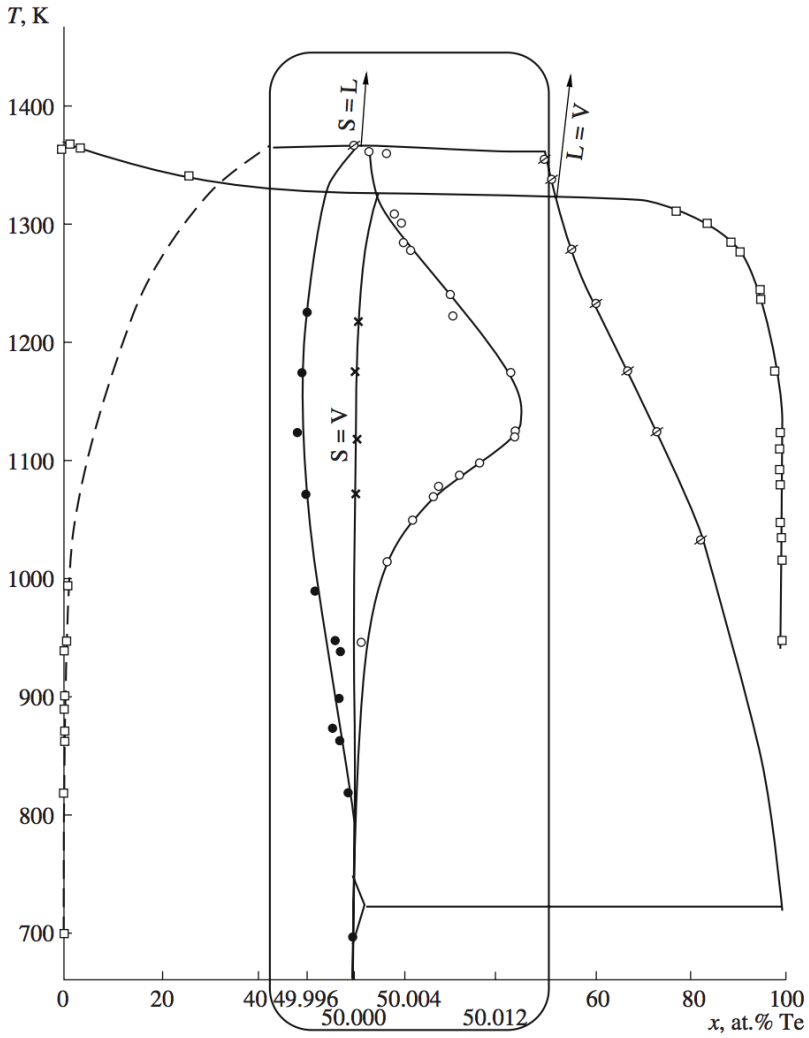

Figure 2.3: Phase diagram for the Cd-Te binary system. The homogeneity region is expanded for clarity. From [3].

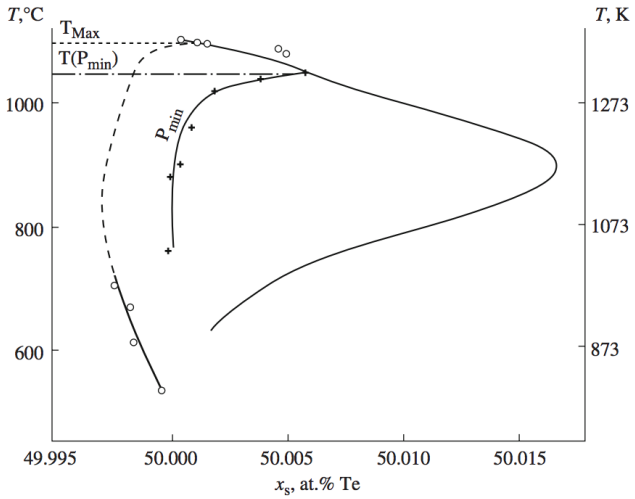

Figure 2.4: Homogeneity region for the $Cd_{0.95}Zn_{0.05}Te$ system. From [3].

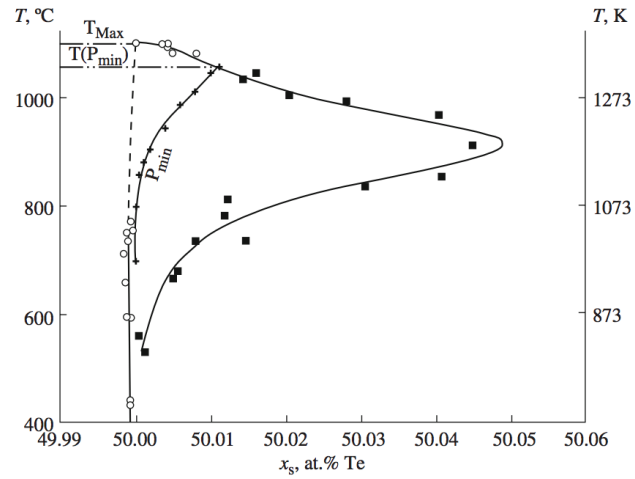

Figure 2.5: Homogeneity region for the $Cd_{0.90}Zn_{0.10}Te$ system. From [3].

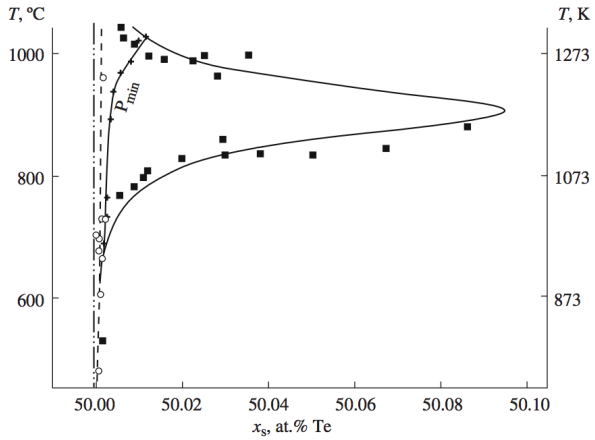

Figure 2.6: Homogeneity region for the $Cd_{0.85}Zn_{0.15}Te$ system. From [3].

At x=0.15, the maximum tellurium composition is 50.09%. As the zinc composition increases, material is solidified at a higher tellurium composition.

Although an understanding of these physics is important to reflect the realistic behavior, two assumptions are made while implementing the phase diagram data into the model. First, as zinc has little impact on the liquidus line, its effects are neglected when calculating a constitutional-dependent melting point. A fourth order polynomial fit to the liquidus line data of CdTe from [77] via the following equation:

$$T_{mp}(C) = A_1 C^4 + A_2 C^3 + A_3 C^2 + A_4 C + A_5, \tag{2.13}$$

where the coefficients A_1 through A_5 are defined in Table 4.2. This function is incorporated into the model via the following constraint

$$T_{int} = T_{mp}(C), \tag{2.14}$$

which requires that the interface adjust its location to conform to the local composition-dependent melting point. Not only does this formulation allow for the accurate computation of the solid-liquid interface, but it also allows for the assessment of thermodynamic

supercooling in the liquid phase away from the interface. With the composition of tellurium known in all locations in the melt, a simple comparison of local temperatures, T_{local} to calculated composition-dependent melting point temperatures can determine the location and severity of supercooling. This magnitude of supercooling, ΔT can be calculated via the following expression:

$$\Delta T = T_{local} - T_{mp}(C). \tag{2.15}$$

For all intents and purposes, this value is equivalent to the classic constitutional supercooling criterion developed by Tiller et al. [44] discussed in Chapter 1. Taking the spatial derivative of Equation 2.15 with an assumed linear liquidus form yields the exact form of the classic criterion shown in Equation 1.1.

The second assumption is that, although zinc has a measurable impact on the homogeneity region of the phase diagram, tellurium is assumed to solidify at 50%. This neglects any impact zinc has on the segregation coefficient, and removes the need to solve for diffusion of tellurium within the solid. Thus segregation of tellurium is incorporated by the following species flux balance across the solidification interface:

$$D\mathbf{n} \cdot \nabla C = -C(1 - k_p)\mathbf{n} \cdot \dot{\mathbf{x}}. \tag{2.16}$$

The flux of tellurium generated by segregation is linearly dependent on the interface growth velocity, $\dot{\mathbf{x}}$.

Lastly, at all ampoule walls and the centerline, a no-flux condition is applied that ensures mass is conserved within the system:

$$D\mathbf{n} \cdot \nabla C = 0 \tag{2.17}$$

2.2 Furnace profile

A realistic furnace profile is required to ensure the accurate representation of heat transfer within the system. A series of furnace profiling experiments described in Appendix A was performed to develop a functional form for T_a, the effective furnace temperature described in Equation 2.7. T_a depends not only on space but also on time since it is

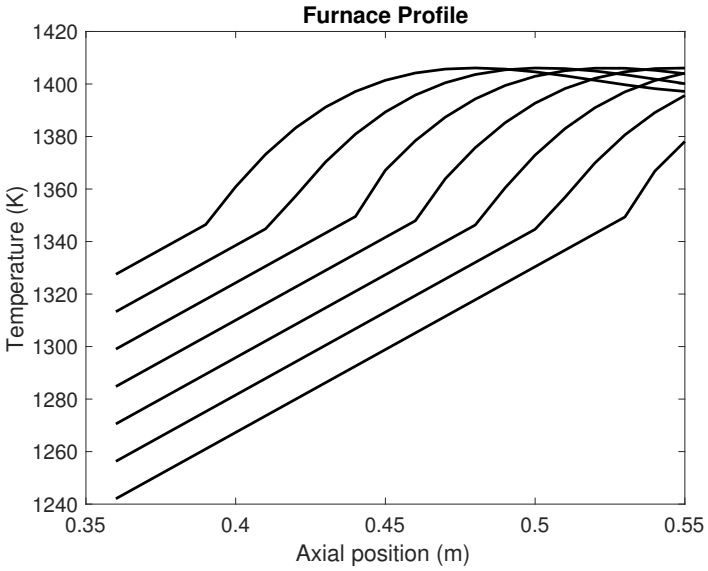

Figure 2.7: Version 2 of the furnace profile applied to the outer ampoule wall as a radiation boundary condition. The function corresponds to equation 2.18

.

translated in the axial direction at an applied translation rate of V_{pull}. The equation is presented below and graphed in figure 2.7.

$$T_a(z,t) = \begin{cases} m_1\left(z - (z_1 + tV_{pull})\right) + T_1 & 0 \leq z < z_1 + tV_{pull} \\ m_2\left(z - (z_1 + tV_{pull})\right)^3 + m_3\left(z - (z_1 + tV_{pull})\right)^2 & \\ +m_4\left(z - (z_1 + tV_{pull})\right) + T_1 & z \geq z_1 + tV_{pull} \end{cases} \tag{2.18}$$

The values m_1 through m_4, T_1 and z_1 are presented in Table 4.2.

Chapter 3

Numerical Methods

The Galerkin finite element method (GFEM) is employed to find an approximate solution to the temperature, flow, and concentration fields in the VGF-ACRT system. A short summary of essential concepts behind the GFEM is presented below based on the the detailed explanations from the following sources: [78–84]. For details on the application of the GFEM to crystal growth models, we direct the interested reader to the following sources: [40, 85–98].

3.1 Galerkin finite element discretization

3.1.1 Parametric mapping to the parent domain

The domain is first discretized into subdomains known as finite elements. These elements are nine-noded quadrilaterals, which allow for the discretization of complex domains. Next, parametric mapping is employed to transform the partial differential equations presented in Chapter 2 from the (r, z) coordinate system to a (ξ, η) coordinate system. In the (ξ, η) system, each quadrilateral element is mapped to a unit square, depicted in Figure 3.1. This technique simplifies the discretization of the governing equations and allows for a number of useful transformations. Mathematically speaking, the (r, z) coordinates of an arbitrary quadrilateral is mapped to the (ξ, η) coordinates of the parent element via the following relation:

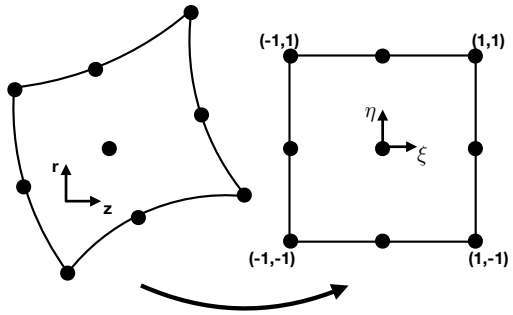

Figure 3.1: Parametric mapping to a unit square parent element.

$$(r, z) = \sum_{k=1}^{N} (r^k, z^k)\phi^k(\xi, \eta). \tag{3.1}$$

In the above equations, r^k and z^k are the nodal coordinates, and $\phi^k(\xi, \eta)$ are variable order Lagrange basis functions, described by [99]. The basis functions conveniently have the property that their value equals one at the node k and zero at all other nodes.

3.1.2 Finite element basis functions

The field variables $\mathbf{u}$, T, and C are approximated within the domain using the variable-order Lagrange basis functions $\phi^k(\xi, \eta)$:

$$\mathbf{u} \approx \hat{\mathbf{u}} = \sum_{k=1}^{N_u} \mathbf{u}^k \phi_u^k(\xi, \eta) \tag{3.2}$$

$$T \approx \hat{T} = \sum_{k=1}^{N_T} T^k \phi_T^k(\xi, \eta) \tag{3.3}$$

$$C \approx \hat{C} = \sum_{k=1}^{N_C} C^k \phi_C^k(\xi, \eta), \tag{3.4}$$

where $\hat{\mathbf{u}}$, $\hat{T}$, and $\hat{C}$ refer to the approximate solution to the field variables; and u^k, T^k, and C^k represent an unknown coefficient of the value of the field variable on the node k. N_u, N_p, and N_t are the number of basis functions per parent element for each field

variable. Biquadratic interpolation is chosen for for form of ϕ^k; however, the case is different for pressure. The preferred choice for pressure is a linear discontinuous basis function, ψ^k, as only certain velocity-pressure basis function combinations are allowed to retain LBB (Ladyzhenskaya, Babuska, and Brezzi) stability [100–103]. The pressure is then approximated via the following:

$$p \approx \hat{p} = \sum_{k=1}^{N_p} p^k \psi_p^k(\xi, \eta). \tag{3.5}$$

While the Lagrange basis functions ϕ^k are directly associated with nodes on each element, the ψ^k basis functions correspond to values of the pressure and the pressure gradient within the element center.

3.1.3 Weighted residuals

The approximate solutions defined in Equations 3.2-3.5 are then substituted into the governing differential equations 2.1-2.6 and the subscript i is dropped for convenience. All terms are gathered on one side of the equation to form the following residual equations:

$$\mathcal{R}_u = \rho \left(\frac{\partial \hat{\mathbf{u}}}{\partial t} + \hat{\mathbf{u}} \cdot \nabla \hat{\mathbf{u}} \right) - \nabla \cdot \hat{\mathbf{T}} - \rho \left[1 + \beta(\hat{T}_{mp} - \hat{T}) \right] \mathbf{g} \tag{3.6}$$

$$\mathcal{R}_p = \nabla \cdot \hat{\mathbf{u}} \tag{3.7}$$

$$\mathcal{R}_T = \rho c_p \left(\frac{\partial \hat{T}}{\partial t} + \hat{\mathbf{u}} \cdot \nabla \hat{T} \right) - k \nabla^2 \hat{T} \tag{3.8}$$

$$\mathcal{R}_C = \frac{\partial \hat{C}}{\partial t} + \hat{\mathbf{u}} \cdot \nabla \hat{C} - D \nabla^2 \hat{C} \tag{3.9}$$

where $\hat{\mathbf{T}} = -\hat{p}\mathbf{I} + \mu \left(\nabla \hat{\mathbf{u}} + (\nabla \hat{\mathbf{u}})^T \right)$. These residual equations, which represent the closure error in the approximation to the differential equations, should be small both globally and locally if the approximate solution is to be considered accurate. Galerkin's method requires that the residual equations are orthogonal to the set of basis functions over the domain, and a solution that satisfies this requirement is an acceptable approximation. This is accomplished by multiplying the residual equations by the appropriate

basis function and integrating over the computational domain:

$$\int_V \phi_u^i \mathcal{R}_u dV = 0 \tag{3.10}$$

$$\int_V \psi_p^i \mathcal{R}_p dV = 0 \tag{3.11}$$

$$\int_V \phi_T^i \mathcal{R}_T dV = 0 \tag{3.12}$$

$$\int_V \phi_C^i \mathcal{R}_C dV = 0, \tag{3.13}$$

where the superscript i represents the basis function associated with each node. These equations are now in the weak form, which are more suitable for analysis.

However, Equations 3.10-3.13 require further manipulation in order to eliminate the second derivatives of the dependent variables. The combination of the chain rule, written below for the temperature field,

$$\nabla \cdot \phi \nabla \hat{T} = \nabla \phi \cdot \nabla \hat{T} + \phi \nabla^2 \hat{T}, \tag{3.14}$$

and the Gauss-Ostrogradsky theorem (also known as the divergence theorem),

$$\int_V \nabla \cdot \phi \nabla \hat{T} dV = \int_A \phi \mathbf{n} \cdot \hat{T} dA, \tag{3.15}$$

can replace the second derivative term in Equation 3.8 with the following expression:

$$\int_V \phi \nabla^2 \hat{T} dV = -\int_V \nabla \phi \cdot \nabla \hat{T} + \int_A \phi \mathbf{n} \cdot \nabla \hat{T} dA, \tag{3.16}$$

where A represents the surface surrounding the volume. This is repeated for the velocity and concentration fields and substituted into Equations 3.6 and 3.9 to yield:

$$\int_V \phi_u^i \left[\rho \left(\frac{\partial \hat{\mathbf{u}}}{\partial t} + \hat{\mathbf{u}} \cdot \nabla \hat{\mathbf{u}} \right) - \rho \left[1 + \beta (T_{mp} - \hat{T}) \right] \mathbf{g} \right] dV + \int_V \nabla \phi_u^i \cdot \hat{\mathbf{T}} dV - \int_A \phi_u^i \mathbf{n} \cdot \hat{\mathbf{T}} dA = 0 \tag{3.17}$$

$$\int_V \psi_p^i \nabla \cdot \hat{\mathbf{u}} dV = 0 \tag{3.18}$$

$$\int_V \phi_T^i \left[\rho c_p \left(\frac{\partial \hat{T}}{\partial t} + \hat{\mathbf{u}} \cdot \nabla \hat{T} \right) \right] dV + \int_V \nabla \phi_T^i \cdot k \nabla \hat{T} dV - \int_A \phi_T^i \mathbf{n} \cdot k \nabla \hat{T} dA = 0 \tag{3.19}$$

$$\int_V \phi_C^i \left[\frac{\partial \hat{C}}{\partial t} + \hat{\mathbf{u}} \cdot \nabla \hat{C} \right] dV + \int_V \nabla \phi_C^i \cdot D_j \nabla \hat{C} dV - \int_A \phi_C^i \mathbf{n} \cdot D \nabla \hat{C} dA = 0. \tag{3.20}$$

Further substitution of the approximate solutions for $\hat{u}$, $\hat{T}$, and $\hat{C}$ into the above equations forms the set of algebraic differential equations below that can then be solved for the set of unknown coefficients at each node in the domain.

$$\int_V \phi_u^i \rho \sum_{k=1}^{N_u} \left(\phi_u^k \frac{\partial (\mathbf{u^k})}{\partial t} + (\mathbf{u^k})^2 \phi_u^k \cdot \nabla \phi_u^k \right) dV - \int_V \phi_u^i \rho \left[1 + \beta (T_{mp} - \sum_{k=1}^{N_T} T^k \phi_T^k) \right] \mathbf{g} dV + \int_V \nabla \phi_u^i \cdot \hat{\mathbf{T}} dV - \int_A \phi_u^i \mathbf{n} \cdot \hat{\mathbf{T}} dA = 0 \tag{3.21}$$

$$\int_V \psi_p^i \sum_{k=1}^{N_u} \mathbf{u^k} \nabla \cdot \phi_u^k dV = 0 \tag{3.22}$$

$$\int_V \phi_T^i \ \rho c_p \sum_{k=1}^{N_T} \left(\phi_T^k \frac{\partial T^k}{\partial t} + T^k \sum_{k=1}^{N_u} \mathbf{u^k} \phi_u^k \cdot \nabla \phi_T^k \right) dV + \int_V \ k \sum_{k=1}^{N_T} T^k \nabla \phi_T^i \cdot \nabla \phi_T^k dV - \int_A \phi_T^i \ k \sum_{k=1}^{N_T} T^k \mathbf{n} \cdot \nabla \phi_T^k dA = 0 \tag{3.23}$$

$$\int_V \phi_C^i \sum_{k=1}^{N_C} \left[\phi_C^k \frac{\partial C^k}{\partial t} + C^k \sum_{k=1}^{N_u} \mathbf{u^k} \phi_u^k \cdot \nabla \phi_C^k \right] dV + \int_V \ D_j \sum_{k=1}^{N_C} C^k \nabla \phi_C^i \cdot \nabla \phi_C^k dV - \int_A \phi_C^i \ D_j \sum_{k=1}^{N_C} C^k \mathbf{n} \cdot \nabla \phi_C^k dA = 0, \tag{3.24}$$

where

$$\hat{\mathbf{T}} = -\sum_{k=1}^{N_p} p^k \psi_p^k \mathbf{I} + \mu \sum_{k=1}^{N_u} \left(\nabla(\mathbf{u}^\mathbf{k} \phi_u^i) + (\nabla(\mathbf{u}^\mathbf{k} \phi_u^i))^T \right). \tag{3.25}$$

These equations are now in suitable form to solve fixed-grid problems. This form is favored since the spatial derivatives of the basis functions in the parent domain are known a priori. Transformation from the parent domain back to the real domain is accomplished using the Jacobian of transformation and Equations 3.2-3.5.

3.1.4 Arbitrary Lagrangian-Eulerian formulation

For problems on moving grids, of which ACRT is one, further manipulation of Equations 3.21-3.24 is required to address the temporal derivative. The time derivatives present in Equations 3.17-3.20 are taken with respect to the Eulerian (or global) reference frame, whereas the time derivatives of the basis function coefficients in Equations 3.21-3.24 are taken with respect to a fixed reference frame within the parent element. The nodal velocity in the parent frame, denoted by $\dot{\mathbf{x}}$, can be converted to the Eulerian frame via the following transformation:

$$\frac{\partial \hat{\mathbf{u}}}{\partial t} = \dot{\mathbf{u}} - \dot{\mathbf{x}} \cdot \nabla \hat{\mathbf{u}} \tag{3.26}$$

$$\frac{\partial \hat{T}}{\partial t} = \dot{T} - \dot{\mathbf{x}} \cdot \nabla \hat{T} \tag{3.27}$$

$$\frac{\partial \hat{C}}{\partial t} = \dot{C} - \dot{\mathbf{x}} \cdot \nabla \hat{C}, \tag{3.28}$$

$$\tag{3.29}$$

where $\dot{\mathbf{u}}$, $\dot{T}$ and $\dot{C}$ represent the time derivative with respect to the parent element reference frame. This is analogous to the material derivate of the Reynolds transport theorem. Physically speaking, this ensures that the temporal variation of a field variable is equal to the local variation in the parent domain minus a convection term that accounts for the relative motion of the nodes.

The arbitrary Lagrangian-Eulerian (ALE) formulation is employed with elliptic grid generation techniques to solve time-dependent moving boundary problems like the one

in the VGF-ACRT system. The nodal positions of the mesh are formulated as an additional differential equation that is solved simultaneously with the differential equations described in Chapter 2 and coupled via appropriate boundary conditions. These will not be discussed here for the sake of brevity; for further details on the techniques employed to solve moving boundary problems, please refer to [104].

3.2 Boundary conditions

The boundary conditions applied to the VGF-ACRT system are broadly categorized into three types: Dirichlet, Neumann, and Robin. Dirichlet boundary conditions are implemented by prescribing the value of the field variable at the boundary, thus replacing the residual equation. Neumann conditions, which prescribe the first derivative of the field variable at the boundary, and Robin conditions, which specify a linear combination of the field variable and its derivatives at the boundary, are implemented by replacing the integrand in the surface integral of Equations 3.23 and 3.24 with the specified value or expression. These conditions are often referred to as natural boundary conditions due to their natural appearance in the weak formulation of the residual equations. For the momentum residuals in Equation 3.21, the natural condition must specify a value or expression for the surface traction, $\mathbf{n} \cdot \mathbf{T}$.

3.3 Solution methods

The discretized residual equations can be represented by the vector $\mathbf{r}(\mathbf{z}, \dot{\mathbf{z}}, \mathbf{p}) = 0$, where $\mathbf{z}$ is the vector of unknown coefficients to the basis functions, $\dot{\mathbf{z}}$ is the vector of its time derivatives, and $\mathbf{p}$ is a vector of input parameters. The parametric mapping presented in Equations 3.2-3.5 allows for the separation of the temporal and spatial dependencies, where the coefficients $\mathbf{z}$ only depend on time while the basis functions only depend on space.

For stationary problems, $\dot{\mathbf{z}} = 0$ and the equation $\mathbf{r}(\mathbf{z}, \mathbf{p}) = 0$ can be solved via Newton-Raphson iteration:

$$\mathbf{z}^{k+1} = \mathbf{z}^k + f\Delta\mathbf{z}, \tag{3.30}$$

where $\mathbf{z}^{k+1}$, the solution at the $k+1$-th iteration, is approximated by $\Delta\mathbf{z}$, a solution update. A damping factor f can be included in the calculation. The solution update, $\Delta\mathbf{z}$, is calculated from the vector of residuals, $\mathbf{r}$, and the Jacobian, $\mathbf{J}$, which is evaluated at $\mathbf{z} = \mathbf{z}^k$:

$$\mathbf{J}\Delta\mathbf{z} = -\mathbf{r}. \tag{3.31}$$

Convergence is reached when the L2 norm of the residual vector and the solution update are both less than a specified tolerance, ϵ:

$$\|\mathbf{r}(\mathbf{z}^{k+1})\|_2 = \sqrt{\sum_{i=1}^{N} |r_i(z_i^{k+1})|^2} < \epsilon \tag{3.32}$$

$$\|\Delta\mathbf{z}\|_2 = \sqrt{\sum_{i=1}^{N} |\Delta z_i|^2} < \epsilon. \tag{3.33}$$

In the above equations, N is the total number of unknowns. For the calculations at hand, a tolerance of $\epsilon = 10^{-4}$ was used.

For time-dependent problems, the vector of temporal derivatives, $\dot{\mathbf{z}}$, must be appropriately discretized into smaller time domains. Time integration is implemented via a third-order explicit Adams-Bashforth predictor and a second-order implicit trapezoidal rule corrector. The residuals are reformulated as $\mathbf{r}(\mathbf{z}, \mathbf{z_0}, \dot{\mathbf{z_0}}, \mathbf{p}) = 0$, where the residual equations depend not only on the solution $\mathbf{z}$ at the current time, but also on the solution $\mathbf{z_0}$ and it's time derivative $\dot{\mathbf{z_0}}$ at the previous time step. Details of this method can be found in the following sources: [105–107].

3.4 Continuation methods

Newton-Raphson iteration converges quadratically when an initial guess is selected that is sufficiently close to the actual solution. However, for complex systems such as the VGF-ACRT system, selection of an appropriate initial guess is difficult if not impossible to do. First-order continuation techniques can be employed to assist the traversing of solution space from an initial guess to a final desired parameter value.

A converged solution at a parameter value P can be used as a high quality initial guess for the solution at a nearby value of $P + \Delta P$:

$$\mathbf{z}(P + \Delta P) \approx \tilde{\mathbf{z}}(P + \Delta P) = \mathbf{z}(P) + \mathbf{z_p}\Delta P, \tag{3.34}$$

where $\tilde{\mathbf{z}}$ represents the approximate solution at $P + \Delta P$, and $\mathbf{z_p}$ represents the first order change in $\mathbf{z}$. The value $\mathbf{z_p}$ is defined by:

$$\mathbf{J}\mathbf{z_p} = -\mathbf{r_p}, \tag{3.35}$$

where the Jacobian $\mathbf{J}$ is evaluated at parameter value P. The value $\mathbf{r_p}$ represents the derivative of $\mathbf{r}$ with respect to P, and is approximated by the following central differences equation:

$$\mathbf{r_p} \approx (\mathbf{r}(P + \epsilon) - \mathbf{r}(P - \epsilon))/2. \tag{3.36}$$

First order continuation methods are helpful not only for reaching desired parameter values, but also for the construction of solution curves and the calculation of parameter sensitivities. For more details on this and higher order continuation schemes, we direct the reader to the following sources: [82, 108, 109].

Chapter 4

Base Case Growth under Steady Conditions

The Bridgman growth of CZT has been well understood and characterized by many authors, e.g. [4, 32, 61]. However, changes to the geometry and furnace specifications yield subtle changes worthy of discussion, and the incorporation of tellurium introduces new physics that must be addressed. This chapter presents an overview of the underlying physics as demonstrated by the contour plots under steady (i.e. no rotation) conditions. The material and system properties for all calculations are shown at the end of this chapter in Tables 4.1 and 4.2.

4.1 Initial condition at zero growth

In a real system, once the system has been brought to a molten state, the furnace begins to translate. This adjusts the thermal fields such that material near the bottom tip of the ampoule will become supercooled. This will result in a spontaneous nucleation event that forms the initial crystalline domain. Nucleation is very complicated, and good continuum-level models do not exist for it to be included in the current model. Thus, we model the evolution of the system after a nucleation event has occurred. Specifically, we select an initial condition where approximately one third the boule has been solidified (just past the cone region) with steady-state thermal and flow fields calculated at translation rate of $V_{pull} = 0$.

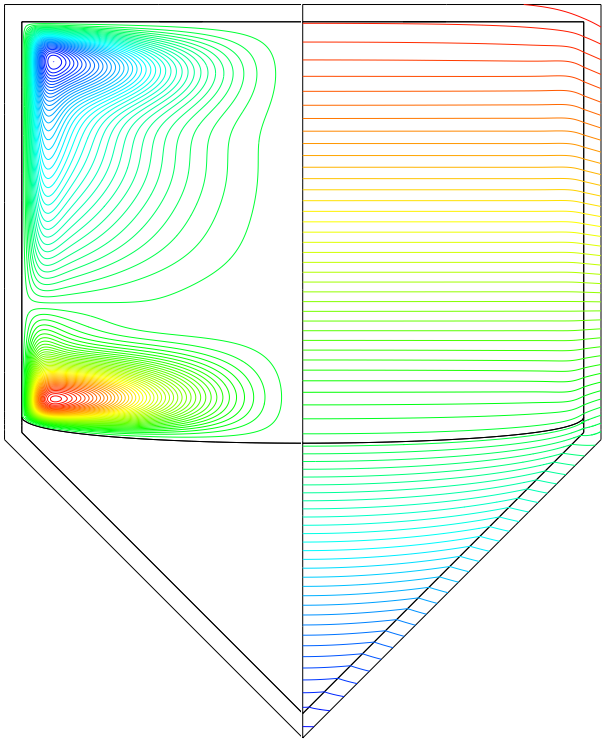

Figure 4.1: Streamlines (left) and temperature isotherms (right) and for a steady state, no-growth case. This serves as the initial flow field for the subsequent transient simulations. $\psi_{min} = -0.01030 cm^3/s$, $\psi_{max} = 0.011336 cm^3/s$, $T_{min} = 1298K$, $T_{max} = 1365K$

The steady state thermal field for zero growth is shown in the right of Figure 4.1. The temperature along the outer ampoule wall is determined by heat fluxes given by exchange with the effective furnace temperature profile. This creates a temperature gradient in the axial direction, with colder temperatures near the bottom of the ampoule and hotter temperatures near the top, as indicated by the blue and red contour lines, respectively. The isotherms are spaced closer together in the solid than in the liquid or the ampoule due to a lower thermal conductivity in the solid. This mismatch in thermal conductivities also creates a discontinuous slope of the isotherms at the ampoule wall, since $k_a > k_l > k_s$. At higher axial positions, the isotherms become farther spaced apart due to a shallower furnace gradient near the top of the ampoule.

The solid-liquid interface is concave, which is primarily a consequence of the mismatch in thermal conductivities between the materials. Close to the center, energy flows straight down toward the solid and out toward the ampoule. Near the ampoule wall, heat is directed both towards the wall in the $+r$ direction and in the $-z$ direction. This effect, due to the high thermal conductivity of the ampoule, creates the deflection of the interface particularly near the side wall. Latent heat is not a contributing factor at this point, since growth has not occurred, however, once the interface begins to move, latent heat will be released. This release of energy will melt back the interface slightly, resulting in an increase in the concavity.

Streamlines for the steady state initial condition are shown in the left of Figure 4.1. The scalar streamfunction, ψ, is defined for cylindrical coordinates as:

$$\frac{1}{r}\frac{\partial \psi}{\partial z} = -u_r \tag{4.1}$$

$$\frac{1}{r}\frac{\partial \psi}{\partial r} = u_z, \tag{4.2}$$

where u_r and u_z are the velocities in the r and z directions, respectively. The streamfunction represents a massless particle's path in the flow, and has units of ψ are $[=] m^3/s$. For streamlines plotted on the left half-plane, the sign indicates the direction of flow, with negative values corresponding to clockwise flow and positive values corresponding to counter-clockwise flow. While the streamfunction is technically only defined for steady state problems, it can nevertheless be calculated and used as an indicator of the

flow structure in transient problems.

The two-vortex flow structure in the left of Figure 4.1 is characteristic of the thermal buoyancy-driven natural convection found in classical Bridgman systems. In the upper half of the ampoule, liquid sitting near the ampoule wall is heated more than fluid at the center. This positive radial temperature gradient drives a clockwise vortex that brings fluid up the side wall and down the center. In the lower half of the ampoule, near the solid-liquid interface, fluid sitting towards the side wall is colder than fluid at the center. This drives a counter-clockwise vortex, where fluid rises at the center and falls near the side wall.

4.2 Transient calculations

With this steady state as an initial condition, a uniform distribution of tellurium is applied to the melt, and time integration can begin. The translating furnace profile adjusts the thermal field at every time step, thus changing the driving force for growth. The interface responds by translating, which results in the release of latent heat and segregated tellurium. The changes to the thermal field drive changes in the flow field, which then determine the distribution of the solute in the liquid. This, in turn, can influence the interface growth rate via thermodynamic effects.

While the thermal and flow fields remain relatively unchanged in structure, the concentration continues to adjust in response to the flux of material into liquid via segregation to conserve mass. A distribution of tellurium in the melt is shown in Figure 4.2 for a steady (i.e. non-ACRT) calculation shortly into growth. Regions of high concentration (indicated by the red color) close to the solid-liquid interface accumulate as the material is rejected from the growing solid. Tellurium is transported within the melt via the natural convection and diffusion. The lower counter-clockwise vortex sweeps fluid sitting close to the interface towards the center and then back towards the side wall at a higher axial position. While convective transport of tellurium is observed in the lower vortex, little mixing occurs between the upper and lower vortices. This is indicated by the very strong shear layer halfway up the melt, between which only diffusion of tellurium is allowed to occur.

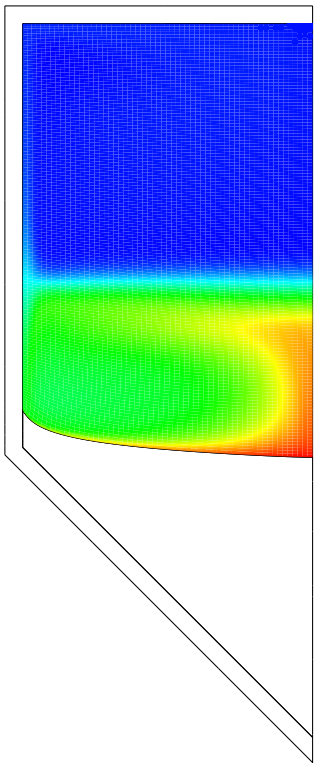

Figure 4.2: Concentration of tellurium in the melt (right) after a short period of applied growth at 2 mm/hr. Blue corresponds to $C_{min} = 53.50at\%$ and red corresponds to $C_{max} = 53.74at\%$.

With the thermal and solutal fields computed, the location and magnitude of constitutional supercooling, ΔT, can be calculated via comparison of the the composition-dependent melting point temperature, T_{mp}, to the local temperature, T_{local}:

$$\Delta T = T_{local} - T_{mp}(C). \tag{4.3}$$

This expression is similar to the classic constitutional supercooling criterion proposed by Tiller et al. [44], except here the liquidus temperature is determined by a fourth-order polynomial instead of a linear approximation. If ΔT is greater than zero, the local melt is superheated and stable. If the ΔT is less than zero, the local melt is supercooled and has the propensity to encourage a morphological instability. Isotherms for the magnitude of supercooling are plotted in Figure 4.3 for a later stage of growth than in Figure 4.2. Here, red contours correspond to areas where the melt is at its melting point temperature, where $\Delta T = 0$ K. Blue corresponds to areas where the melt is at its greatest magnitude of supercooling, where $\Delta T < 0$. The reversal of signs is due to the negative nature of ΔT. The blue contour lines near the center of Figure 4.3 indicate regions of severe supercooling, and the red contour lines toward the periphery are regions of minimal supercooling. This supercooled fluid is caused by an accumulation of tellurium, which not only adjusts the local concentration gradients but also alters the local interface shape and location, influencing the thermal field as well.

The effects of segregation and supercooling under steady conditions are further discussed in Chapter 6. There we will show the evolution of supercooled material over the course of a steady and ACRT simulation. The following chapter presents sample calculations of the system under ACRT, and highlight the relevant rotational fluid dynamic phenomena that occur.

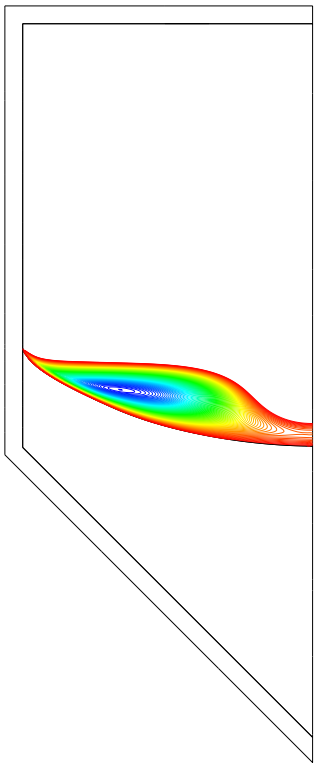

Figure 4.3: Supercooled regions of in the melt driven by accumulation of tellurium. Blue contours correspond to higher magnitudes of supercooled material. Blue corresponds to $\Delta T_{min} = -0.7685K$ and red corresponds to $\Delta T_{max} = 0K$.

Table 4.1: Material Properties

Symbol	Description	Value	Units
β	thermal expansion coefficient	7.69×10^{-5}	K^{-1}
$C_{p,l}$	heat capacity of liquid	0.187	J/(g K)
$C_{p,s}$	heat capacity of solid	0.159	J/(g K)
$C_{p,a}$	heat capacity of ampoule	1.192	J/(g K)
ϵ	emissivity of ampoule	0.3	—
γ_{ref}	surface tension at reference temperature	175	g/s^2
γ_T	temperature derivative of surface tension	-0.16	g/s^2 K
$D_{l,Zn}$	diffusion coefficient of zinc in liquid	1×10^{-4}	cm^2/s
$D_{s,Zn}$	diffusion coefficient of zinc in solid	1×10^{-9}	cm^2/s
$D_{l,Te}$	diffusion coefficient of tellurium in liquid	7.4×10^{-5}	cm^2/s
ΔH_f	enthalpy of fusion	209	J/g
k_l	thermal conductivity of liquid	0.02	W/cm K
k_s	thermal conductivity of solid	0.01	W/cm K
k_a	thermal conductivity of ampoule	0.025	W/cm K
ν	kinematic viscosity	8.0×10^{-3}	cm^2/s
ρ_l	liquid density	5.65	g/cm^3
ρ_s	solid density	5.65	g/cm^3
ρ_a	ampoule density	2.21	g/cm^3
T_{mp}	equilibrium melting temperature	1365	K

Table 4.2: System Properties and Nomenclature

Symbol	Description	Value	Units
A_1	Composition-dependent melting point formulation	-0.0003	$K/at\%^4$
A_2	Composition-dependent melting point formulation	0.0826	$K/at\%^3$
A_3	Composition-dependent melting point formulation	-7.6144	$K/at\%^2$
A_4	Composition-dependent melting point formulation	294.26	$K/at\%$
A_5	Composition-dependent melting point formulation	- 2584.2	K
ΔT	undercooling at interface	—	K
$\mathbf{g}$	gravitational acceleration vector	980	cm/s^2
$\mathbf{I}$	identity tensor	—	—
R	ampoule radius	3.25	cm
m_1	parameter in furnace profile	6.3122	K/cm
m_2	parameter in furnace profile	0.0390	K/cm^3
m_3	parameter in furnace profile	-1.4036	K/cm^2
m_4	parameter in furnace profile	15.1806	K/cm
$\mathbf{n}$	unit normal vector	—	—
$\mathbf{t}$	unit tangent vector	—	—
T_1	parameter in furnace profile	K1314	K
T_{int}	interface temperature	—	K
T_{ref}	reference temperature	1365	K
$\mathbf{u}$	velocity vector	—	cm/s
V_{pull}	applied pull rate	2	mm/hr
$\dot{\mathbf{x}}$	interface velocity vector	—	cm/s
z_1	parameter in furnace profile	3.25	cm

Chapter 5

Base Case Growth under the Accelerated Crucible Rotation Technique

The accelerated crucible rotation technique (ACRT) dramatically rearranges the thermal, flow, and solute fields from the results presented in the previous chapter. In this chapter, contour plots are presented under a typical rotation schedule to elucidate and explain the important rotational fluid dynamic phenomena. In theory, the subsequent enhanced convection will mix the melt and adjust the local thermal and concentration gradients sufficiently enough to prevent an instability at the solid-liquid interface during growth.

A sample rotation schedule is depicted in Figure 5.1. Four notable regimes are identified: 1) Acceleration from rest to a maximum rotation rate, 2) constant rotation at the maximum rotation rate, 3) deceleration from the maximum rotation to rest, and 4) a stationary regime where the crucible is held at rest. This sequence is then repeated in the reverse direction, completing a full cycle. An ACRT schedule will be specified by the following five parameters: Ω_0, τ_a, τ_r, τ_d, and τ_s, which refer to the maximum rotation rate (RPM), the time alloted for acceleration (s), the time allotted for the constant regime (s), the time allotted for the deceleration regime (s), and the time allotted for the stationary or stopped regime (s), respectively.

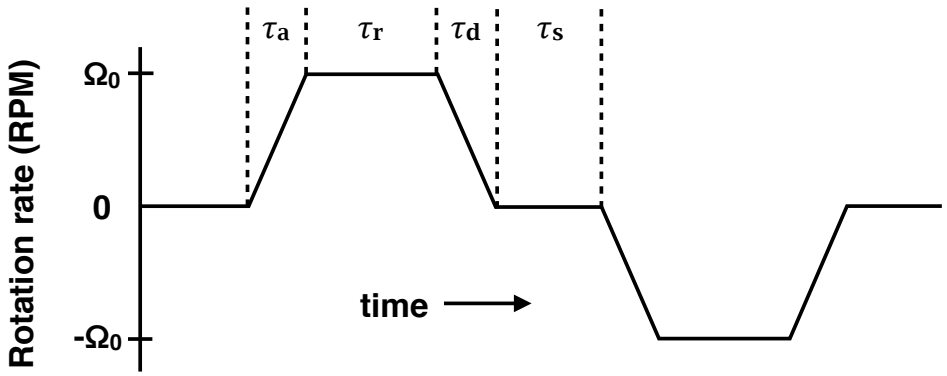

Figure 5.1: A schematic of a rotation schedule with five design parameters: Ω_0, the maximum rotation rate; τ_a, the length of time over which to accelerate from zero to the maximum rotation rate; τ_r, the length of time over which to hold at the maximum rotation rate; τ_d, the length of time over which to decelerate from the maximum rotation rate to zero; and τ_s, the length of time over which to hold the system stationary.

5.1 Azimuthal velocity

As rotation is imparted upon the system, momentum is diffused inwards from the sidewalls towards the center. It is instructive to observe this effect via contours of the u_θ velocity contours for multiple points during the first application of a typical rotation schedule, shown in Figure 5.2. The following rotation schedule is applied to the system: $\Omega_0 = 30$ RPM, $\tau_a = \tau_d = \tau_s = 60$ seconds and $\tau_r = 15$ seconds. The blue contours correspond to azimuthal velocity in the counter-clockwise direction, and the red contours correspond to the clockwise direction. Rotation is applied after several hours of steady growth, as indicated by an interface position that is higher than the initial condition presented in Chapter 4. The interface has also deflected subsequently; this is a consequence of accumulated tellurium and is discussed at length in Chapter 9.

The initial effects of rotation during acceleration are apparent by the few velocity contours present near the sidewall, indicating fluid is moving in the clockwise direction

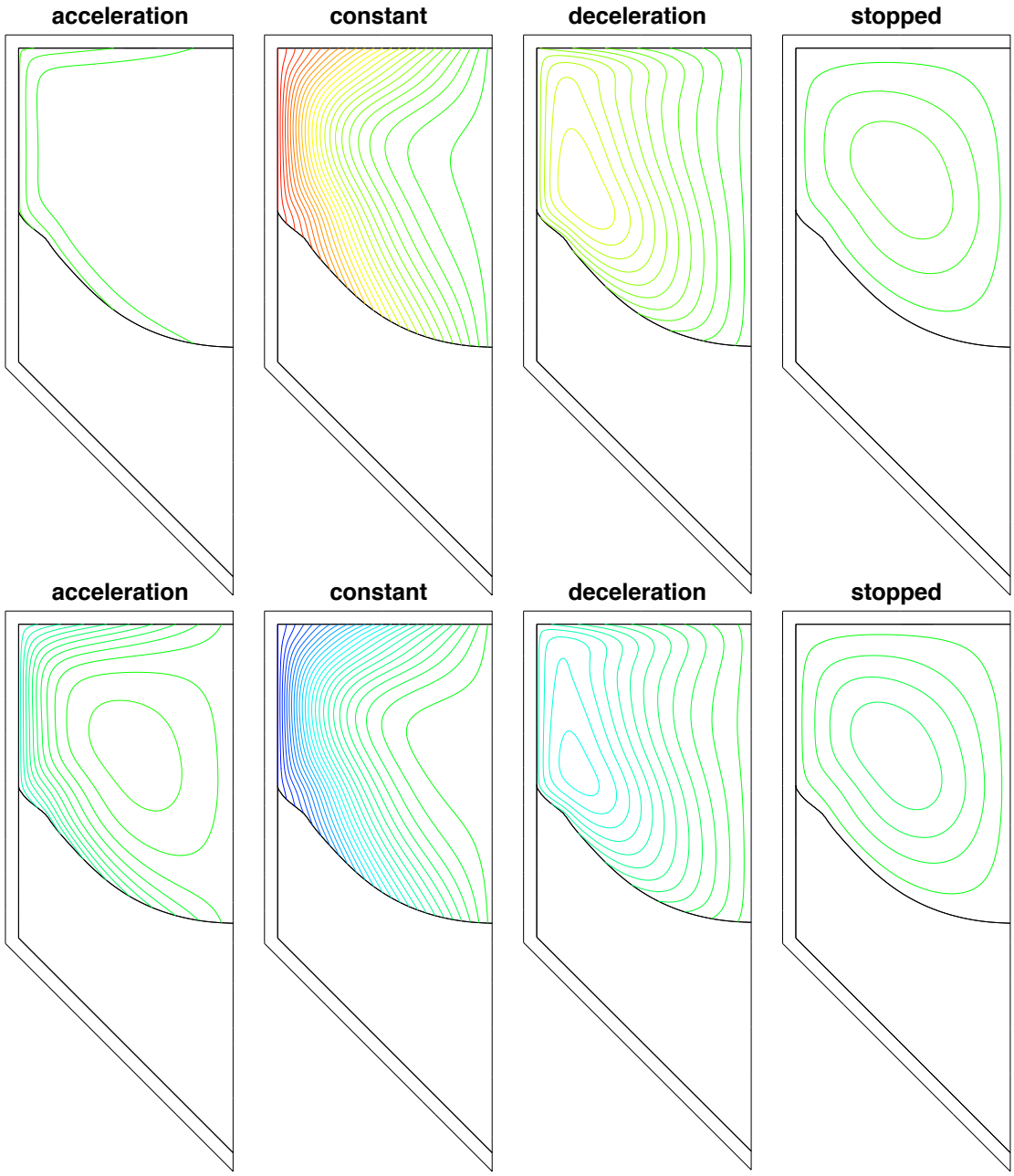

Figure 5.2: Azimuthal velocity contour plots for a sample rotation schedule. Blue corresponds to $u_{\theta min} = -10.21 cm/s$ (-30 RPM), and red corresponds to $u_{\theta max} = 10.21 cm/s$ (30 RPM).

. As rotation continues at a constant rate, momentum has diffused inwards and material towards the center also begins to rotate. Solid body rotation is almost entirely achieved, at which point deceleration occurs. Fluid at the side wall begins to slow down, as indicated by the dark green contours close to the side wall. At this point, fluid near the center is moving faster than fluid near the sidewall, which is an important arrangement required to induce Taylor-Görtler instabilities (discussed in section 5.2). Upon stopping, the fluid still has residual angular momentum that slowly dissipates from the sidewall towards the center. Acceleration then begins in the counter-clockwise direction, as indicated by the change from red to blue contours. Again, fluid sitting near the solid surfaces begins to spin, and this angular momentum is slowly propagated inwards towards the fluid that is still moving in the reverse direction. By the time a constant rotation rate is reached, the entirety of the melt is moving in the same direction, and solid-body rotation is approached. Upon deceleration, fluid moving towards the side wall moves slower than the bulk, as indicated by the green contours. When the system is then held again at rest, the angular momentum slowly dissipates. This constitutes an entire cycle, and is repeated during the entirety of the growth process. At solid body rotation, the flow is characterized by the rotational Reynolds number:

$$Re_{rot} = \frac{R^2 \Omega_0}{\nu}, \tag{5.1}$$

where R, Ω_0, and ν represent the radius, the maximum rotation rate, and the kinematic viscosity, respectively.

5.2 Relevant rotational fluid dynamic phenomena

Coupling of the azimuthal and meridional flows in the Navier-Stokes equations results in unique patterns that only arise in rotating fluids. Inspection of the streamlines representing meridional flows at the same time points as in Figure 5.2 reveal two phenomena that are uniquely observed under ACRT conditions.

As acceleration begins, fluid near the upper and lower surfaces are forced outwards towards the sidewall as a consequence of Ekman transport, thus overriding the underlying buoyancy-driven structure described in Chapter 4. With its origins in oceanic sciences, Ekman transport is the spiral-like motion of fluid that occurs near a horizontal

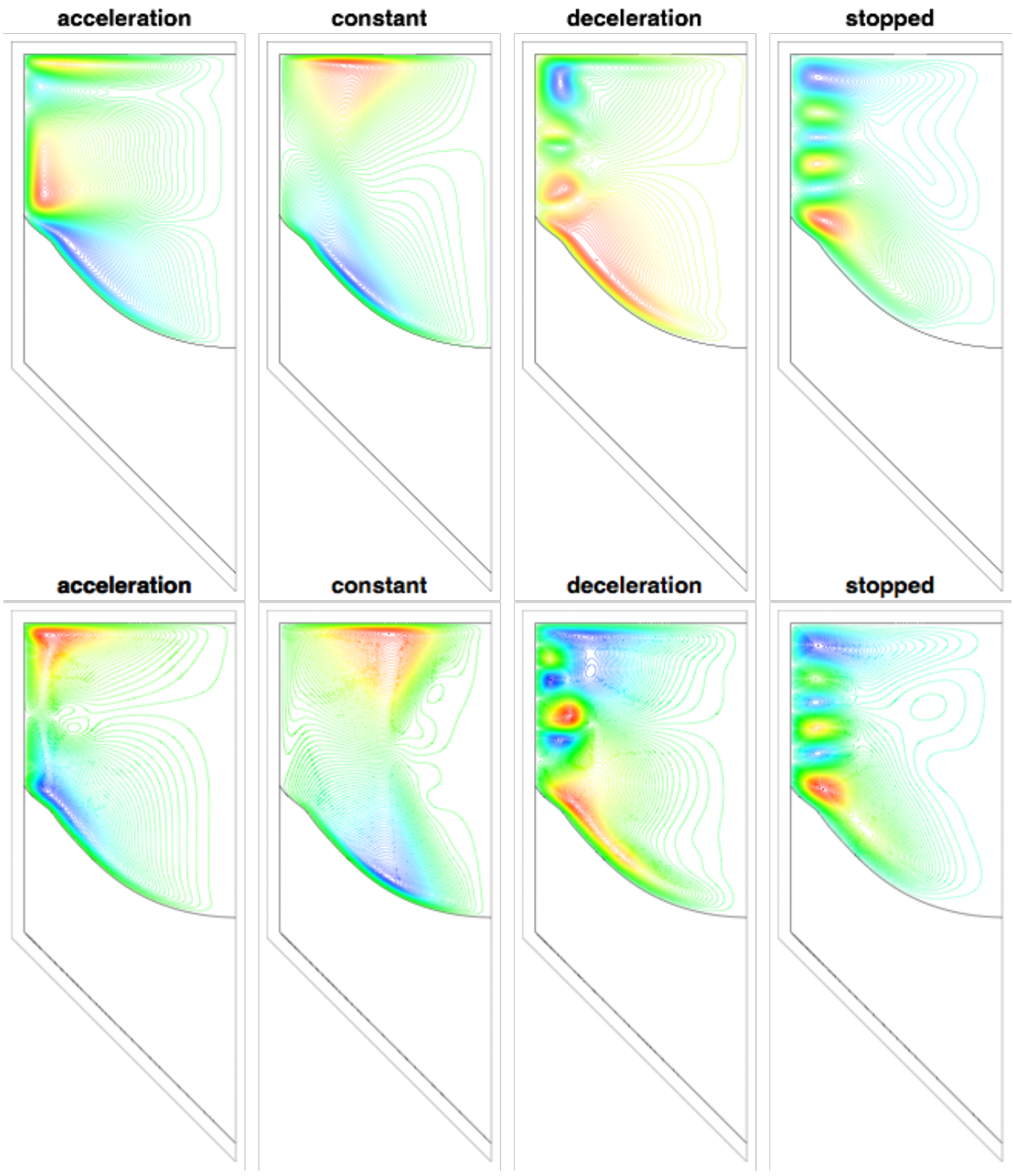

Figure 5.3: Streamlines for a sample rotation schedule. $\psi_{min} = -0.01593 cm^3/s$ and $\psi_{max} = 0.019427 cm^3/s$.

boundary subjected to a Coriolis force [52,110–119]. During acceleration, the upper and lower solid-liquid surfaces impart a force to the proximal fluid in the azimuthal direction that pushes the fluid outward in a spiral pattern from the center towards the side wall. This is observed by the upper-most counter-clockwise vortex and lower-most clockwise vortex that forms during the acceleration regime in Figure 5.3. The momentum boundary layer associated with this Ekman transport is defined by the characteristic thickness,

$$\delta_{Ek} = \sqrt{\frac{\nu}{\Omega_0}}. \tag{5.2}$$

This characteristic thickness can be observed qualitatively in Figure 5.3 during acceleration and deceleration in the small regions near the solid-liquid interfaces over which a large change in velocities occur. The timescale of the Ekman transport is characterized by:

$$\tau_{Ek} = \sqrt{\frac{R^2}{\Omega\nu}}, \tag{5.3}$$

which is a measure of the time required to reach solid body rotation upon a step change in Ω_0. Conventional wisdom recommends that $\tau_r = \tau_{Ek}$ so the system can fully reach solid-body rotation. For the case of $\Omega_0 = 30$ RPM, $\tau_{Ek} = 20$ seconds, which is slightly greater than τ_r. Nevertheless, solid body rotation is almost achieved after the constant period, and the Ekman flow has developed and dominated the natural convection that was still present during the acceleration period.

Upon deceleration, the Ekman flow is reversed, with an upper-most clockwise vortex and the lower-most counter-clockwise vortex pumping fluid towards the center. A second, more dramatic instability occurs at this point: Taylor-Görtler instabilities, which are stacked, counter-rotating vortices that line the side wall as a consequence of the rearrangement of flows. Derived from the same principles as Taylor-Couette instabilities, which are found in coaxial rotating cylinders [120–123] these instabilities occur when there is a reversal of the angular momentum gradient. Taylor-Görtler instabilities only occur above a sufficiently high rotational Reynolds number [124]. This instability can aid the radial mixing of the fluid, and has historically been postulated [55] to prevent the nucleation of new grains along the sidewalls [55].

5.3 Conclusion

We have presented preliminary results that demonstrate the changes in the flow patterns under ACRT. These will be observed in many of the simulations presented in future chapters. However, far more complicated and interesting are the secondary impacts on the composition and supercooling fields, which will be discussed in the following chapter. With an understanding of how supercooling is altered under ACRT, a thermodynamically consistent metric will be proposed for the assessment of rotation schedules. This metric will be utilized in Chapter 7 to assess some of the conventional wisdom proposed by Capper [51]. In Chapter 8, this metric is expanded upon, and applied to a factorial design of experiments with the purpose of better understanding each component of a rotation schedule. Chapter 9 will then shift way from schedule optimization toward system design optimization with the comparison of two differing furnace profiles. Lastly, model validation efforts are presented in Chapter 10 to ensure that the previous chapters are accurately representing the realistic phenomena.

Chapter 6

The Rearrangement of Constitutionally Supercooled Fluid under Accelerated Crucible Rotation

6.1 Summary

Via consideration of tellurium segregation and transport, we show that steady growth from a tellurium-rich melt produces persistent supercooling in front of the growth interface, likely leading to morphological instability. The application of ACRT rearranges melt flows and tellurium transport but, in contrast to conventional wisdom, does not altogether eliminate supercooling of the melt. Rather, a much more complicated picture arises, where spatio-temporal realignment of supercooled melt may act to locally suppress an instability. A better understanding of these mechanisms and quantification of their overall effects will allow for future growth optimization. Note that many of these results were first published in [125] and reproduced with permission from Elsevier.

6.2 Introduction

To model the effects of ACRT, a time-dependent, azimuthal velocity is imposed on the crucible walls and solid-liquid interface. The rotation schedule used in the calculations is shown in Figure 6.1a. The schedule is designed using characteristic measures of time evolution and strength for ACRT flows. The first of rotation schedule considerations is addressed by the Ekman time scale, $\tau_{Ek} = \left(R^2/(\nu\Omega_0)\right)^{1/2}$, where R, ν, and Ω_0 are the radius, kinematic viscosity, and maximum rotation rate, respectively. This value characterizes the period of time needed to approach a solid-body rotational flow state. The second consideration is embodied by the rotational Reynolds number, $\mathrm{Re}_{rot} = \Omega_0 R^2/\nu$, which measures the relative amount of inertia imparted to the flow by rotation. For the Washington State University (WSU) growth system and the schedule defined in Figure 6.1a, $\tau_{Ek} \approx 36$ seconds, thus the constant period should be of equal or greater value than the Ekman timescale. $\tau_r = 120$ seconds, which allows enough time for the melt to reach solid-body rotation. The maximum applied rotation gives a value of $\mathrm{Re}_{rot} \approx 1400$, which is sufficient to impart enough angular momentum to the fluid to trigger the nonlinear Taylor-Görtler instability [58,61]. The remaining schedule parameters are chosen based on previous experiments: $\tau_a = 60$ seconds, $\tau_d = 30$ seconds, and $\tau_s = 0$ seconds.

A translation velocity of 2 mm/h is applied to both systems with a furnace profile described in Chapter 2.2. The melt composition is tellurium-rich, as is typically employed for melt growth of CZT for radiation detector applications. For the following calculations, we specify an initial melt with a uniform tellurium mole fraction of C = 0.535. The initial thermal and flow states for the simulations are shown in Figure 6.1b, and discussed at length in Chapter 4.

6.3 Results

6.3.1 Growth without crucible rotation

We first present the case of growth in this system without application of ACRT. Figure 6.2 shows contours of the tellurium cocentration on the left and the supercooling in the melt on the right at successively increasing times. As growth proceeds, the solid-liquid

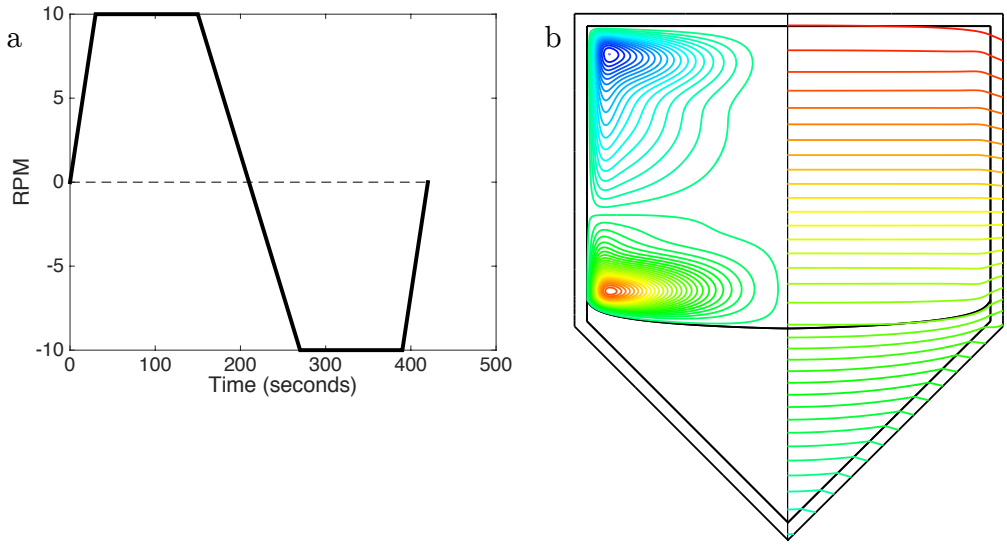

Figure 6.1: (a) The rotation schedule used in the simulation, with $\Omega_0 = 10$ RPM, $\tau_a = 60$ sec, $\tau_r = 120$ sec, $\tau_d = 30$ sec, and $\tau_s = 0$; (b) steady state streamlines (left) and temperature isotherms (right) used as an initial condition for transient simulations. $\psi_{min} = -0.01030 cm^3/s$, $\psi_{max} = 0.011336 cm^3/s$, $T_{min} = 1298K$, $T_{max} = 1365K$

interface moves upward and becomes slightly more concave in shape. The tellurium concentration field evolves from an initially homogeneous state to that seen in Figure 6.2a. Due to the rejection from segregation during growth, an enriched layer of tellurium has built up in the melt in front of the solid-liquid interface. The underlying flow, which retains the two-cell character shown in Chapter 4, sweeps tellurium inward along the solidification interface and upward at the centerline. The upper portion of the melt is isolated from the lower by the shear layer between the two circulation cells, so tellurium from the lower cell can only slowly diffuse across them. Thus, the upper region's concentration is much less than the region near the growth interface. As time proceeds, the total amount of tellurium in the melt increases, as indicated by the changing colors.

Even though the absolute changes in composition are rather small, the consequences of the build-up of tellurium in the melt are indicated by the regions of supercooled liquid in front of the growth interface shown the right side of the images of Figure 6.2. Specifically, we plot contours of $\Delta T \equiv T_{local} - T_{mp}(C)$, where T_{local} is the local melt temperature and $T_{mp}(C)$ is the constitutionally-dependent melting temperature calculated from the phase diagram. The existence of these regions indicates the possible onset of morphological instability during crystal growth via the mechanism of constitutional supercooling, as originally put forth by Tiller et al. [44]. As shown by the increased areas enclosed by the red contours in Figure 6.2, the melt adjacent to the growth interface becomes progressively more unstable as time proceeds.

The influence of tellurium also influences the interface velocity. The interface velocity is plotted for growth under steady conditions in Figure 6.3. The velocity begins near zero as the initial condition is chosen to be a no-growth steady state. As the furnace profile is translated in time, the interface responds by growing. As the interface velocity increases, segregation of tellurium occurs proportional to the velocity. This reduces the solidification temperature corresponding to the phase diagram, which retards the interface growth significantly. This effect is compounded as tellurium continues to accumulate in the melt, and is reflected in the plateau of the interface velocity. The average interface velocity over the course of 22 hours is 0.55 mm/hr, which is significantly suppressed below the applied translation rate of 2 mm/hr.

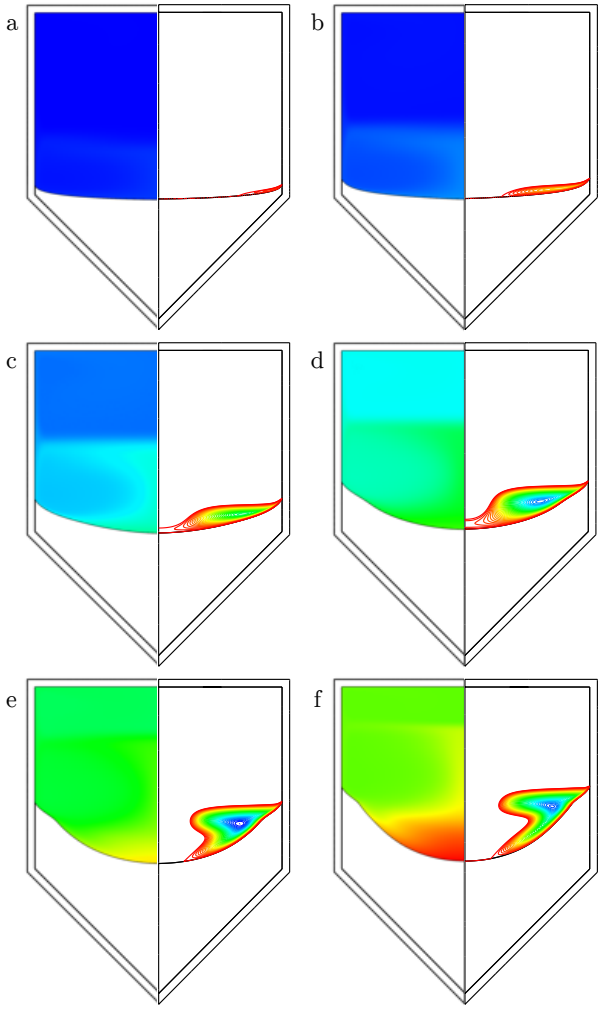

Figure 6.2: Results for steady growth at various time steps. Concentration plots (left) are shown for varying tellurium concentrations and supercooling (right) is shown indicating the location and magnitude of supercooled fluid. Red and blue correspond to higher and lower values, respectively. Growth begins with an initial condition of homogeneous tellurium concentration in the melt, and integrated in time (hours): (a) 2.457, (b) 3.084, (c) 3.712, (d) 4.339, (e) 4.966, and (f) 5.593. $C_{min} = 53.48 at\%Te$, $C_{max} = 55.29 at\%Te$, $\Delta T_{min} = -1.27K$, and $\Delta T_{max} = 0K$.

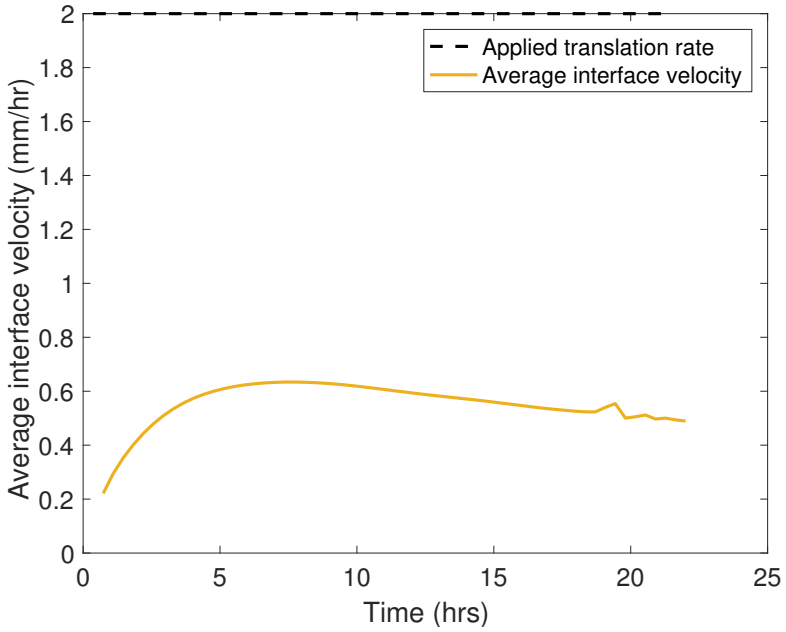

Figure 6.3: Average interface velocity (orange) compared to the applied furnace translation rate (dashed) for the steady growth case.

6.3.2 Growth with ACRT

The next set of simulations consider the same growth conditions but with the repeated application of the ACRT rotation schedule depicted in Figure 6.1. Plots of the streamlines (left) and temperature isotherms (right) are shown for ACRT growth in Figure 6.4. The system is shown at the start of the 9th cycle into growth, and each case corresponds to a different regime of rotation during one ACRT cycle: (a) acceleration, (b) constant rotation, (c) deceleration, (d) acceleration in the reverse direction.

Two notable fluid dynamical phenomena are seen during spin up and spin down of the crucible. The characteristic Ekman flow [49], appearing during acceleration and deceleration, is observed in Figures 6.4a and c and is responsible for forcing fluid outwards and inwards along the upper and lower interfaces. Taylor-Görtler vortices [46], stacked vertically along the crucible wall and appearing during deceleration, are observed in Figure 6.4d at the end of spin down. These vortices are responsible for radially mixing the melt. These flow structures are critical to achieving mixing in ACRT and are discussed more extensively in Refs. [57,61]. The isotherms, drawn in the right-side images of these plots, clearly show that the solid-liquid interface does not lie on a single isotherm. With variation of the melt composition caused by segregation and convection, the interface follows instead the solidification temperatures given by the phase diagram.

Figure 6.5 shows contours of the tellurium concentration field in the melt on the left and the melt supercooling on the right at the same times as in the previous figure. Interestingly, the tellurium in the melt is not completely homogenized, even though eight complete ACRT cycles have been applied. This is in contrast to previous work by Yeckel and Derby [58], who only considered the segregation of zinc during growth.

The right images of Figure 6.5 show a very complicated spatio-temporal evolution of melt supercooling through the ACRT cycle and demonstrate that, at least for this particular rotation schedule, ACRT does not completely eliminate supercooling. Rather, the regions of supercooled melt sweep across the interface while simultaneously growing or shrinking during different portions of the ACRT cycle. We speculate that the periodic abatement of supercooling may enable local re-stabilization of the interface. In contrast to the case of steady growth, where the persistent presence of supercooling likely forms and propagates a cellular morphology over time, the growth of cells may be inhibited by the short periods of instability over an ACRT cycle or, in effect, healed by periods

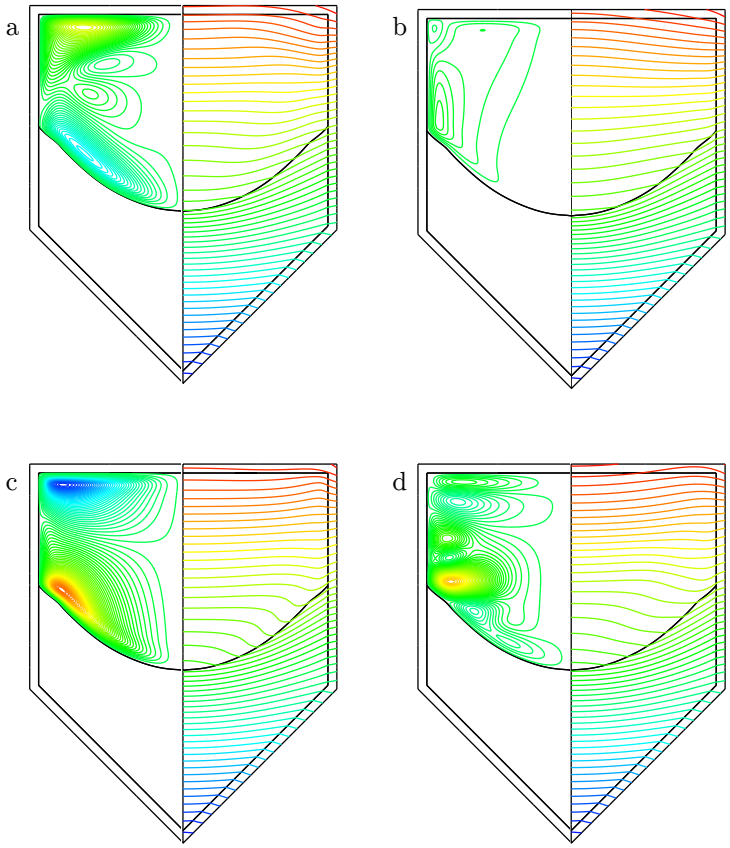

Figure 6.4: Results for ACRT growth at various time steps during the 9th cycle. Streamlines (left) and temperature contours (right) are shown. $\psi_{min} = -0.0897 cm^3/s$, $\psi_{max} = 0.121 cm^3/s$, $\Delta\psi = 0.00421 cm^3/s$, $T_{min} = 1273K$, $T_{max} = 1325K$, $\Delta T = 1.04K$. Figures correspond to the following distinct regimes in the ACRT cycle: a) acceleration, b) constant rotation, c) deceleration, d) acceleration in the reverse direction.

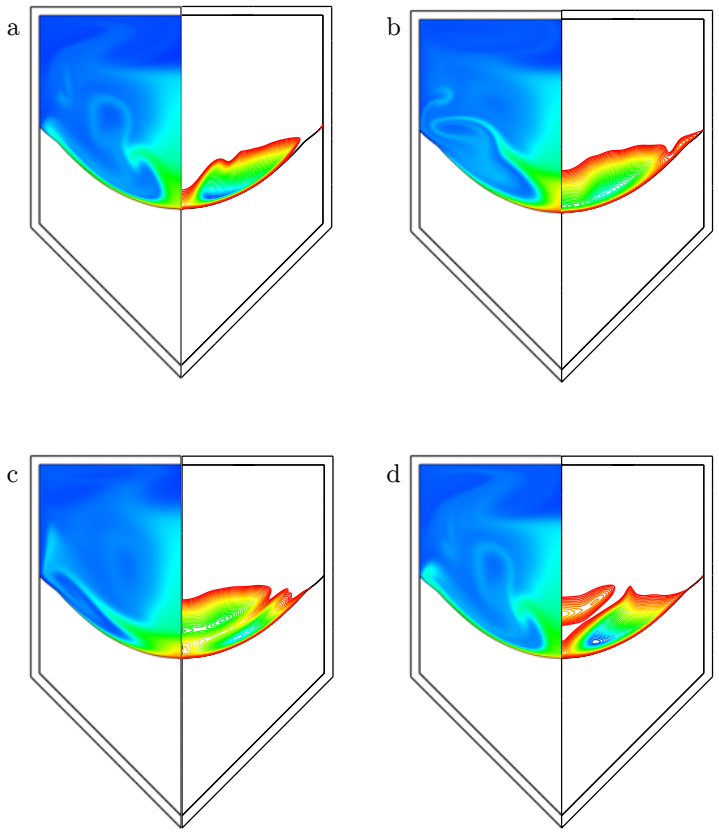

Figure 6.5: Results for ACRT growth at various time steps. Concentration plots (left) are shown for tellurium concentration and supercooling (right) is shown indicating the location and magnitude of supercooled fluid. Red and blue corresponding to higher and lower values, respectively. $C_{min} = 54.77at\%$, $C_{max} = 55.35at\%$, $\Delta T_{min} = -4.39K$, and $\Delta T_{max} = 0$. Figures correspond to identical time steps as in Figure 6.4.

when the supercooling is momentarily swept away.

The rearranged flows under ACRT also disrupt the interface velocity. A plot of the average interface velocity versus time for the ACRT case is shown in Figure 6.6 in contrast to the steady case. The ACRT case has an average interface velocity of 0.95 mm/hr, indicating it is effective in increasing the growth rate over the steady case, a fact that is corroborated by previous authors [47, 58]. However, the interface velocity spikes and falls in phase with the rotation schedule, particularly near the beginning of rotation. After 3 full cycles, a stable periodic cycle of interface velocities is reached.

A closer look at the interface velocity at the beginning of the 9th cycle is shown in Figure 6.7, where each period of rotation is identified. A cursory explanation for these oscillations is presented: during acceleration, Ekman flow sweeps newly segregated and highly concentrated fluid across the interface towards the side wall. This is shown in the concentration field of Figure 6.5a. This increase in composition locally reduces the solidification temperature, reducing the driving force for growth. This reduction in interface velocity is apparent with a minimum of 0.67 mm/hr during this period. A reduction of the interface velocity decreases the driving force for segregation corresponding to Equation 2.16, which reduces the local composition. This momentarily decreases the supercooling along the interface, which is consistent with the supercooling contours in Figure 6.5a that do not cover the entirety of the interface. This effect is continued in the next period, where the system is allowed to rotate at constant rotation. As solid body rotation is reached, the resulting lower composition increases the solidification temperature, subsequently increasing the driving force for growth. Here a spike in the interface velocity of 1.18 mm/hr is observed, and the subsequent segregation and supercooling is observed in Figure 6.5b. Upon deceleration, Ekman flow sweeps less concentrated fluid back towards the center across the interface, depicted in Figure 6.5c. This local reduction of composition then increases the driving force for growth, as observed by the spike in interface velocity of 1.15 mm/hr. As the interface velocity spikes, it increases the driving force for segregation. This flux of highly concentrated fluid then exacerbates the supercooling. An entirely new region of supercooled fluid has been created during this period, and overtaken the supercooling created in the previous period, as shown in the contours of Figure 6.5c. This is repeated in the reverse direction. While in reality the solute transport and the interface velocities are simultaneously influencing each

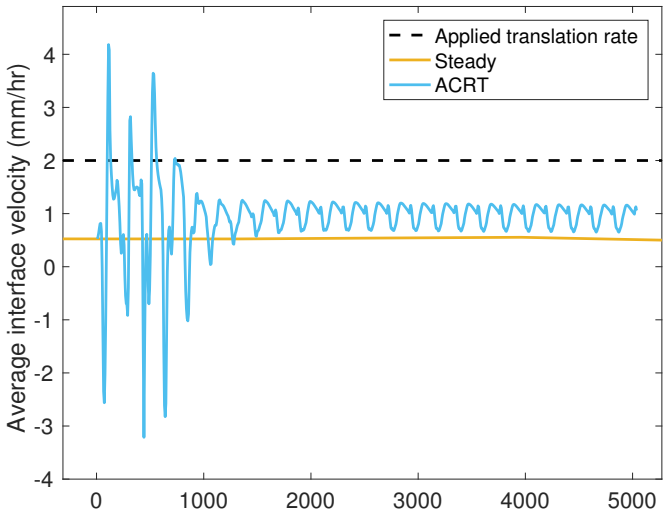

Figure 6.6: Average interface velocity for the steady versus ACRT cases. The steady case has an average interface velocity of 0.55 mm/hr, while the ACRT case has an average interface velocity of 0.95 mm/hr. Both are well below the applied translation rate of 2 mm/hr due to compositional effects on solidification.

other along with the effects of the thermal field, it is apparent that large changes in the interface velocity lead to periodic changes to the local supercooling field.

6.4 Development of thermodynamically consistent metric for schedule assessment

To the best of our knowledge, this is the first computation to show that segregation of tellurium drives constitutional supercooling. Our results also reveal that ACRT does not altogether eliminate supercooling but rather periodically adjusts it. To quantitatively capture this behavior, a thermodynamically consistent metric is proposed here and expanded upon further in Chapter 8 that quantitatively reflects the changing stabilizing and destabilizing conditions along the interface.

The metric definition begins with an improvement over the classic stability criterion put forth by Tiller et al. described by Equation 1.1: the Mullins and Sekerka stability criterion [126]. Unlike Tiller's, this criterion takes into account both thermal gradients

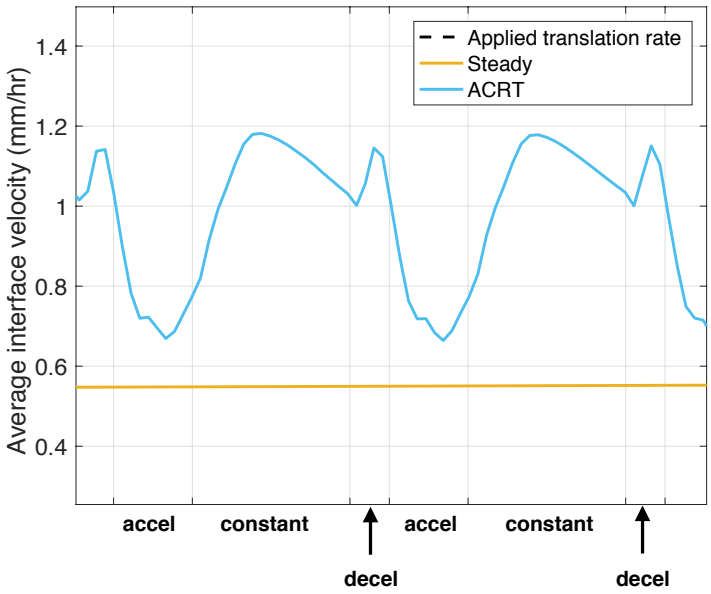

Figure 6.7: Average interface velocity for the 9th ACRT cycle. The interface velocity oscillates in phase with the rotation schedule.

in the liquid and the solid weighted by the thermal conductivities. A stability value, s, is calculated via the following equations:

$$s = -\frac{1}{2}\left(\mathscr{G}' + \mathscr{G}\right) + mG_c \tag{6.1}$$

$$\mathscr{G}' = \frac{k_s}{\bar{\kappa}} G_s \tag{6.2}$$

$$\mathscr{G} = \frac{k_l}{\bar{\kappa}} G_l \tag{6.3}$$

$$\bar{\kappa} = \frac{1}{2}\left(k_s + k_l\right). \tag{6.4}$$

In the above equations, k_s and k_l are the thermal conductivities of the solid and the liquid, respectively, and G_s and G_l are the local thermal gradients normal to the interface in the solid and liquid, respectively. G_c is the local liquid concentration gradient normal

to the interface, and m is the local slope of the liquidus line. Equation 6.1 is derived from a linear stability analysis of a one dimensional, no-growth, steady state growth system. While these assumptions are not valid in the current system, we believe the principles can be extended to our system since we are calculating the highly localized variations in concentration and temperature. The quantity s can be calculated at every node along the two-dimensional solid-liquid interface as a function of the local thermal and compositional values. If s is greater than zero, that point along the interface will be unstable, and we would predict a cellular morphology to form. If s is less than zero, that point along the interface will be stable and remain planar. In short, this value predicts whether a perturbation in the interface will be stabilized by the local thermal and compositional fields, allowing the interface to return to its planar configuration, or whether it will be destabilized by the local conditions, allowing the perturbation to grow into the cellular morphology described above. For an in-depth derivation and further discussion of this criterion, we direct the interested reader to the following references: [126–133].

At every time point t within a transient calculation the percent of stabilized interface area can be calculated. This is done by aggregating the cylindrical area along the interface that is stable, and dividing it by the total area for a final value referred to as A_t. This value is plotted as a function of time to assess the changing stability of the interface during rotation. A representative result for a different ACRT cycle is shown in Figure 6.8, where A_t is superimposed with the interface velocity for the same rotation schedule. During periods of acceleration where the interface velocity decreases, the interface stability spikes to a maximum of 36% stable. During periods of deceleration where the interface velocity spikes, the A_t drops to a minimum of 5.3% stable. This behavior is consistent with the discussion in Section 9.4, where changes to the interface velocity cause oscillations in the supercooled fluid and thus stability of the interface. Although this metric does not capture any kinetic effects of an instability growing or diminishing, it is a preliminary quantitative measure that can be used to compare rotation schedules. We will use this metric in the next chapter to quantitatively compare two rotation schedules.

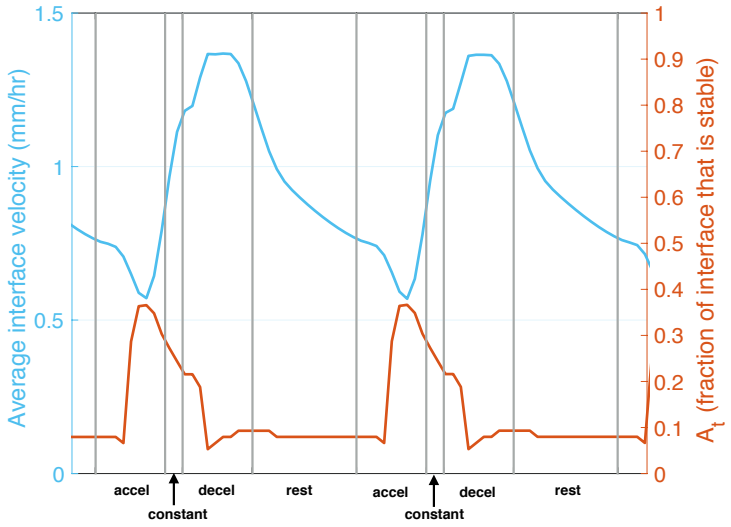

Figure 6.8: Superposition of the average interface velocity with A_t, the fraction of stabilized interface during the 9th cycle for the following rotation schedule: $\Omega_0 = 10$ RPM, $\tau_a = 60$ sec, $\tau_r = 15$ sec, $\tau_d = 60$ sec, and $\tau_d = 90$ sec.

6.5 Conclusions

Our simulations demonstrate that steady growth, without rotation, from an initially tellurium-rich melt results in segregation that is sufficient to drive supercooling. That such conditions exist is consistent with the notion that liquid-phase inclusions may be captured via morphological instabilities of the growth interface.

The application of ACRT to this system shows that, despite the formation of Ekman and Taylor-Görtler flows, complete mixing is not attained in the melt. Conventional wisdom presumes that near-complete mixing driven by ACRT eliminates all supercooling in the melt; however, we observe that supercooled regions of melt shift through time and space in response to ACRT-driven flows. This points to the effectiveness of the Ekman flows in temporarily ameliorating supercooling, and that classical ideas of complete homogenization of the melt may not be necessary. This point will be directly addressed in the next chapter, where the conventional wisdom will be critically assessed through comparison of two rotation schedules.

Chapter 7

Assessment of Conventional Wisdom Through Comparison of Two Rotation Schedules

7.1 Summary

We assess the impact of two ACRT schedules designed for a cadmium zinc telluride growth system per the classical recommendations of Capper and co-workers. The "flow maximizing" ACRT schedule, with higher rotation rates, effectively mixes the solutal field in the melt but does not reduce supercooling adjacent to the growth interface. The ACRT schedule derived for stable Ekman flow, with lower rotation rates, proves more effective in reducing supercooling and promoting stable growth. These counter-intuitive results highlight the need for more comprehensive studies on the optimization of ACRT schedules for specific growth systems and for desired growth outcomes. Note that many of these results were first published in [134] and reproduced with permission from Elsevier.

7.2 Introduction

As discussed in chapter 1, Capper and co-workers reported substantial improvements in the growth of several II-VI compounds via the use of ACRT. After extensive experimental work and an assessment of the existing body of knowledge concerning rotational fluid dynamics [53], Capper made several recommendations regarding rotation schedule selection [52, 135]. In the present paper, we aim to test the recommendations put forth by Capper via an analysis of the effects of different ACRT schedules on the growth of CZT.

The first of Capper's recommendations is proposed to "maximize flow" in the system by choosing a rotation rate that yields an Ekman thickness of $d_E < 0.05$ cm. This criterion is argued to arise from past experience with ACRT in flux growth methods and to encourage an Ekman flow strong enough to disrupt concentration boundary layers. Applied to the WSU system (with $\nu = 8\text{x}10^{-3}$ cm^2/s), this yields a rotation rate of 30.6 revolutions per minute (RPM), so we choose $\Omega_0 = 31$ RPM. This rotation rate has a corresponding Ekman time scale in this system of $\tau_E = 20.2$ seconds. Capper also argues that, to promote strong Ekman flows, short acceleration and deceleration times are appropriate, namely $\tau_a, \tau_d \ll \tau_E$, and that the steady rotation and stopped periods should be on the order of the Ekman time scale, $\tau_r = \tau_s \approx \tau_E$. Accordingly, we choose $\tau_a = \tau_d = 5$ seconds and $\tau_r = \tau_s = 20$ seconds. These parameters will be used for ACRT case 1 in subsequent model computations. We note that this rotation rate yields a value of the rotational Reynolds number of $\text{Re}_\Omega \approx 4,300$. These rotation schedules are vastly different than the one presented in Chapters 5 or 6.

Capper also cautioned that too strong of a driving force can destabilize the Ekman flow and proposed an additional criterion "which maintains stable Ekman flow" by limiting the rotation to a rate that yields $\text{Re}_{rot} \leq 500$. While the specific source for this recommendation is not clear [53], there have been many studies of flow driven by a large, steadily rotating disk that confirm that the Ekman layer becomes unstable to disturbances when the Rotational Reynolds number exceeds several hundred; see, e.g., [136]. For the WSU system, $\text{Re}_{rot} \leq 500$ permits a maximum rotation rate of 3.6 RPM, and we choose a second ACRT schedule with $\Omega_0 = 3$ RPM. This yields a rotational Reynolds number of $\text{Re}_{rot} \approx 420$ and a characteristic Ekman time scale of

$\tau_E = 64.8$ seconds. Thus, an acceleration/deceleration timescale of $\tau_a = \tau_d = 5$ seconds is chosen, and a constant/stopped time scale is chosen to be $\tau_r = \tau_s = 64$ seconds. These parameters constitute ACRT case 2.

7.3 Results

We are particularly interested in constitutional supercooling, which arises in this system by the segregation of tellurium at the growth interface [125]. In the following results, contours associated with thermal supercooling are calculated using the local composition and temperature values as described in Chapter 2. We assert that supercooling of the melt likely exacerbates the nucleation of new grains and the capture of tellurium-rich inclusions via morphological interface instabilities. Thus, our primary objective is to ascertain which growth conditions minimize the extent of supercooling.

The calculations were done with an effective furnace profile described in section 2.2 applied as a radiative heat transfer boundary condition. All material and system parameters are defined in Tables 4.1 and 4.2. All subsequent figures show the streamlines, concentration field, temperature field, and thermal supercooling and are plotted with identical color scales for the different cases, with blue corresponding to the minimum and red to the maximum values. Plots of the streamlines are created with 100 contour lines between $\psi_{min} = -0.01481\ cm^3/s$ and $\psi_{max} = 0.008009\ cm^3/s$. The tellurium concentration plots are created using $C_{min} = 54.6489\ at\%$ and $C_{max} = 55.4442\ at\%$. The temperature field plots are created with 100 isotherm contours with $T_{min} = 1274K$ and $T_{max} = 1326K$. Lastly, thermal supercooling, which corresponds to the deviation from the composition-dependent melting point, is plotted using 100 contours between a minimum value of $\Delta T_{min} = -2.286K$ (blue) and a maximum value of $\Delta T_{max} = 0K$ (red).

7.3.1 Growth without rotation: Case 0

Figure 7.1(a) shows the streamlines (left) and concentration field (right) after approximately 20 hours of growth with no rotation. A two-vortex flow structure is observed via the streamlines, which arises as a consequence of thermal buoyancy effects. An upper, clockwise vortex is created due to heating from the side wall, and a counter-clockwise,

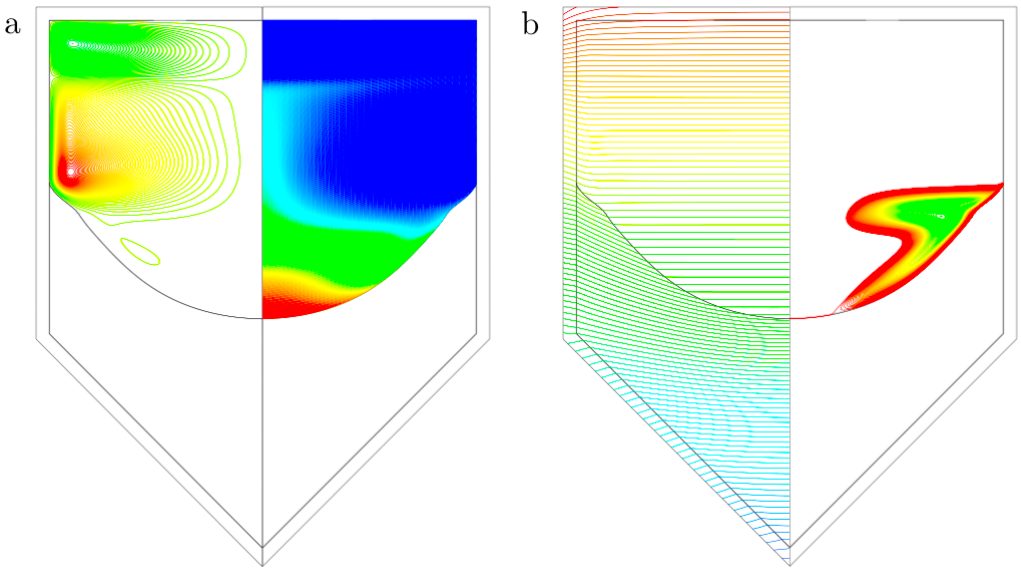

Figure 7.1: Growth from an initially constant-composition melt, without rotation, after approximately 20 hours. (a) Streamlines (left) show a thermal buoyancy-driven structure, and tellurium concentration field (right) indicates significant segregation has occurred. (b) Temperature isotherms (left) show a mostly linear thermal profile, and thermal supercooling (right) suggests persistent supercooling along the solid-liquid interface.

lower vortex is created due to negative radial thermal gradients (hotter fluid along the centerline) in the melt region neighboring the solid-liquid interface. As the solid grows and the interface moves axially upwards, tellurium is rejected into the melt due to its non-unity segregation coefficient. This accumulation is apparent in the concentration field, with a strong accumulation of Te near the center. The weak, lower vortex sweeps the rejected Te up along the centerline and then outwards towards the side wall.

The temperature isotherms shown in Figure 7.1(b) show the axial flow of heat through the system. Of particular interest is that the solid-liquid interface does not lie along a single isotherm, rather its shape is determined by both the temperature and composition, according to the phase diagram. Importantly, the segregation of tellurium produces a significant region of supercooling in the melt, shown by the supercooling contours on the right. As argued above, such a region of supercooling is likely to promote unfavorable outcomes, such as the loss of single-crystallinity and the formation of tellurium inclusions.

7.3.2 Growth with ACRT: Case 1

After 20 hours of growth without rotation (the outcome of the previous case), ACRT was applied to the system per the case 1 schedule derived above to "maximize flow." Contour plots of the streamlines, concentration field, temperature isotherms, and supercooling are shown in Figure 7.2 after 20 minutes of growth, corresponding to a point during the spin-down portion of the 11th cycle.

Figure 7.2(a) clearly shows the Taylor-Görtler vortices via the streamlines at this point in the rotation schedule, and the cumulative results of ACRT-driven flows are manifest by a tellurium composition field that appears to be mostly homogenized. In addition, the strong flows are significantly affecting heat transfer, as shown by the distorted isotherms shown in Figure 7.2(b), compared to those of the prior case with no rotation shown in Figure 7.1(b). Indeed, based on the maximum melt velocity in the meridional plane, a thermal Peclet number, assessing the relative importance of convective to conductive heat flows, is computed to be $\mathrm{Pe} = 1.8 \times 10^3$ for the ACRT case, compared to a value of $\mathrm{Pe} = 7.8$ for the no-rotation case.

Significantly, in spite of the near-homogenization of the melt composition, supercooling still exists, and is in fact quite large in magnitude as indicated by the dark blue

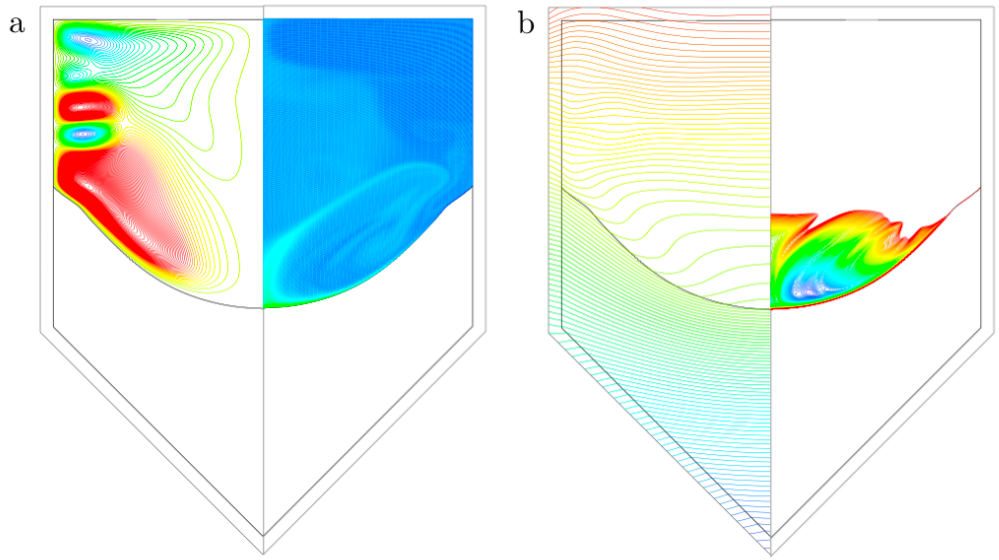

Figure 7.2: Growth from an initial condition shown in Figure 7.1, under flow maximizing conditions according to case 1, corresponding to a point in the cycle during spin down of the 11th cycle (approximately 20 minutes after application of ACRT). (a) Streamlines (left) show the characteristic Taylor-Görtler instabilities, and concentration field (right) indicates almost complete homogenization has occurred in the melt. (b) Temperature isotherms (left) are significantly spaced apart, showing mixing effects on the thermal field, while thermal supercooling (right) is strengthened compared to the case without rotation.

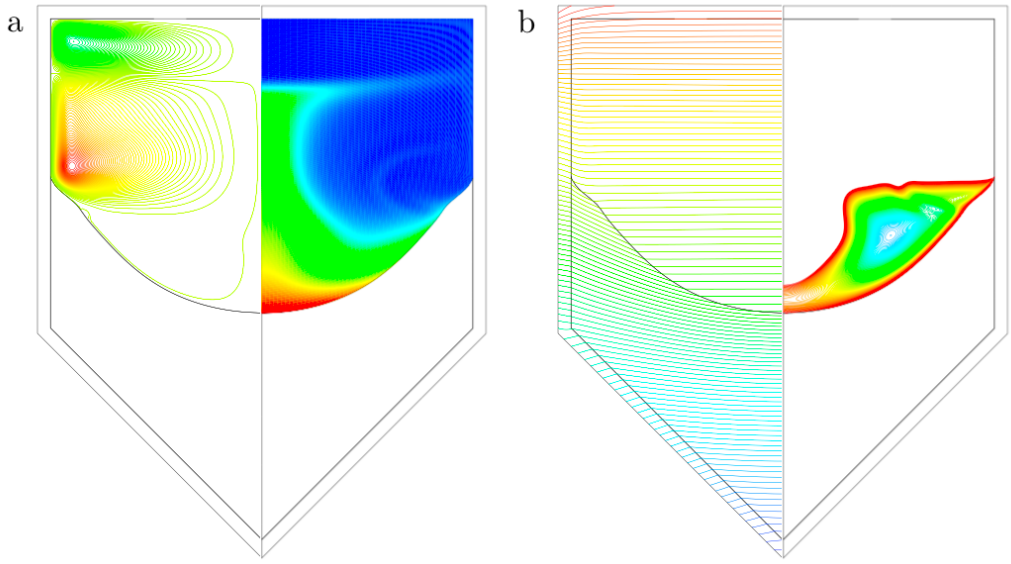

Figure 7.3: Growth from an initial condition shown in Figure 7.1, under Ekman flow stabilizing conditions according to case 2, corresponding to a point during the stopped regime in the 4th cycle (approximately 20 minutes after application of ACRT). (a) Streamlines (left) show a thermal buoyancy-driven flow structure, and concentration field (right) is marginally better mixed than in the no-rotation case. (b) Temperature isotherms (left) and thermal supercooling (right) are similar in shape and magnitude to the no-rotation case.

contours, which correspond to larger deviations from the melting point. The region of supercooling is located over the central portion of the interface in this snapshot of the system; however, this region moves across the interface in a time-dependent manner as the Ekman layer oscillates between inward- and outward-flowing directions as discussed in Chapter 6.

7.3.3 Growth with ACRT: Case 2

The same system (20 hours of growth without rotation) is examined after ACRT is applied, with conditions specified by case 2. Figure 7.3 show streamlines, concentration field, isotherms, and supercooling contour plots after approximately 20 minutes of growth, corresponding to a point during the stopped regime in the 4th ACRT cycle.

Much weaker flows are driven by the ACRT case 2 parameters, and this is reflected

by both the melt flow streamlines and the Te composition field shown in Figure 7.3(a), which are very similar to those of the case without applied rotation shown in Figure 7.1(a). Unlike under the previous case, the rotational Reynolds number for case 2 is not strong enough to induce Taylor-Görtler instabilities. Moreover, the results in Figure 7.3(b) show that the ACRT-driven flows do not substantially affect heat transfer but are strong enough to influence the Te composition in the melt, giving rise to slightly lower concentrations at the growth interface. Lastly, the supercooled region has taken on a similar morphology to the no-rotation case, yet its magnitude and size have grown in comparison. However, not shown by this snapshot in time, the supercooled melt region grew and shrank as it was convected across the interface by Ekman flows.

7.4 Discussion

We have asserted in Chapter 6 that the classical idea of complete mixing driven by ACRT is too simple and that the primary stabilization in this system occurs via Ekman flows sweeping supercooled liquid away from the interface, replacing it with a layer of thermally stable (superheated) fluid. Furthermore, we have posited that this stable fluid may momentarily ameliorate interface instability and, averaged over time, may prevent the formation of deep cells and tellurium inclusions.

Calculation of the total stabilized area, A_t, as described in Chapter 6, can be applied here to judge improvement via ACRT over time. Figure 7.4 indicates the percentage of the interface that is stable, as locally assessed via the classic Mullins and Sekerka criterion [126] over time for each simulation. Slightly more than half of the interface is stable for the case of continued growth without rotation (case 0), with the supercooled melt persisting in the form depicted in Figure 7.1 (b). The fractions of stable interface for cases 1 and 2 oscillate dramatically in phase with their respective rotation schedules, indicating that Ekman flows are responsible for creating periods of stability and periods of instability. However, it is clear that the case 2 rotation schedule results in significantly higher fractions of stabilized interface than that produced by case 1 parameters. Clearly, although the 3 RPM case is not strong enough to homogenize the melt, it does a better job of creating periods of where most ($\sim$80–90%) of the interface is under stabilizing conditions.

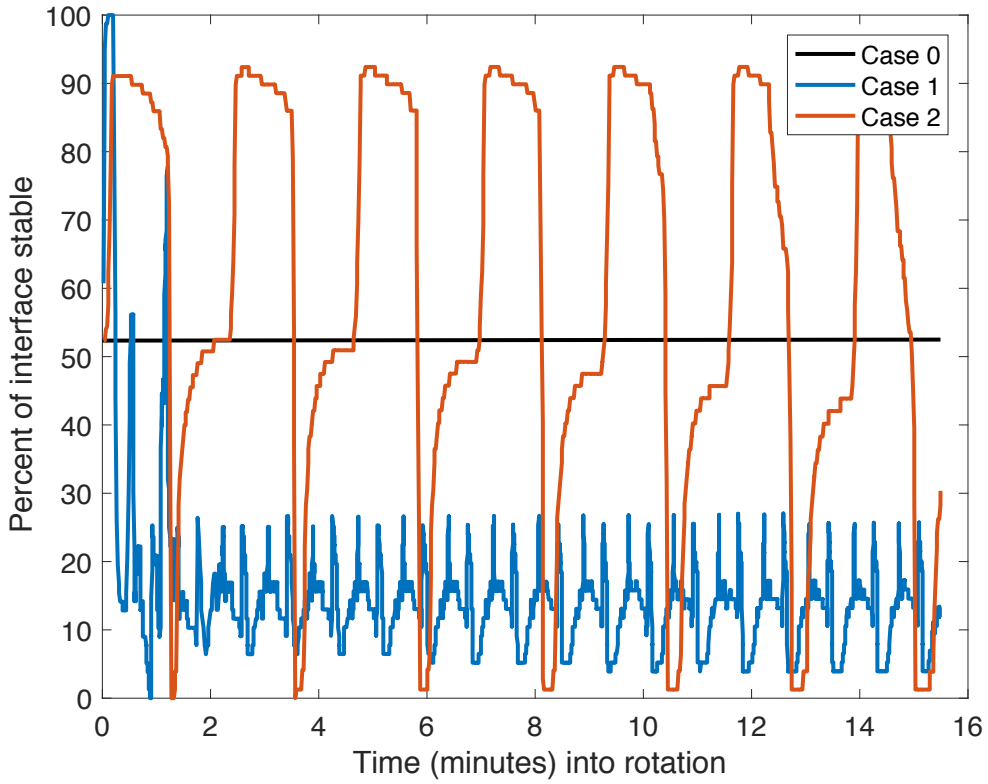

Figure 7.4: Percent of the solidification interface that is stable, according to the Mullins and Sekerka criterion, as a function of time. Case 0 represents growth with no rotation, integrated from the state depicted in Figure 7.1. Cases 1 and 2 correspond to ACRT schedules with maximum rotation rate of 31 RPM and 3 RPM, respectively.

7.5 Conclusions

We have evaluated two rotation schedules by applying Capper's recommendations [52] to the WSU growth system for CZT. Under the "flow maximizing" conditions (ACRT case 1), significant homogenization of the concentration was achieved in the melt; however, in spite of this mixing, significant supercooling persisted. Under the Ekman "flow stabilizing" conditions (ACRT case 2), the tellurium concentration was not nearly as well-mixed as in case 1. Nevertheless, an assessment of the sold-liquid interface with time demonstrated that the milder rotational schedule of case 2 resulted in more stabilization and would, therefore, likely result in higher-quality material than both the non-ACRT and flow maximizing cases. Clearly, the outcomes of ACRT are far more complicated than classical wisdom dictates, necessitating a much deeper assessment of the mechanistic working and outcomes of this technique.

In the next chapter, these learnings are extended to the large-scale comparison of rotation schedules via factorial design. We systematically assess the relative importance of each component of the rotation schedule and investigate the trends of changing one component while holding the others constant. This not only provides us with an optimal rotation schedule for the WSU system, but it will also help elucidate the results discussed in the present chapter.

Chapter 8

A Factorial Approach to Optimize Rotation Schedules

8.1 Summary

We present a series of numerical calculations that reveal insight into the important parameters that govern the accelerated crucible rotation technique (ACRT) applied to the gradient freeze growth of cadmium zinc telluride (CZT). A metric is designed based on the classic Mullins and Sekerka criterion that allows for the quantitative comparison of rotation schedules over multiple cycles. This metric is first employed in a 2-k factorial design of experiments which highlights the maximum rotation rate as the most important parameter, followed by the acceleration period and the rest period. Next, these parameters are systematically varied over a wide range of values. Improved interface stability is achieved with weaker rotation rates and longer acceleration periods, while the influence of the rest period is highly dependent on the maximum rotation rate.

8.2 Introduction

Information regarding the selection of an optimal rotation schedule for a particular growth system is lacking. This is due in part to the high cost of material preventing large optimization experiments, and also in part to the challenge of quantitatively determining "better" results from a computation. Moreover, as the previous chapter motivated,

little work has been done to assess interface stability during ACRT. In this chapter, we present a thermodynamically-based metric that represents the stability of the interface after many cycles and allows for the analysis and optimization of rotation schedules. Computation results are presented with a preliminary mechanistic explanation that support our understandings.

Chapter 6 presented the preliminary calculations of a metric based on the Mullins and Sekerka stability criterion. In short, the propensity of the interface to be morphologically unstable is calculated at every point along the interface as a function of the thermal gradients in the liquid and solid and concentration gradient in the liquid. This value, referred to as s, varies in both space and time. To capture the spatial variations, the percentage of total interface area that is stabilized is calculated to determine the amount of interface under stabilizing conditions. This value, referred to as A_t, oscillates in phase with the rotation schedule. While this is useful for the assessment of a single rotation schedule, further manipulation would be useful in order to consider the effects of time.

In follow up from the discussion on this topic in Chapter 6, periods of destabilization may be reversed if stabilizing conditions persist long enough. In an attempt to account for this healing effect in a simplified manner, the length of time under stabilizing conditions is compared to the length of time under destabilizing conditions. By subtracting the latter from the former and dividing it by the total time, a metric is created that measures the ability of an ACRT cycle to heal an unstable interface. The following conditions are assigned: if at any point in time, more than 85% of the interface is stable, it is under stabilizing conditions; and if less than 15% of the interface is stable, it is under destabilizing conditions. Although these values are somewhat arbitrary, they were found through trial and error to best differentiate between rotation schedules. This metric will furthermore be referred to as the M-value, and its calculation is defined with pseudo code in Algorithm 1. Although this value neglects any kinetic effects, i.e. how fast an instability grows or heals, it provides a cursory understanding of how the stability is changing over multiple cycles. Of great importance to the implementation of this metric is the time step, Δt, chosen for the simulations. The value of Δt must be small enough such that significant variations within a cycle can be precisely measured. A good rule of thumb is to select Δt to be an order of magnitude smaller than the shortest period

in the rotation schedule.

Algorithm 1 M-value calculation

```
1: procedure M-VALUE(A_t)
2:     h ← 0                          ▷ This counter will track healing or stabilizing states
3:     d ← 0                          ▷ This counter will track destabilizing states
4:     for time = t_i : t_f do        ▷ Iterate through time points
5:         if A_t > 0.85 then
6:             h ← s + 1              ▷ Increase s-counter when above 85% stable
7:         if A_t < 0.15 then
8:             d ← d + 1              ▷ Increase d-counter when below 15% stable
9:     M-Value ← (h − d) / (t_f − t_i)   ▷ Calculate final M value
```

A negative M-value signifies that most of the simulation is spent under destabilizing conditions, suggesting that the ACRT schedule is likely exacerbating an instability. We believe this indicates that an unstable cellular morphology would arise and lead to the unfavorable entrapment of tellurium-rich material. Via this argument, largely negative M-values will determine worse rotational schedules. An M-value that is greater than zero signifies that the majority of the simulation is spent under stabilizing conditions, meaning that the ACRT schedule is effective in disrupting the local conditions. Through this mechanism, the interface has a chance to re-stabilize and heal itself. Via this argument, large positive M-values determine better rotational schedules. In this form, this metric can be used to quantitatively compare rotation schedules after the application of multiple ACRT cycles.

8.3 Statistical analysis

In selecting a rotation schedule, there are five traditional parameters to consider: the maximum rotation rate the system will reach (Ω_0), the length of time to accelerate to the maximum rotation rate (τ_a), the length of time held at the maximum rotation rate (τ_r), the length of time to decelerate down to zero (τ_d), and the length of time held at rest (τ_s). This is then repeated in the reverse direction, making up a full cycle. A sample rotation schedule identifying these regimes is shown in Figure 8.1. A brief survey of the literature indicates that a wide range of parameters have been employed in designing rotation schedules. Maximum rotation rates vary from 3 to 90 RPM, and time intervals

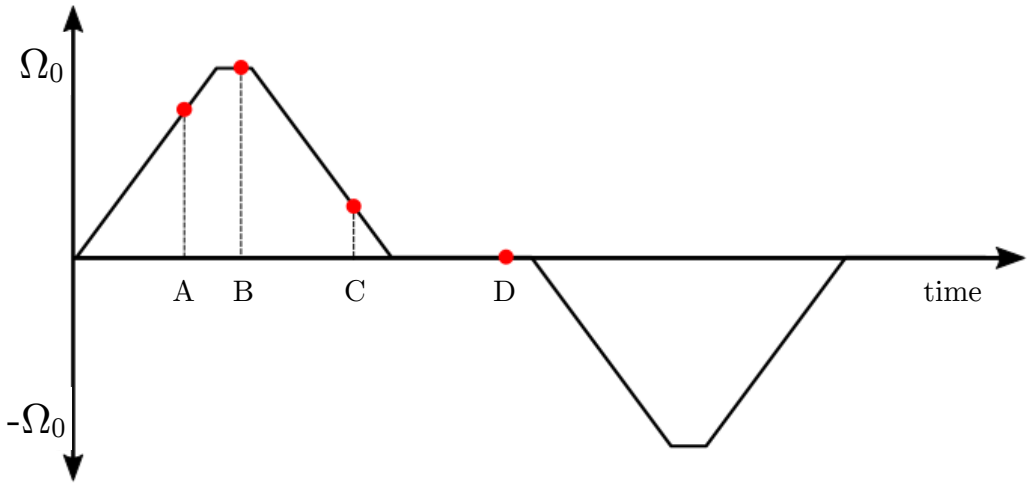

Figure 8.1: Schematic of a rotation schedule with the following regimes identified by the markers in red: A) τ_a, B) τ_r, C) τ_d, and D) τ_s.

for each period vary from 0-180 seconds [51,63]. It is therefore challenging to intelligently select an optimal rotation schedule given such a large range. Moreover, traversing a five-dimensional parameter space to find the optimal schedule with simulations would be computationally expensive. Thus, in order to assess the relative importance of each parameter of the rotation schedule, a 2-k factorial design of experiments is employed.

The procedure begins with the selection of a characteristically high and low value for each of the five parameters of interest. These are summarized in Table 8.1, and were selected since they are representative of the range previously employed in experiments performed at Washington State University (WSU). This creates $2^5 = 32$ combinations of parameters that make up 32 unique rotation schedules. Each of these is applied to an initial condition of $\sim$ 18 hours of steady growth, and allowed to run for 1.6 hours of rotation with a time step of 1.3 seconds. The total length of time is chosen as it allows for 12 full cycles of the longest rotation schedule to be performed. After 1.6 hours, the M-value described above is determined. A main effect value for each parameter is then calculated via the following equation:

$$\text{Main effect of parameter i} = \text{avg}(y_{i+}) - \text{avg}(y_{i-}), \tag{8.1}$$

Table 8.1: 2-k Factorial Experimental Design Variables: Definitions of High and Low Values

Component	**LowValue**$(-)$	**HighValue**$(+)$
Max RPM, Ω_0	3 RPM	10 RPM
Time to accelerate, τ_a	15 sec	60 sec
Time at constant rotation, τ_r	15 sec	60 sec
Time to decelerate, τ_d	15 sec	60 sec
Time at rest, τ_s	15 sec	60 sec

where y_{i+} represents all the M-values for which parameter i is at its high value, and y_{i-} represents all the M-values for which parameter i is at its low value. The main effect measures the response in the interface stability due to a change from a low to a high value of parameter i. If the main effect is relatively large and positive, it means that a change in parameter i from low to high resulted in a highly stabilizing effect on the interface. Conversely, if the value is relatively large and negative, a change from low to high resulted in a highly destabilizing effect on the interface. A small value corresponds to a minimal impact on the system. Although this technique assumes the system has a linear response to changes in input parameters, we believe the application of this technique can lend insight into the relative importance of each parameter. We refer the interested reader to [137] for further details of this technique.

8.4 Results

The main effect of each parameter is calculated via Equation 8.1 and presented in Figure 8.2. From this graph, it is clear that Ω_0 has the largest influence on the stability of the system. The relatively large, negative value associated with this parameter suggests that a change from $\Omega_0 = 3$ RPM to $\Omega_0 = 10$ RPM has a highly destabilizing influence on the interface. The remaining four parameters have relatively low positive impacts on the system, which would indicate that adjusting from $\tau = 15$ seconds to $\tau = 60$ seconds has a moderately stabilizing influence on the interface. From inspection, it appears τ_a and τ_s have marginally higher values than τ_r and τ_d.

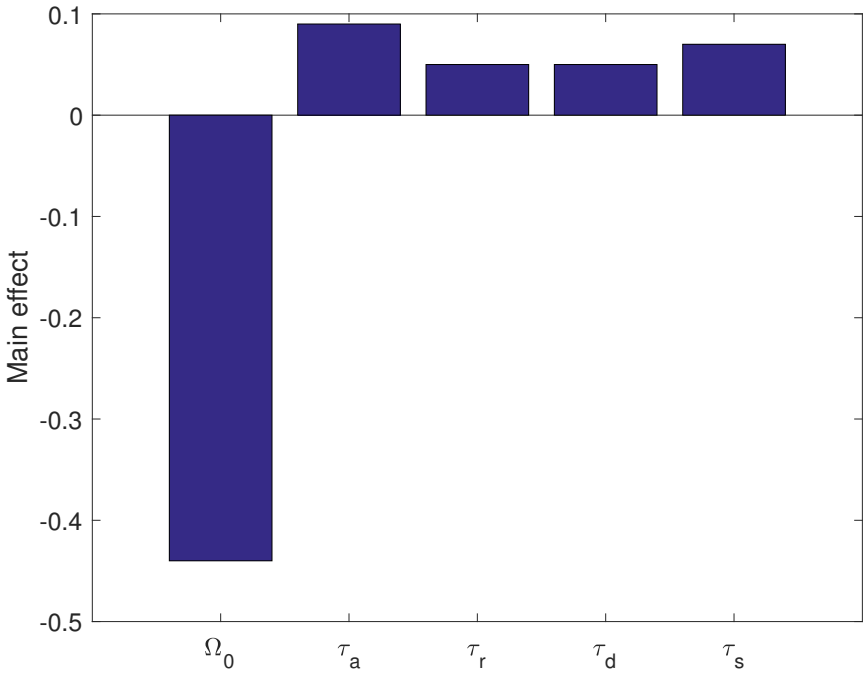

Figure 8.2: Graph of the main effect, defined in Equation 8.1, of each parameter on the interface stability: the maximum rotation rate (Ω_0), the time allowed to accelerate (τ_a), the time spent at the maximum rotation rate (τ_r), the time allowed to decelerate (τ_d), and the amount of time spent at zero rotation (τ_s).

8.5 Discussion

8.5.1 Effect of maximum rotation rate

To further assess and understand the nonlinear influence these parameters have on the interface stability, additional studies are performed systematically varying one parameter at a time. Ω_0, which is calculated to have the largest influence on the system, is varied from 1 to 30 RPM. This range was selected to best span the values used in the literature; however, rotation rates past 30 RPM could not be converged without changing the mesh. The M-value is calculated after 1.6 hours for each case and plotted in Figure 8.3.

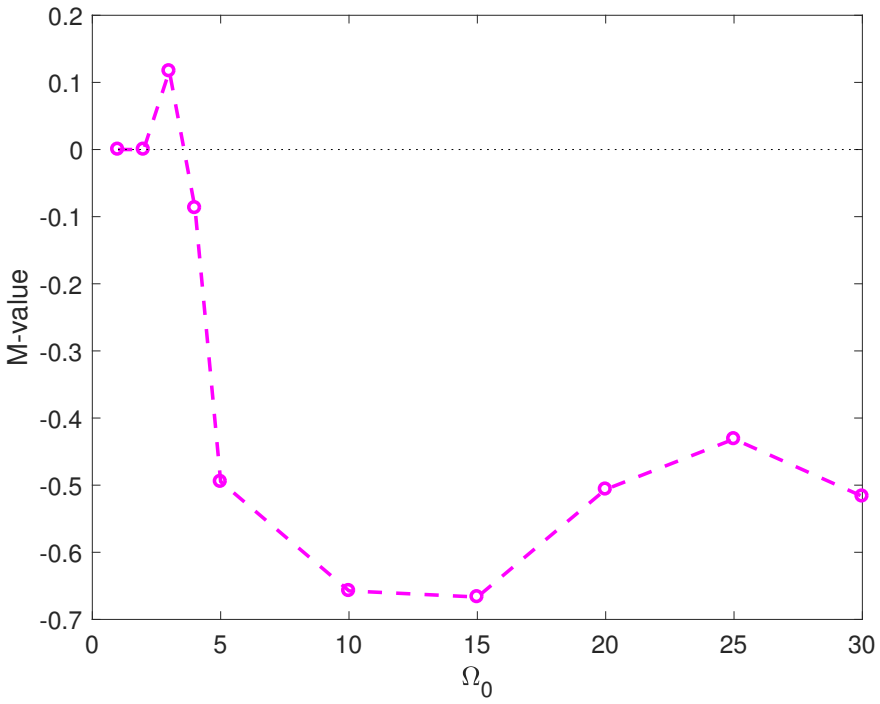

Figure 8.3: The circles represent calculated M-values after 1.6 hours of rotation. M-values correspond to the ACRT cycle's ability to heal itself, with M-values above zero indicating that the majority of the simulation was spent under stabilizing conditions. The following rotation schedule was used for all simulations: $\tau_a = 60sec$, $\tau_r = 15sec$, $\tau_d = 60sec$, and $\tau_s = 60sec$, while Ω_0 varied from 1 to 30 RPM.

We aim to explain why, for this system, we observe such a nonlinear trend in behavior. At Ω_0 = 1-2 RPM, the M-value is zero. Such low rotation rates are not strong enough to significantly perturb the local conditions to adjust the interface stability. The most stability is achieved at $\Omega_0 = 3$ RPM with the only positive M-value.

Contour plots of the concentration (left) and supercooled fluid (right) are presented in Figure 8.4 to explain why $\Omega_0 = 3$ RPM is favored. The following rotation schedule is employed for the figures: $\Omega_0 = 3$ RPM, $\tau_a = \tau_d = \tau_s = 60$ seconds, and $\tau_r = 15$ seconds. Figures 8.4a-8.4d correspond to the time points specified in Figure 8.1 for the 10th cycle applied after $\sim$ 18 hours of steady growth. Contour plots showing streamlines and temperature are omitted for brevity, and much of the behavior is consistent with the previous work presented in Chapters 5 and 7. As the crucible is accelerated in Figure 8.4a, Ekman flow sweeps concentrated material towards the side wall along the interface. This effect is subtle due to the weak rotational flow characterized by a rotational Reynolds number of 415. The supercooling (right) is mostly unperturbed from the initial condition. However, as the system is held at $\Omega_0 = 3$ RPM in Figure 8.4b, a thin boundary layer of superheated fluid is apparent along the interface due to local changes in the composition field. As the system decelerates down to zero in Figure 8.4c, the Ekman flow reverses direction, sweeping less concentrated fluid towards the center. During this period, supercooled fluid persists along the entirety of the interface. As the system is held at rest in Figure 8.4d, the Ekman flows dissipate and the supercooling has retained its initial structure.

Throughout the cycle, the local interface velocity changes upon readjustment of the local gradients. A plot of the spatially averaged interface velocity as a function of time is shown in Figure 8.5 in blue for $\Omega_0 = 3$ RPM. During the acceleration and constant periods, Ekman flow pushes higher concentrated material across the interface towards the side wall. This subtle effect is depicted in Figures 8.4a and 8.4b. This reduces the solidification temperature corresponding to the phase diagram, reducing the interface velocity. This is observed with a dip in the velocity of 0.38 mm/hr. A reduced interface velocity decreases the driving force for segregation, subsequently reducing the amount of supercooled fluid. This stabilizing effect is quantified by the fraction of stabilized interface, A_t, plotted in Figure 8.6, where the interface is 90% stabilized during acceleration and constant rotation. This is corroborated by the contour plot of the supercooling in

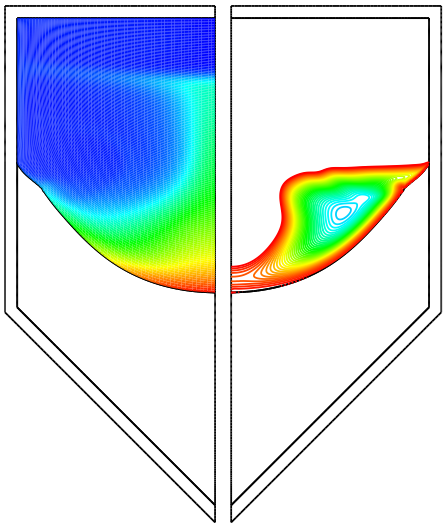

(a) Time point A (acceleration period).

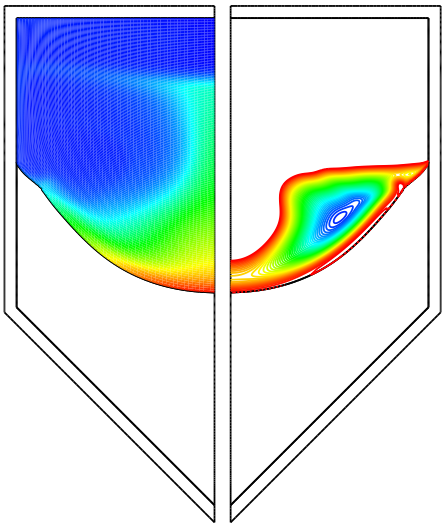

(b) Time point B (constant period).

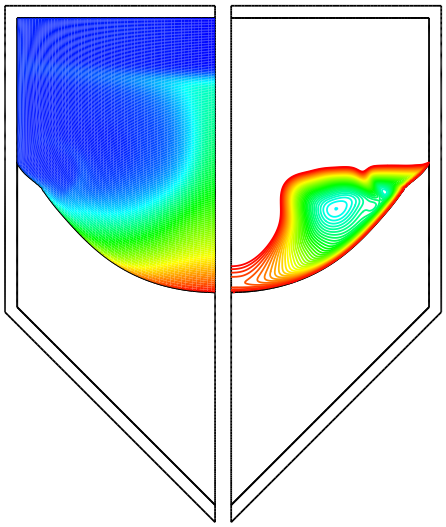

(c) Time point C (deceleration period).

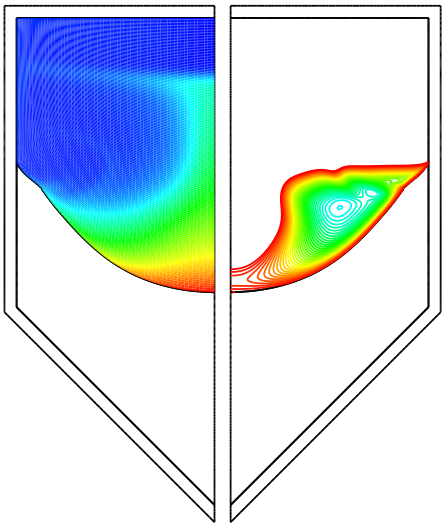

(d) Time point D (rest period).

Figure 8.4: Contour plots for the 10th cycle of the following rotation schedule: $\Omega_0 = 3RPM$, $\tau_a = \tau_d = \tau_s = 60$ sec and $\tau_r = 15$ sec. Time points are defined in Figure 8.1. Concentration (left) and supercooling contour lines (right) are shown with the following extrema: $C_{min} = 54.71$ at%, $C_{max} = 55.52$ at%, $\Delta T_{min} = -1.97$ K and $\Delta T_{max} = 0$ K.

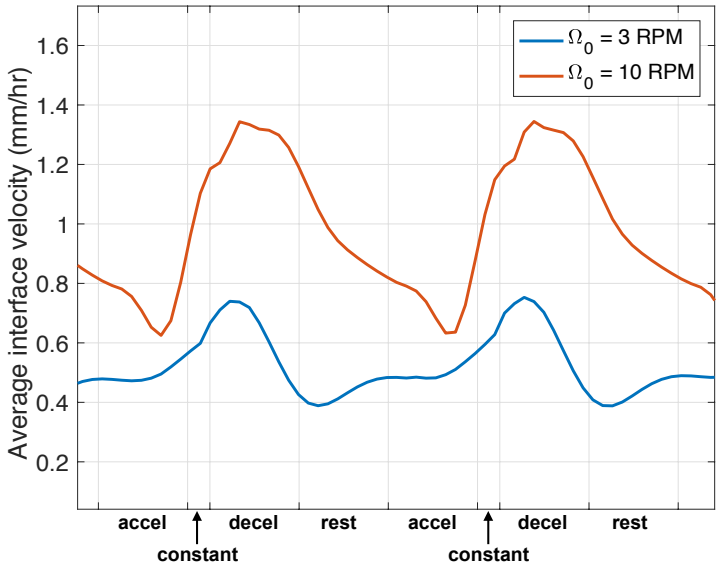

Figure 8.5: The average interface velocity at the beginning of the 10th cycle. $\Omega_0 = 3$ RPM, plotted in blue, has an average interface velocity of 0.52 mm/hr and $\Omega_0 = 10$ RPM, plotted in red, has an average interface velocity of 0.92 mm/hr.

Figure 8.4b, where a thin boundary layer of stabilized fluid exists in front of the interface that has been created due to a reduction in segregation. Upon deceleration, Ekman flow sweeps less concentrated fluid across the interface towards the center, which increases the corresponding melting point temperature. This creates a driving force for growth, and a spike in the interface velocity of 0.75 mm/hr is observed in Figure 8.5. This increases the segregation of tellurium, which exacerbates the supercooling, as observed in the decrease in stability to 4% in Figure 8.6. This is corroborated by the supercooling field in Figure 8.4c where the interface is almost entirely covered by supercooled fluid. With the lack of rotation, the rest period retards the growth to a velocity of 0.49 mm/hr, which corresponds to a moderate stabilizing effect whereby 45% of the interface is stabilized.

Many of these effects are exacerbated at $\Omega_0 = 10$ RPM. Contour plots at identical time points are shown in Figure 8.7, with concentration on the left and supercooling on the right. The following rotation schedule is employed: $\Omega_0 = 10$ RPM, $\tau_a = \tau_d =$

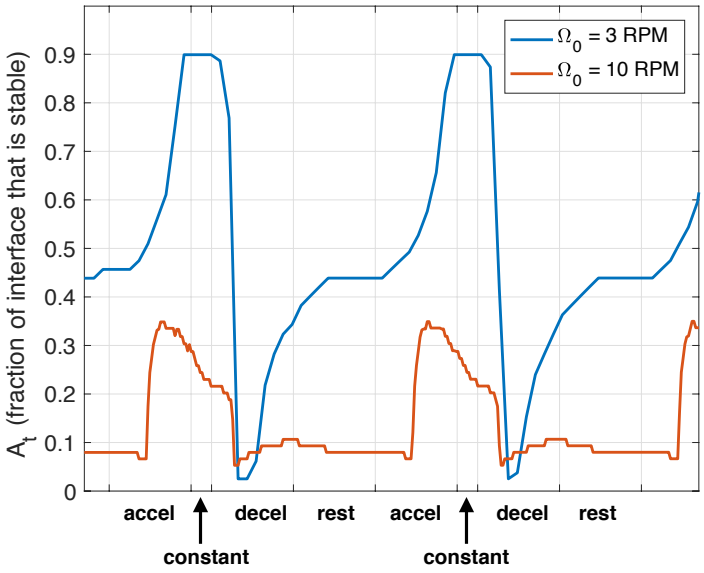

Figure 8.6: The fraction of the interface that is stabilized, A_t, for $\Omega_0 = 3$ RPM and $\Omega_0 = 10$ RPM.

$\tau_s = 60$ seconds, and $\tau_r = 15$ seconds. The average interface velocity and the fraction of stabilized interface are shown in red in Figures 8.5 and 8.6, respectively.

As the crucible is accelerated in Figure 8.7a, Ekman flow develops, sweeping highly concentrated fluid across the interface towards the side wall. Given the higher rotational Reynolds number of 1380, the Ekman flow is able to propagate this fluid across the entirety of the interface, and this is clearly seen in Figure 8.7a. This increase in composition reduces the solidification temperature, reducing the driving force for growth. Subsequently, a minimum interface velocity of 0.63 mm/hr is observed during this period. This reduction in velocity decreases the driving force for segregation, thus slightly improving the supercooling and improving the overall stability of the interface. Figure 8.6 shows a maximum of 35% of the interface stabilized during acceleration, and this is supported by the supercooling contour plot in Figure 8.7a which shows the interface near the side wall is not supercooled. As the system is held at a constant rotation rate, the interface velocity begins to increase to 1.0 mm/hr due to the recent reduction of the composition in the previous period. This begins to increase segregation, and the

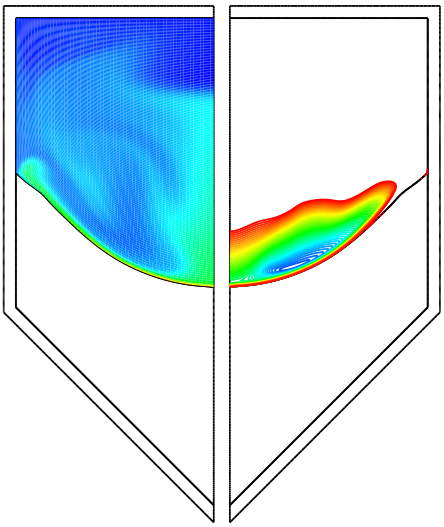

(a) Time point A (acceleration period).

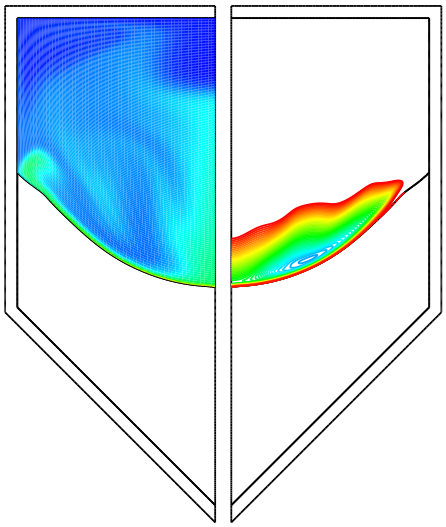

(b) Time point B (constant period).

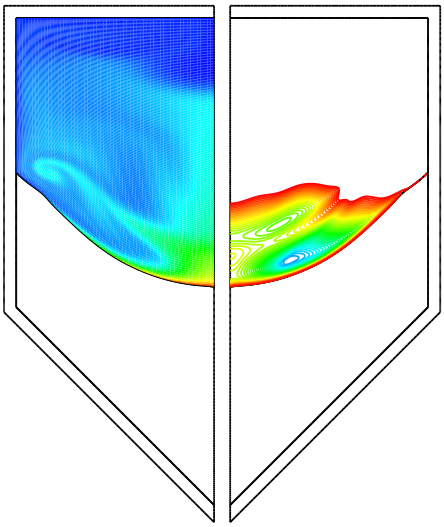

(c) Time point C (deceleration period).

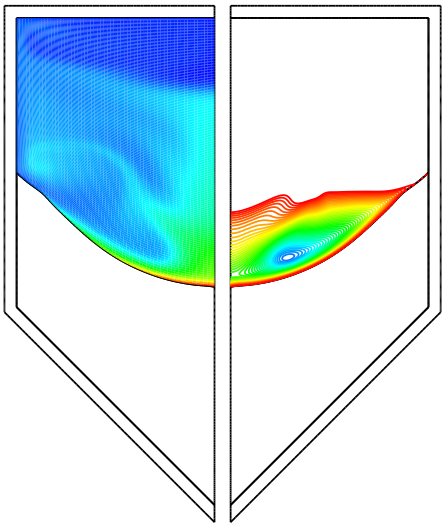

(d) Time point D (rest period.

Figure 8.7: Contour plots for the 10th cycle of the following rotation schedule: $\Omega_0 = 10RPM$, $\tau_a = \tau_d = \tau_s = 60$ sec and $\tau_r = 15$ sec. Time points are defined in Figure 8.1. Concentration (left) and supercooling contour lines (right) are shown with the following extrema: $C_{min} = 54.77$ at%, $C_{max} = 55.33$ at%, $\Delta T_{min} = -4.01$ K and $\Delta T_{max} = 0$ K.

stability begins to decrease. Supercooling continues to persist along the interface in Figure 8.7b. This effect is exacerbated as the system is decelerated. During deceleration, Ekman flow sweeps less concentrated fluid back towards the center as depicted in Figure 8.7c, increasing the solidification temperature. This increases the driving force for growth, thus segregating more tellurium and exacerbating the supercooling. A maximum velocity of 1.35 mm/hr is observed in this period with only 6% of the interface stabilized in Figure 8.6. A significant amount of supercooled fluid has been created due to this rapid growth, which is observed closest to the interface in Figure 8.7c. As the system is held at rest, the interface velocity decreases to 0.82 mm/hr while the only 9% of the interface remains under stabilizing conditions. This mild improvement is observed in Figure 8.7d with a subtle reduction of the supercooling.

Overall, the $\Omega_0 = 3$ RPM case has a temporally averaged interface velocity of 0.52 mm/hr, while the $\Omega_0 = 10$ RPM case has a temporally averaged interface velocity of 0.92 mm/hr. Over time, the higher interface velocity in the latter case segregates more tellurium, which exacerbates the supercooling. This is confirmed via comparison of the extrema of supercooling in each case: after 10 cycles, the 3 RPM case has a minimum of $\Delta T = -1.97K$ while the 10 RPM case has a minimum of $\Delta T = -4.1K$. Moreover, the 10 RPM velocity oscillates more dramatically than the 3 RPM case, with a standard deviation of 0.51 mm/hr compared to 0.13 mm/hr, respectively. Larger oscillations will create periods where the supercooling is further worsened, thus increasing the propensity to form a morphological instability. The 3 RPM case is favored because it is just strong enough to induce a stabilizing effect via the Ekman flows during acceleration, while not being so strong as to negatively affect the interface velocity. While these exact values are only applicable to the system at hand, these results support the idea that the system can in fact be rotated too quickly, and a compromise must be identified where the Ekman flow is maximized while changes to the velocity are minimized.

8.5.2 Effect of acceleration period

Next, τ_a is varied from 5-180 seconds while measuring the M-value after 1.6 hours of rotation. These results are depicted in Figure 8.8a for $\Omega_0 = 3$ RPM. The M-value steadily increases from zero until $\tau_a = 60$ seconds, at which point the M-value plateaus. After $\tau_a = 90$ seconds, the M-value drops and plateaus until 180 seconds.

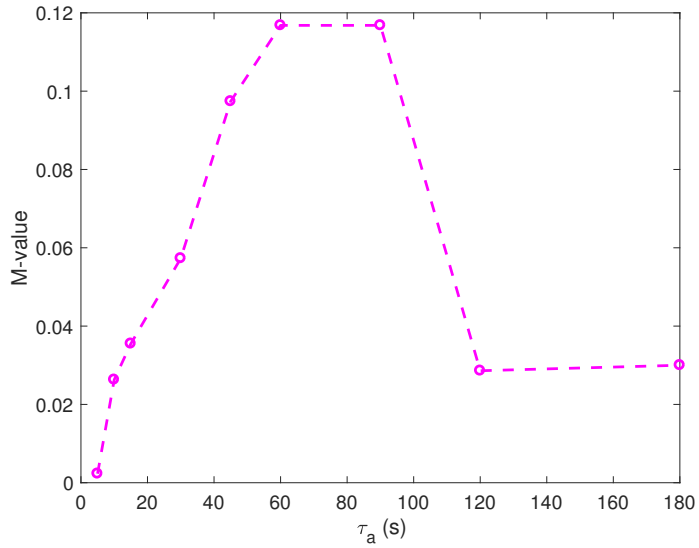

(a) $\Omega_0 = 3RPM$

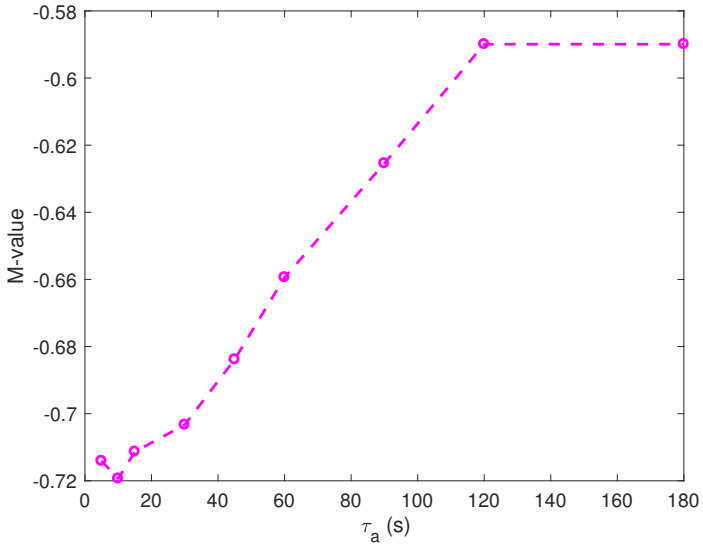

(b) $\Omega_0 = 10RPM$

Figure 8.8: The circles represent calculated M-values after 1.6 hours of rotation. The following rotation schedule was used for all simulations: $\tau_r = 15$ sec, $\tau_d = 60$ sec, and $\tau_s = 60$ sec, while τ_a varied from 5 to 180 seconds.

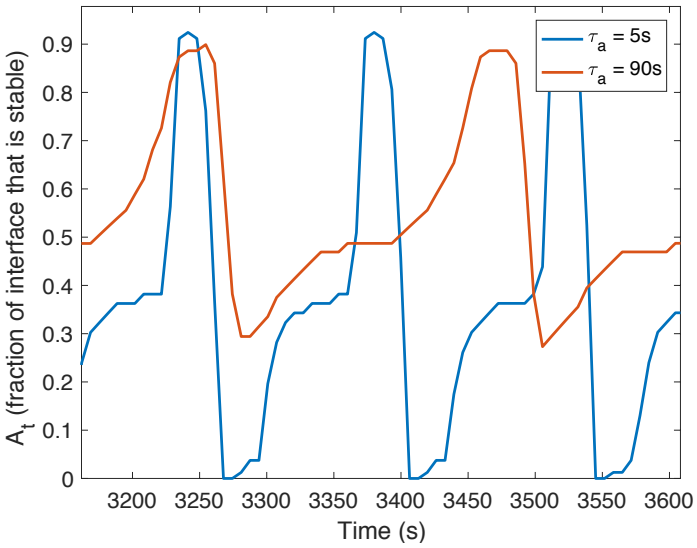

Figure 8.9: The fraction of the interface that is stabilized, A_t, for $\Omega_0 = 3$ RPM after 53 minutes of rotation. $\tau_a = 5$ sec is plotted in blue and $\tau_a = 90$ sec is plotted in red.

These results are best understood via comparison of the fraction of stabilized interface, A_t for the $\Omega_0 = 3$ RPM case. Figure 8.9 shows the comparison of A_t for the $\tau_a = 5$ sec and $\tau_a = 90$ sec cases. While both cases have spikes in the stability near 90% stable during acceleration, the $\tau_a = 5$ sec case dips to nearly 0% stable during deceleration whereas the $\tau_a = 90$ sec case only dips to 29% stable. Analysis of the interface velocity does not explain this discrepancy. Both cases have an average interface velocity of 0.52 mm/hr, with standard deviations of 0.12 and 0.14 mm/hr, respectively. Thus, despite equivalent rotational Reynolds numbers and interface velocities, the longer τ_a value results in improved stability. This indicates that fast acceleration will negatively adjust the solute field — while not changing the interface velocity — yielding worsened supercooling. This is corroborated by contour plots of the composition and supercooling after 1.6 hours of rotation. Figure 8.10(a) shows the results for $\tau_a = 5$ seconds and Figure 8.10(b) the case for $\tau_a = 90$ seconds, both of which have Ω_0 =3 RPM. The concentration plots in both cases appear to retain much of the original structure of the initial condition, indicating the rotation was ineffective in homogenizing the melt. However, the supercooled material in Figure 8.10a has a minimum of -2.02 K, whereas

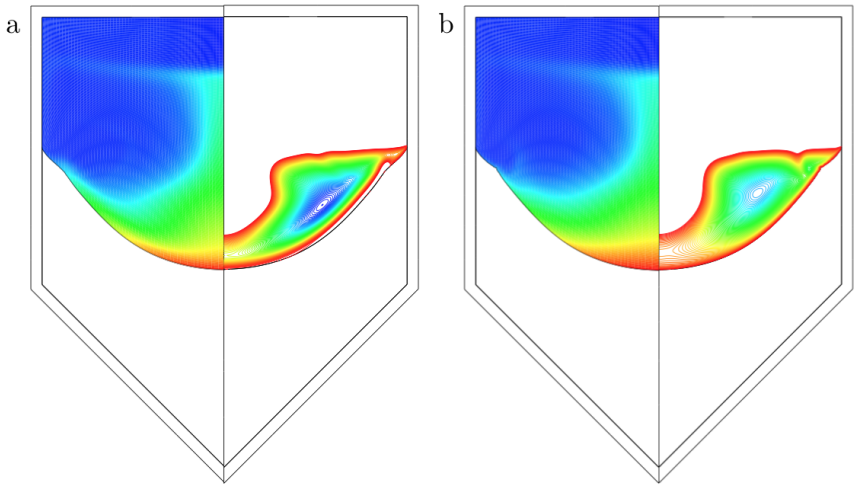

Figure 8.10: Tellurium concentration (left) and supercooled fluid (right) after 1.6 hours of ACRT under the following rotation schedule: $\Omega_0 = 3$ RPM, $\tau_r = 15$ sec, $\tau_d = 60$ sec, $\tau_s = 60$ sec, a) $\tau_a = 5$ sec, and b) $\tau_a = 90$ sec. $C_{min} = 54.76$ at% Te, $C_{max} = 55.59$ at% Te, ΔT_{min} = -2.02 K, $\Delta T_{max} = 0$ K.

Figure 8.10b has a minimum of -1.71 K. The improvement in the latter case supports selecting longer periods of acceleration.

The reduction in M-values at long τ_a values greater than 90 seconds for the 3 RPM case is a consequence of weaker Ekman flows that are less effective in disrupting the local compositional field and subsequently less effective in stabilizing the interface. In the limit of an infinitely long acceleration period where infinitesimal changes are made to the rotation rate during spin up, Ekman flow would not be observed. The cases of $\tau_a \geq 120$ seconds are beginning to approach that limit, which is why the effectiveness begins to drop of at this point.

A similar effect is observed for the comparison of for the case of $\Omega_0 = 10$ RPM. Figure 8.11 shows the fraction of stabilized interface 53 minutes into rotation for a comparison of $\tau_a = 5$ sec and $\tau_a = 90$ sec. While neither values reach over 60% stabilized, the $\tau_a = 5$ sec clearly spends more time under destabilizing conditions. This is due to a compounding of two effects: first, the fast transport of solute near the interface worsens supercooling as in the 3 RPM case. Second, the interface velocities are adjusted, which result in worse supercooling for the shorter acceleration period. The average interface velocities

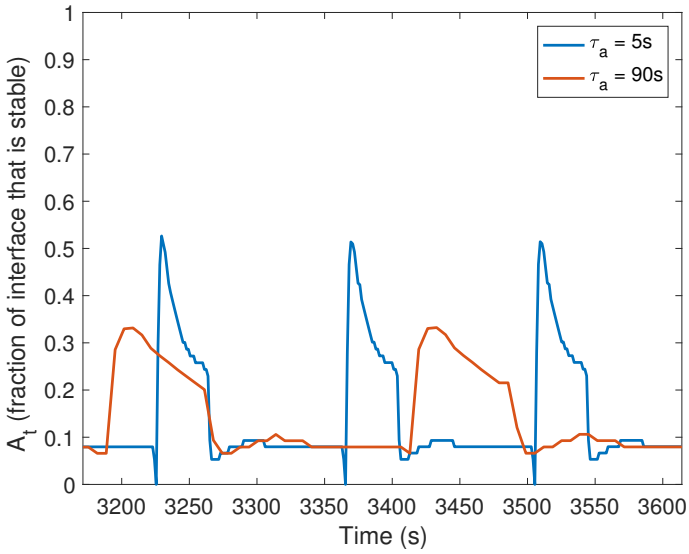

Figure 8.11: The fraction of the interface that is stabilized, A_t, for $\Omega_0 = 10$ RPM after 53 minutes of rotation. $\tau_a = 5$ sec is plotted in blue and $\tau_a = 90$ sec is plotted in red.

for the $\tau_a = 5$ and 90 sec cases are 0.96 and 0.93 mm/hr, respectively. Moreover, the former oscillates with a standard deviation of 0.44 mm/hr and the latter with 0.39 mm/hr. As previously discussed, the larger average velocity and larger magnitude of oscillations will yield worsened supercooling. This is corroborated via a comparison of the composition and supercooling fields after 1.6 hours of growth. Figures 8.12 (a) and (b) depict the concentration field (left) and undercooling (right) for $\tau_a = 5$ seconds and $\tau_a = 90$ seconds, respectively. Both cases are nearly homogenized with respect to tellurium due to the stronger flows. However, the $\tau_a = 5$ seconds case exhibits more a severe supercooling of -3.15 K. In contrast, the $\tau_a = 90$ seconds case has an improved magnitude of supercooling of -2.80 K.

Together with 3 RPM case, these results suggest that prolonging the acceleration period will have an overwhelmingly positive effect on the interface stability via two mechanisms. First, the rapid transport of material across the interface tends to exacerbate the supercooling during the deceleration phase. This effect is compounded by faster and larger oscillations in the interface velocities that are observed for shorter

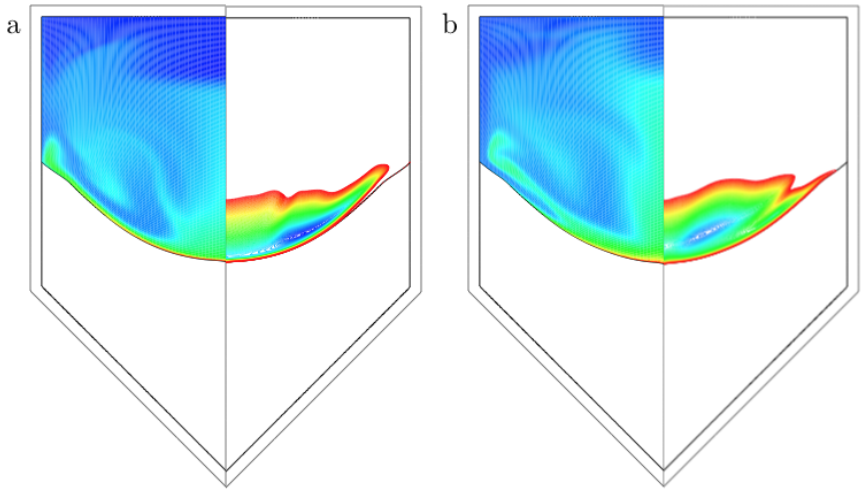

Figure 8.12: Tellurium concentration (left) and supercooled fluid (right) after 1.6 hours of ACRT under the following rotation schedule: Ω_0 = 10 RPM, τ_r = 15 sec, τ_d = 60 sec, τ_s = 60 sec, a) τ_a = 5 sec, and b) τ_a = 90 sec. C_{min} = 54.84 at% Te, C_{max} = 55.31 at% Te, ΔT_{min} = -3.15 K, ΔT_{max} = 0 K.

acceleration periods. Together, they support selecting rotation schedules with gradual acceleration rates that gradually have minimal impact on the solute transport and interface velocities.

8.5.3 Effect of rest period

An identical process is performed for the rest period as it has the third largest influence on the system. This value was also varied from 0-180 seconds. Figures 8.13a and 8.13b show the influence on the M-value after 1.6 hours of rotation for Ω_0 = 3 RPM and Ω_0 = 10 RPM, respectively.

In the 3 RPM case, increasing τ_s increases the M-value with a peak that occurs around τ_s = 90 seconds. A comparison of the fraction of stabilized interface, A_t, is shown for a comparison of τ_a = 0 sec and 90 sec in Figure 8.14. Just like with the acceleration case, the shorter stopped period results in severe dips in the interface stability during deceleration. While both cases have average interface velocities of 0.52 and 0.53 mm/hr, respectively, the τ_s = 0 sec case has a standard deviation of 0.17 mm/hr, while the τ_s = 90s case has a standard deviation of 0.13 mm/hr. This larger

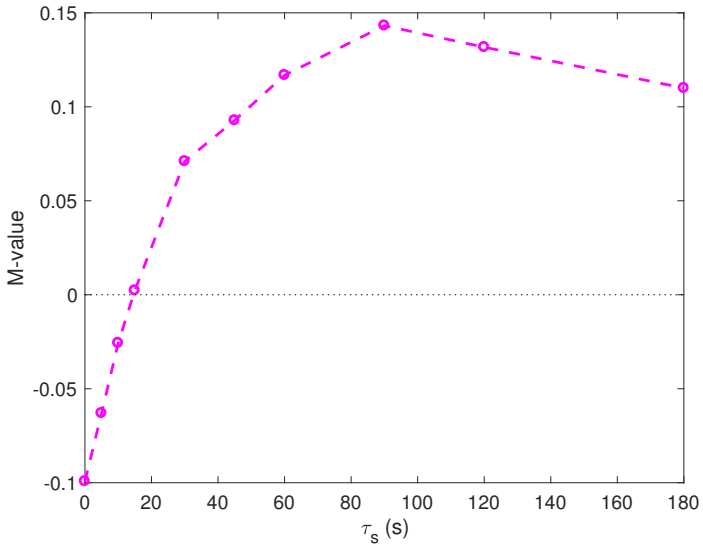

(a) $\Omega_0 = 3RPM$

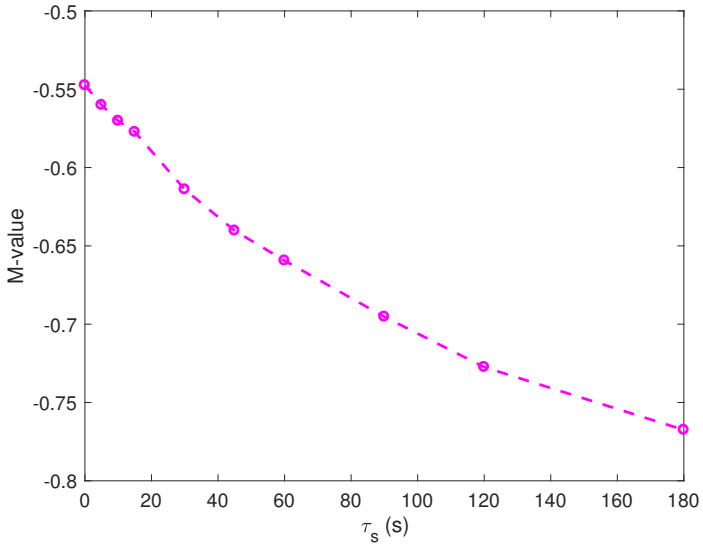

(b) $\Omega_0 = 10RPM$

Figure 8.13: The circles represent calculated M-values after 1.6 hours of rotation. The following rotation schedule was used for all simulations: $\tau_a = 60$ sec, $\tau_r = 15$ sec, $\tau_d = 60$ sec, while τ_s varied from 0 to 180 seconds.

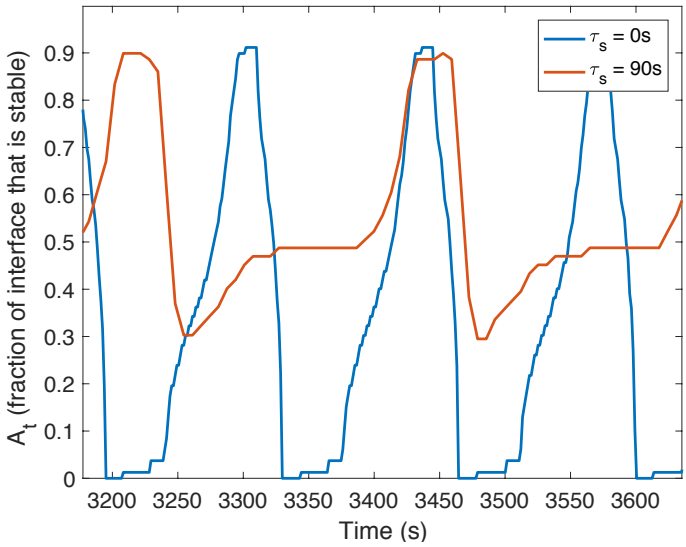

Figure 8.14: The fraction of the interface that is stabilized, A_t, for $\Omega_0 = 3$ RPM after 53 minutes of rotation. $\tau_s = 0$ sec is plotted in blue and $\tau_s = 90$ sec is plotted in red.

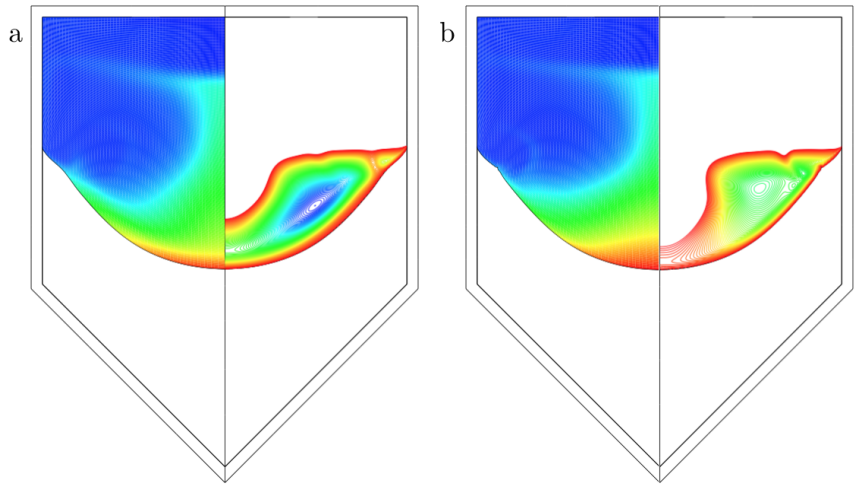

Figure 8.15: Tellurium concentration (left) and supercooled fluid (right) after 1.6 hours of ACRT under the following rotation schedule: $\Omega_0 = 3$ RPM, $\tau_a = 60$ sec, $\tau_r = 15$ sec, $\tau_d = 60$ sec, a) $\tau_s = 0$ sec, and b) $\tau_s = 90$ sec. $C_{min} = 54.75$ at% Te, $C_{max} = 55.58$ at% Te, ΔT_{min} = -2.40 K, $\Delta T_{max} = 0$ K.

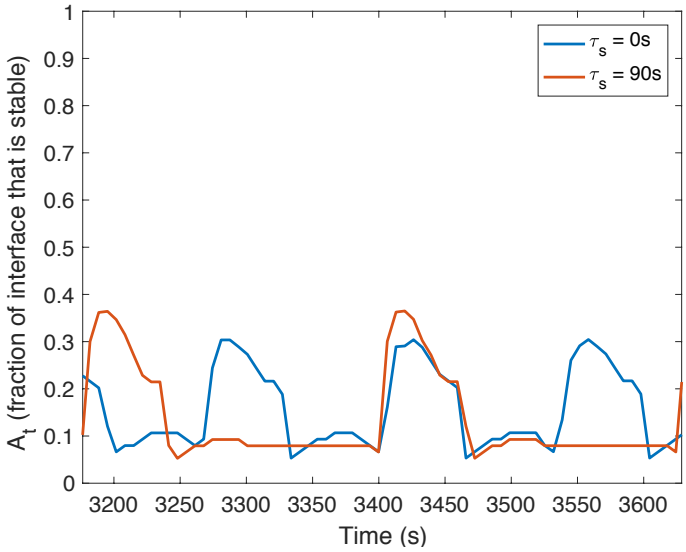

Figure 8.16: The fraction of the interface that is stabilized, A_t, for $\Omega_0 = 10$ RPM after 53 minutes of rotation. $\tau_s = 0$ sec is plotted in blue and $\tau_s = 90$ sec is plotted in red.

oscillation in interface velocity in the former case paired with the quick changes to the solute field result in worsened stability. This is also confirmed by contour plots of the tellurium concentration and supercooling after 1.6 hours of rotation. Figures 8.15(a) and (b) show the results for the case of $\tau_s = 0$ seconds and $\tau_s = 90$ seconds, respectively. The former results in more severe supercooled fluid with a minimum supercooling value of -2.40 K compared to -1.42 K in Figure 8.15(b).

However, this argument does not explain the behavior for $\Omega_0 = 10$ RPM shown in Figure 8.13b, which exhibit worse stability for larger τ_s values. This is best understood with a comparison of A_t values during a single cycle, shown in Figure 8.16 for $\tau_s = 0$ seconds in red and $\tau_s = 60$ seconds in blue. As the deceleration periods drive A_t down to nearly 5% stable, the strong flows perpetuate this level of stability during the stopped regime. As the length of τ_s increases, the total amount of time spent at such destabilizing conditions increases. These periods correspond to moments in the cycle where the interface velocity is at a maximum, shown in Figure 8.17. Although the $\tau_s = 0$ sec case has a higher average velocity 1.0 mm/hr compared to 0.89 mm/hr in the $\tau_s = 90$ sec case, and similar standard deviations around 0.50 mm/hr, worse

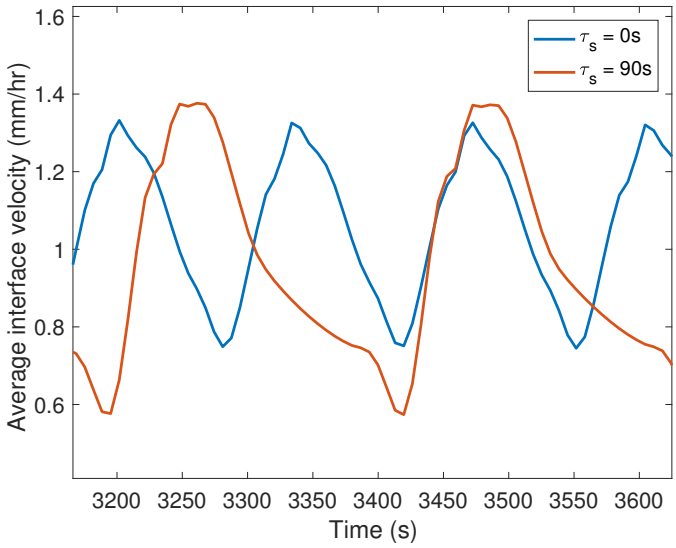

Figure 8.17: The average interface velocity after 53 minutes of rotation for $\Omega_0 = 10$ RPM. $\tau_s = 0$ sec, plotted in blue, has an average interface velocity of 1.0 mm/hr and $\tau_s = 90$ sec, plotted in red, has an average interface velocity of 0.89 mm/hr.

stability is observed for the $\tau_s = 90$ sec case. This is because more time is spent at its maximum velocity, resulting in more segregated tellurium and worse supercooling. This observation is confirmed visually with the contour plots presented in Figure 8.18. After 1.6 hours of rotation, both concentration fields are well-mixed. However, unlike the previous cases, the $\tau_s = 0$ seconds case shown in Figure 8.18a has an improved magnitude of supercooling of -2.50 K compared to -3.23 K for the $\tau_s = 90$ seconds case shown in Figure 8.18b. These results are strong indications that the system's response to changing τ_s is highly dependent on Ω_0, and how the interface velocity has improved or exacerbated supercooling conditions.

8.6 Conclusion

We have presented a series of simulations that shed light on ACRT as applied to the vertical gradient freeze growth of CZT. In an effort to optimize and compare various rotation schedules, a metric that relies on the classic Mullins and Sekerka stability criterion was designed. This metric — referred to as the M-value — incorporates both spatial

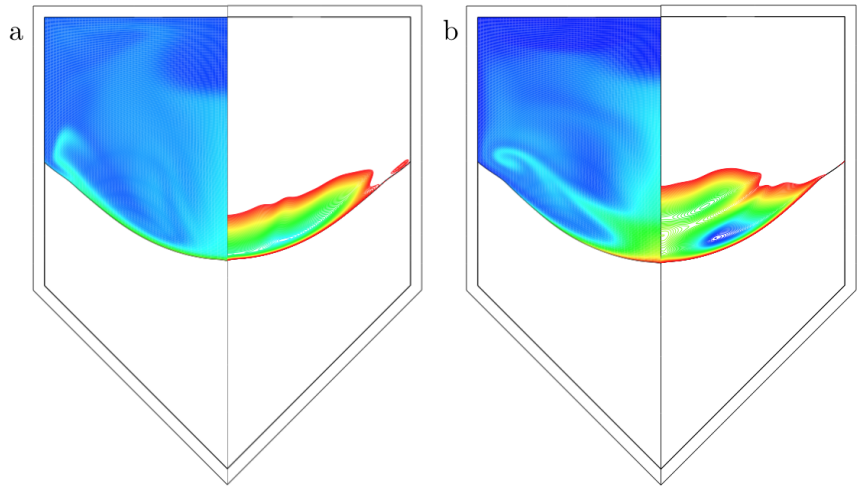

Figure 8.18: Tellurium concentration (left) and supercooled fluid (right) after 1.6 hours of ACRT under the following rotation schedule: Ω_0 = 10 RPM, τ_a = 60 sec, τ_r = 15 sec, τ_d = 60 sec, a) τ_s = 0 sec, and b) τ_s = 90 sec. C_{min} = 54.86 at% Te, C_{max} = 55.36 at% Te, ΔT_{min} = -3.23 K, ΔT_{max} = 0 K.

and temporal variations in the stability along the interface and allows for quantitative comparison of rotation schedules over many simulations.

This value was first used in a 2-k factorial design that analyzed the preliminary response of the system to changes in rotation schedule. Five parameters of the rotation schedule were tested: the maximum rotation rate, the period of acceleration, the period of constant rotation, the period of deceleration, and the period at rest. These efforts revealed that the maximum rotation rate has the most impact on the system, followed by the acceleration and rest periods.

We explored the influence of these three parameters further by varying each across a wide range of values and measuring a response in the M-value. For the current system, rotation rates of 3 RPM yielded the optimal stability. This rotation rate encouraged Ekman flows that are strong enough to induce a stabilizing effect during the acceleration period, but are weak enough such that the local interface velocity is not severely altered. This is in contrast to the system under a rotation rate of 10 RPM, where the Ekman flows are so strong that they induce interface velocities nearly double that of the 3 RPM case. This large adjustment in velocities results in significant changes to the local

composition field, which exacerbate an instability. While the exact values found here are specific to the system at hand, these results support the idea that a rotation rate should be selected that maximizes the Ekman flow while minimizing fluctuations in the interface velocity.

For both 3 RPM and 10 RPM cases, increasing the acceleration period had a positive effect on the overall stability. Despite having the same flow strength and interface velocities, simulations with longer acceleration periods resulted in improved stability and supercooling. Fast changes to the local solute field worsen the stability, and should be avoided.

Lastly, the influence of the rest period was found to be highly dependent on the rotation rate. For a maximum rotation rate of 3 RPM, longer rest periods were correlated with better stability. This is again due to the argument that gradual perturbations to the solute field result in improved supercooling. However, for a maximum rotation rate of 10 RPM, the coupling of the strong, Ekman flow that occurs during deceleration result in long periods of fast growth, which yield long periods of segregation and the formation of supercooled fluid. Thus, the length of the rest period could improve or worsen the overall stability, depending on the maximum rotation rate.

For this system, the most important issue to manage is the impact of differing rotation schedules on the local interface velocity. Schedules that reduce dramatic oscillations in the velocity yield better stability. With this insight in hand, we can consider other methods of interface velocity management to achieve even better stabilizing conditions. For example, changing the applied furnace gradient or the initial amount of excess tellurium may alter the local velocities for the better. These ideas will be touched upon in Chapters 9 and 10.

Although the exact values presented here are specific to the system at hand, the idea of managing the interface velocity to prevent the deleterious build up of supercooled fluid is applicable to all systems under ACRT. However, calculations with specific physical properties and geometries would need to be performed to provide a range of optimal operating parameters.

Chapter 9

An Investigation of Solidification Dynamics with Varying Thermal Gradients

9.1 Summary

In this chapter, we analyze the impact of two different applied temperature gradients, 10 K/cm and 30 K/cm, on the flow, temperature, tellurium distribution, and undercooling during growth with and without applied ACRT. Under growth without rotation, a higher axial thermal gradient results in stronger thermal-buoyancy driven flows, a faster interface growth velocity, greater tellurium segregation, and stronger undercooling. ACRT improves the stability of the growth interfaces for both systems; however, contrary to conventional wisdom, the case of the shallow thermal gradient is predicted to exhibit a more stable growth interface, which may result in fewer inclusions and higher quality material. Note that many of these results were first published in [138] and reproduced with permission from the SPIE Digital Library.

We represent the furnace temperature as a linear function applied as a Dirichlet condition that translates at 2 mm/hour, depicted schematically in Figure 9.1a. Although a completely linear profile is highly idealized, this choice is motivated by simplicity. Gradients of 10 K/cm and 30 K/cm are applied to the system, and an initial condition

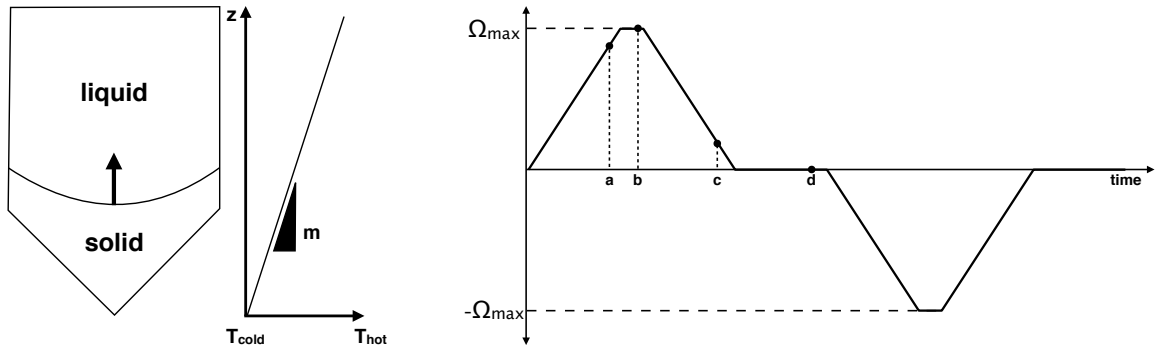

(a) (b)

Figure 9.1: (a) Schematic of VGF method where a translating furnace profile with a gradient of m is applied to directionally solidify CZT in a conical ampoule, (b) schematic of a sample rotation schedule with four regimes: a) acceleration, b) constant RPM, c) deceleration, and d) zero RPM.

is chosen as a state of growth where the crystal is roughly one third of the way grown.

9.2 Initial condition

The transient simulations are started from the steady states depicted in Figure 9.2, in which the growth velocity is taken to be zero and the composition field is assumed constant with a uniform concentration of 53.478 at% Te in the melt. Streamlines (left) and temperature isotherms (right) are shown in Figures 9.2 (a) and (b) for the 10 K/cm and 30 K/cm applied furnace gradients, respectively. Both plots are scaled with identical extrema, allowing for direct comparison of values.

Qualitatively, both streamlines (left) exhibit the same thermal-buoyancy-driven flow structure. The upper clockwise flow cell is driven by hotter fluid rising along the outer crucible wall. Near the concave interface, the radial thermal gradient is reversed, driving a counter-clockwise lower vortex. This is typical of the classic two-vortex structure found in many Bridgman-like problems. The 10 K/cm and 30 K/cm cases differ only in the strength of this flow, as identified by the different color scales found in each. This is expected, since the Rayleigh number — the dimensionless group that represents the strength of thermal buoyancy in the system — scales linearly with the temperature

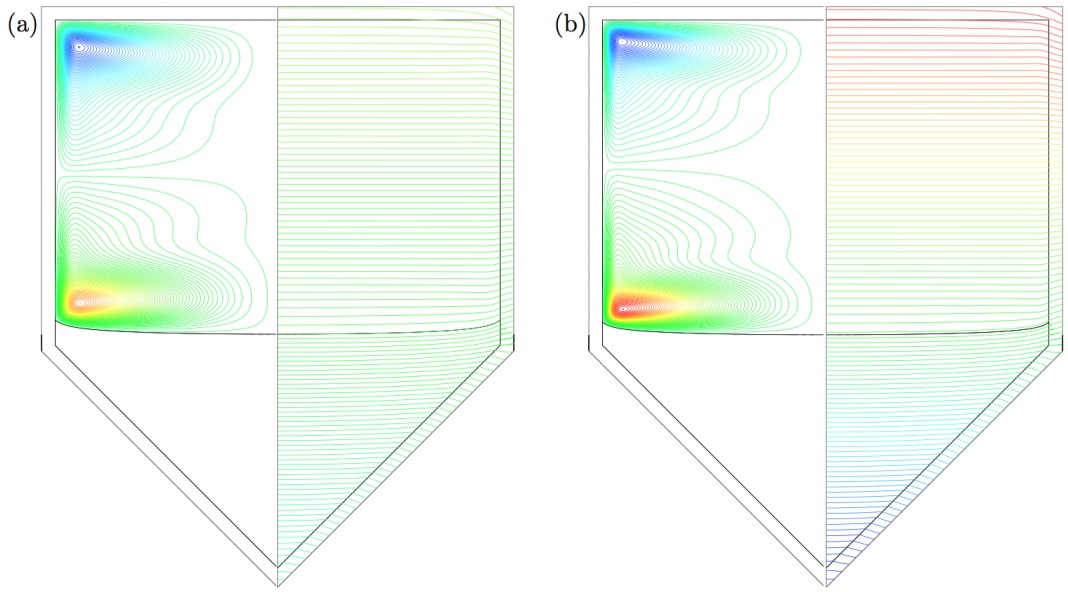

Figure 9.2: Contour plots of streamlines (left) and temperature isotherms (right) for the initial states for the (a) 10K/cm and (b) 30K/cm cases. $\psi_{min} = -0.008677 cm^3/s$, $\psi_{max} = 0.01244 cm^3/s$, $T_{min} = 1221K$, $T_{max} = 1434K$

gradient.

In both cases the isotherms (right) are spaced closer together in the solid due to a smaller thermal conductivity than the liquid. The interface is concave with respect to the solid, which is a consequence of the interactions of the thermal field, the mismatch of thermal conductivities, and latent heat effects. The shallow gradient of the 10 K/cm case is seen in the figure via the limited color range of the isotherms.

9.3 Transient growth under steady conditions

Before applying ACRT, it is important to understand the differing behaviors of the system at a constant growth rate with no crucible rotation. Recall that growth is driven by axially upward translation of the linear temperature profile representing the furnace. Streamlines (left) and temperature isotherms (right) after approximately 10 hours of growth are shown in Figures 9.3a and b for the 10 K/cm and 30 K/cm cases, respectively. The underlying flow structure has remained nearly unchanged from the

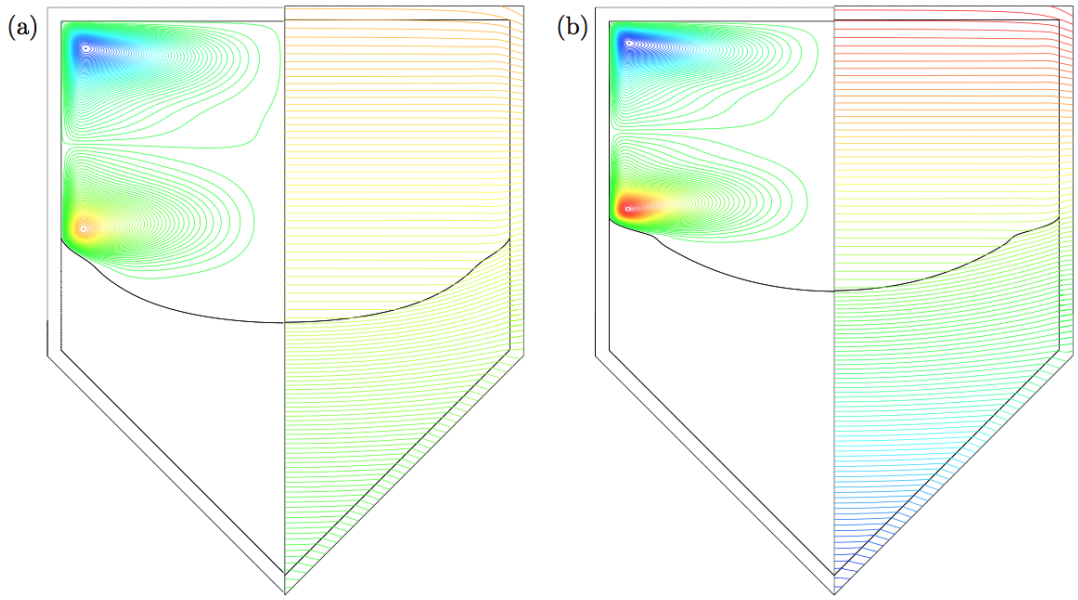

Figure 9.3: Contour plots of streamlines (left) and temperature isotherms (right) at approximately 10 hours into (non-ACRT) growth for the (a) 10K/cm and (b) 30K/cm cases. $\psi_{min} = -0.008439 cm^3/s$, $\psi_{max} = 0.009990 cm^3/s$, $T_{min} = 1165K$, $T_{max} = 1374K$

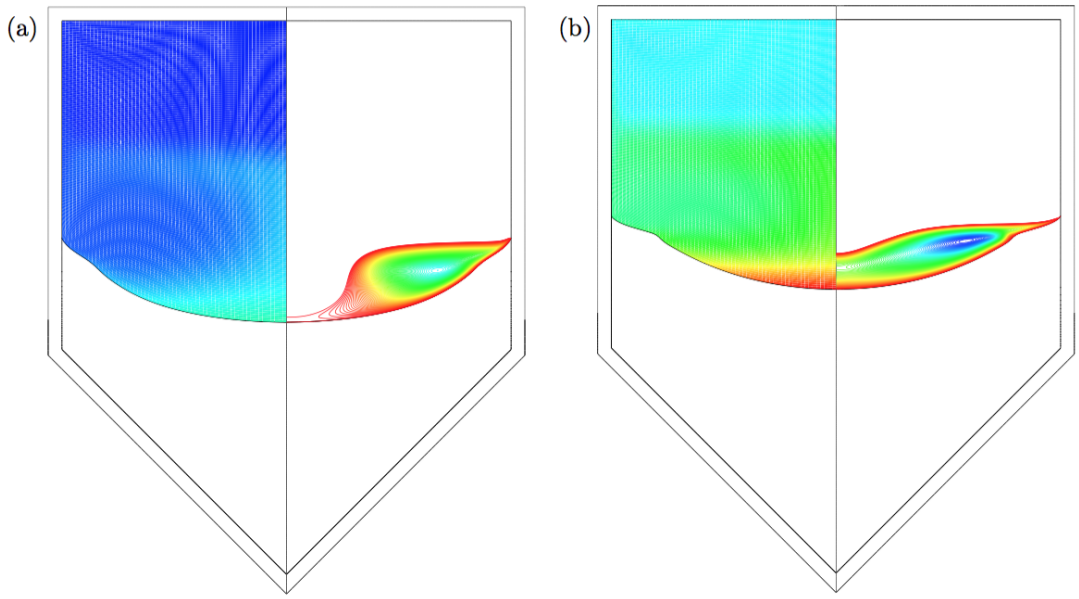

Figure 9.4: Contour plots of tellurium concentration (left) and supercooling isotherms (right) at approximately 10 hours into (non-ACRT) growth for the (a) 10K/cm and (b) 30K/cm cases. $C_{min} = 53.96at\%$, $C_{max} = 56.19at\%$, $\Delta T_{min} = -1.775K$, $\Delta T_{max} = 0K$

initial states. The flows in the 30 K/cm case are still stronger, as exhibited by the color scale.

There are a few interesting observations of the interface. First, the interface in the 30 K/cm case has grown farther than in the 10 K/cm case. The local interface velocity is not necessarily equal to the applied translation rate, and the lower gradient case lags behind the higher gradient case, likely due to the larger heat transfer through the melt caused by stronger convection in the latter case. In fact, the local average growth rate at the centerline for the 30 K/cm is over twice as fast as that of the 10 K/cm case (0.872 versus 0.371 mm/hr, respectively). This is discussed further in section 9.3.1.

The tellurium concentration (left) and thermal supercooling (right) after 10 hours of growth are shown in Figures 9.4a and b for the 10 K/cm and 30 K/cm cases, respectively. Although somewhat difficult to identify owing to the different range of colors in the visualizations, both concentration fields exhibit similar structures which are consequences of the flow patterns. As tellurium is rejected by the growing solid, it accumulates in front of the interface. The counter-clockwise flow sweeps this concentrated material towards the centerline and upwards until it reaches the upper vortex. The shear layer that separates the two vortices prevents the penetration of flow between the two vortices; species transfer across this shear layer must occur via diffusion through the melt. The upper vortex in both cases mixes the melt, producing a region of constant concentration. This pattern is observed in both cases, with differing colors in the concentration plots clearly separating the two regions.

This has an impact on the morphology of the interface. The solidification interface is noticeably deflected in both systems, compared to the initial states shown in Figure 9.2. This is driven by latent heat effects combined with changes in composition, linking the melt-solid interface with the phase diagram. As tellurium is rejected during growth, it accumulates along the melt-solid interface, particularly near the centerline. This increase in concentration depresses the compositional-dependent melting point, as determined by the liquidus data, which locally retards growth of the interface. The resulting local depression of the interface at the centerline is so great that the lower flow cell can no longer effectively sweep tellurium away from the interface, compounding the effect. Another effect of this flow-composition coupling is the deflected, shoulder-shape morphology of the interface near the crucible side wall.

Thermal supercooling occurs in the melt in front of the interface for both cases as a result of tellurium enrichment via segregation. As explained above, the presence of melt supercooling is a precursor to instability of the interface [126] and the possible formation of tellurium inclusions. The 30 K/cm case exhibits a larger magnitude and greater spatial extent of supercooling than the 10 K/cm case (-1.775 versus -1.336 K, respectively). This is of great interest, because simple arguments would presume that the higher axial gradient would result in a more stable configuration. Instead, with a faster growth rate and the aforementioned accumulation of Te in the 30 K/cm system, supercooling in the melt in this transient system is enhanced. Thus, the destabilizing effects of the solutal field outweigh the stabilizing effects of the larger thermal gradient.

9.3.1 Longer-term behavior

In order to see how the differing thermal gradients impact the system over a longer time period, values for the interface growth velocity at the centerline and minimum supercooling are shown in Figure 9.5.

The interface velocities at the centerline for both the 10 K/cm and 30 K/cm cases, shown in Figure 9.5a, exhibit a similar pattern but are offset by approximately 0.5mm/hr. Both interface velocities begin at zero, as the interfaces in the initial conditions are stationary. As the applied linear temperature field is translated at a constant rate of 2 mm/hr, both interfaces start moving. The velocity of the 30 K/cm case increases faster, due to higher levels of convective heat transfer through the melt, as asserted above.

The growth velocities for both cases reach a local maximum after approximately 6 hours and then decrease and plateau. This initial transient corresponds to the transition from a planar-like interface to one with deformation, as shown above in Figure 9.4. With the onset of the deformation, the centerline velocity decreases, and the interface shape remains relatively unchanged. After 23 hours, however, the interface velocity dramatically increases again. At this point, the melt volume has shrunk significantly enough so that the lower vortex has disappeared, and the entire melt is dominated by a single clockwise vortex. This vortex is able to penetrate into the quiescent region near the interface, adjusting the local compositional field so that the interface has a chance to grow faster and "catch up". This happens sooner in the 30 K/cm system as it reaches a small volume of melt sooner. The 30 K/cm system interface velocity

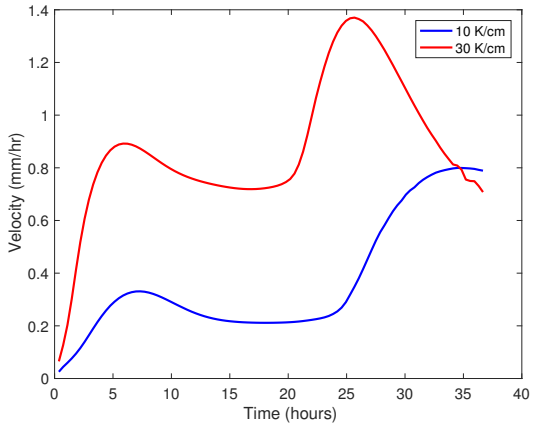

(a) Interface velocity at centerline.

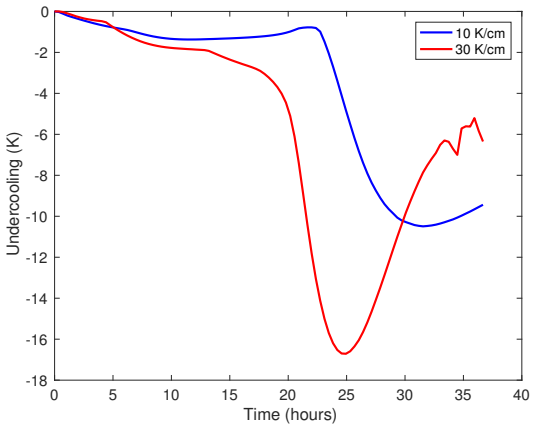

(b) Minimum supercooling.

Figure 9.5: Trends of interface velocity and supercooling during steady (non-ACRT) growth.

peaks and then falls again because the volume of melt has become so small and the tellurium concentration has increased such that it dramatically retards the local growth rate. The 10 K/cm would do the same if given more time. Importantly, the nonlinear interactions among flow, composition, and the phase diagram never allow the centerline growth velocity to reach the steady furnace profile translation rate of 2 mm/hr.

The overall faster growth rate of the 30 K/cm case has a detrimental impact, as evidenced by the larger magnitude supercooling values shown in the contour plots in Figure 9.4. To see how this trend develops over the entire course of the simulation, the minimum value of the supercooling within the entire melt is plotted versus time for both the 10 K/cm and 30 K/cm cases in Figure 9.5b. Both cases begin with zero supercooling; however, as growth begins, both curves begin to drop. As the growth rate increases for the 30 K/cm case, resulting in a larger rejection of tellurium into the melt, the supercooling quickly grows to an absolute minimum of around -17K. This minimum is reached before the 10 K/cm case following discussion above. The 30K/cm case rises again due to the sharp change melt volume. As the volume decreases, the concavity of the interface shape changes, and the classic Bridgman two-vortex structure merges into one. This ameliorates the supercooling and causes minor fluctuations in the supercooling.

9.4 Transient growth under ACRT

Transient growth simulations with applied rotation are performed using the following ACRT schedule: A maximum rotation rate of 10RPM, 60 seconds to accelerate to the maximum rotation rate, 15 second held at the maximum rotation rate, 60 seconds to decelerate back down to zero RPM, and 60 seconds held at zero RPM. This is repeated in the reverse direction for a total of one cycle. The rotation schedule is depicted schematically in Figure 9.1b.

This rotation schedule is applied to both the 10 K/cm and 30 K/cm systems after approximately 10 hours of growth, after substantial supercooling has occurred in both systems (initial condition for ACRT calculations is shown in Figures 9.3 and 9.4). Contour plots from the first half of the first cycle are shown in the Figures 9.6-9.11, with (a), (b), (c), and (d) plots corresponding to 55 seconds into rotation (the acceleration

regime), 70 seconds (the constant regime), 129 seconds (the deceleration regime), and 185 seconds (the zero rotation regime), respectively.

Streamlines for the 10 K/cm and 30 K/cm cases are shown in Figures 9.6 and 9.7, respectively. Both sets of figures have identical extrema and can be directly compared. As the crucible rotation accelerates, Ekman flows are driven by centrifugal forces outward along the horizontal surfaces, namely the upper crucible wall and the solid-liquid interface (for a further discussion on relevant rotational fluid dynamics, refer back to Chapter 5). These flows are strong enough to force fluid at the top and bottom of the melt outwards, towards the side wall. Continuity converts these outward surface flows into vortices, which are visible in Figures (a) and (b), with a lower vortex moving in the clockwise direction and the upper vortex moving in the counter-clockwise direction. These vortices move in the opposite direction to the underlying, thermal-buoyancy driven flows and, in the 10 K/cm case, are strong enough to override them.

However, the underlying buoyant vortices are still visible near the center and along the side wall for the 30 K/cm case. The Ekman vortices in this case are forced to be shorter and closer to the upper and lower surfaces. In fact, a close examination of the streamlines in the 30 K/cm case reveals that the Ekman flow is forced to turn before reaching the outer wall because of the much stronger underlying flow, as discussed earlier.

As the system rotation decelerates to zero in Figures (c), the Ekman flows are reversed, creating a lower vortex moving in the counter-clockwise direction and an upper vortex in the clockwise direction. Since these align with the underlying flow structure, the underlying buoyant vortices are strengthened during this period, as evidenced by the red and blue maxima in the vortex centers. As the system comes to rest and is held at zero RPM in Figures (d), the Ekman flows subside, leaving a flow structure similar to that arising solely from buoyancy.

Notably absent from the flows exhibited by this system are the Taylor-Görtler vortices that typically form during spin down of the ACRT cycle [58]. This is likely due to the relatively low maximum rotation rate and short cycle times for the ACRT schedule employed here.

The effects of the flows of the first ACRT cycle on the concentration profiles are shown in Figures 9.8 and 9.9 for the 10 K/cm and 30 K/cm cases, respectively. For

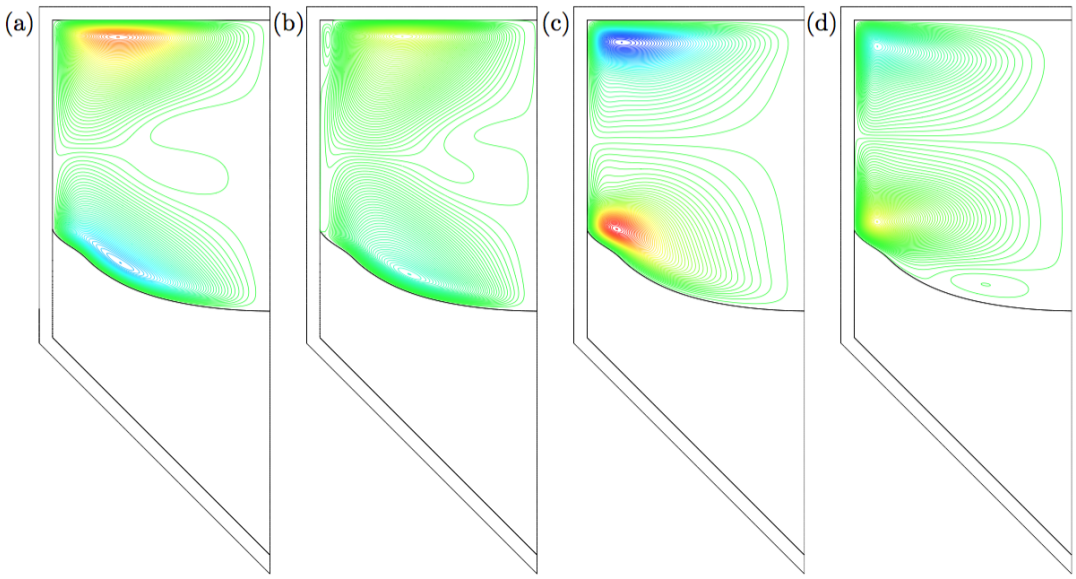

Figure 9.6: Streamlines for 10 K/cm case during the first applied ACRT cycle with the following timepoints: (a) acceleration, (b) constant rotation, (c) deceleration, and (d) zero rotation. $\psi_{min} = -0.01698 cm^3/s$, $\psi_{max} = 0.01831 cm^3/s$.

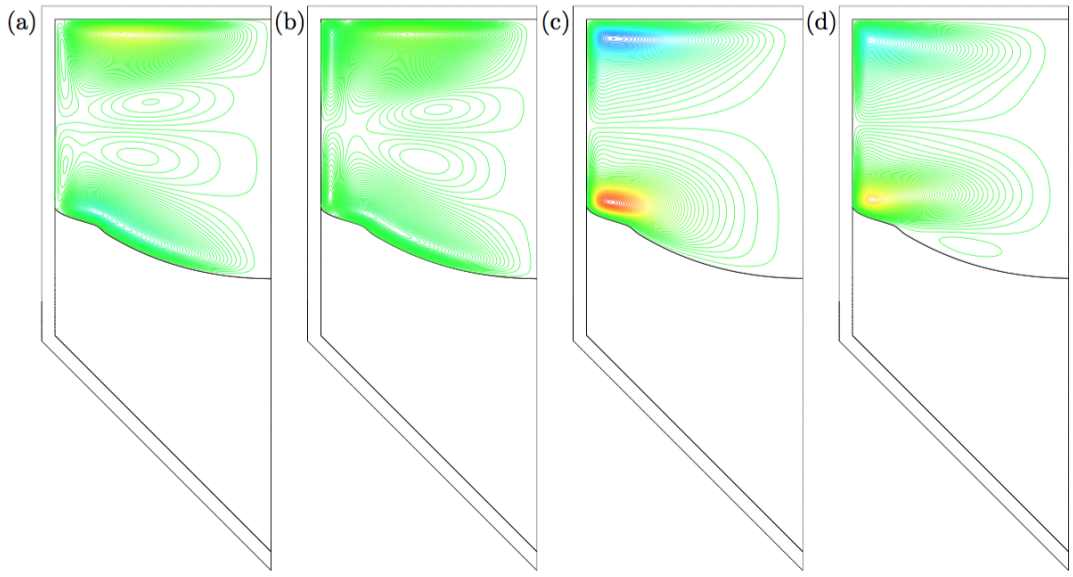

Figure 9.7: Streamlines for 30 K/cm case during the first applied ACRT cycle with the following timepoints: (a) acceleration, (b) constant rotation, (c) deceleration, and (d) zero rotation. $\psi_{min} = -0.01698 cm^3/s$, $\psi_{max} = 0.01831 cm^3/s$.

these visualizations, it is more instructive to scale each case with different extrema, given the significant disparities in average concentrations for both initial cases shown in Figure 9.4. Therefore, the absolute concentrations in each are different, as noted in the captions.

During rotational acceleration, shown in Figures (a), the Ekman flow sweeps highly concentrated liquid from the center of the interface towards the side wall, which is especially true for the 10 K/cm case. However, given the strong underlying vortex in the 30 K/cm case counteracting the Ekman flow, the Ekman flow is not strong enough to move the most highly concentrated liquid to the side wall.

During constant rotation, shown in Figures (b), the liquid that is near the side wall in the 10 K/cm case forms an upward plume. In contrast, the 30 K/cm case is relatively unchanged, since the strong thermal buoyancy forces are continually counteracting the rotational flow.

As the rotation is decelerated to zero, shown in Figures (c), the Ekman flow is reversed, and, in both cases, more concentrated fluid is brought towards the center of the interface. While being held at zero rotation, shown in Figures (d), both systems are dominated again by the underlying thermal-buoyancy driven flow, as more highly concentrated liquid flows in the counter-clockwise direction near the interface. During this entire period, the upper shear layer is constantly present and in neither cases is the Ekman flow observed to penetrate the upper vortex.

Lastly, the supercooling in the melt is shown for the 10 K/cm and 30 K/cm cases during the first ACRT cycle in Figures 9.10 and 9.11, respectively. Absolute values are chosen for the color plots, so a direct comparison is possible. During acceleration and constant rotation, shown in Figures (a) and (b), fluid is swept outwards along the interface. The disruption of flows along the interface momentarily melting back the solid, thus stabilizing the interface as discussed in the previous chapter. However, the highest values of supercooling, as evidenced by the green and blue contours, occurs during these periods of the cycle. This is likely a consequence of the movement of concentrated liquid towards the side wall.

During deceleration, shown in Figures (c), the Ekman flow drives fluid back towards the centerline, not only driving the growth of new supercooled fluid, but also encouraging this supercooled liquid to be brought back to the center. In the 10 K/cm case, this flow

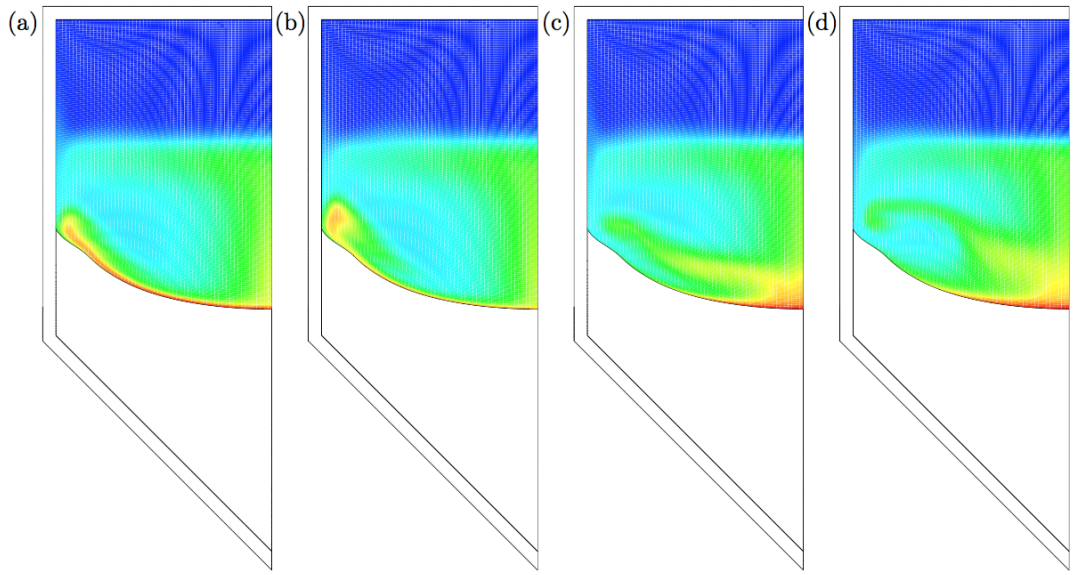

Figure 9.8: Tellurium concentration for 10 K/cm case during the first applied ACRT cycle with the following timepoints: (a) acceleration, (b) constant rotation, (c) deceleration, and (d) zero rotation. $C_{min} = 53.97at\%$, $C_{max} = 54.64at\%$.

reversal creates a pocket of supercooled liquid above the interface, which is eliminated shortly thereafter by the Ekman flow. As the system is held at zero rotation, shown in Figures (d), the supercooling takes on its original structure and decreases in magnitude. Overall, the volume of supercooled melt decreases with applied rotation, despite the maximum amount of the supercooling increasing in magnitude. The 30 K/cm case again shows a higher magnitude of supercooling due to the effects described above. The supercooling of the 30 K/cm case, however, always remains in a smaller region, suggesting the overall volume of supercooling is less than that in the 10 K/cm case.

9.4.1 Longer-term behavior

ACRT is continued for another 30 cycles in order to observe the longer-term effects on the system. Concentration and supercooling are shown in Figures 9.12a and b for the 10 K/cm and 30 K/cm cases, respectively.

Repeated ACRT cycles have resulted in significant mixing of the melt adjacent to the liquid-solid interface, which has reduced the Te concentration near the interface thus

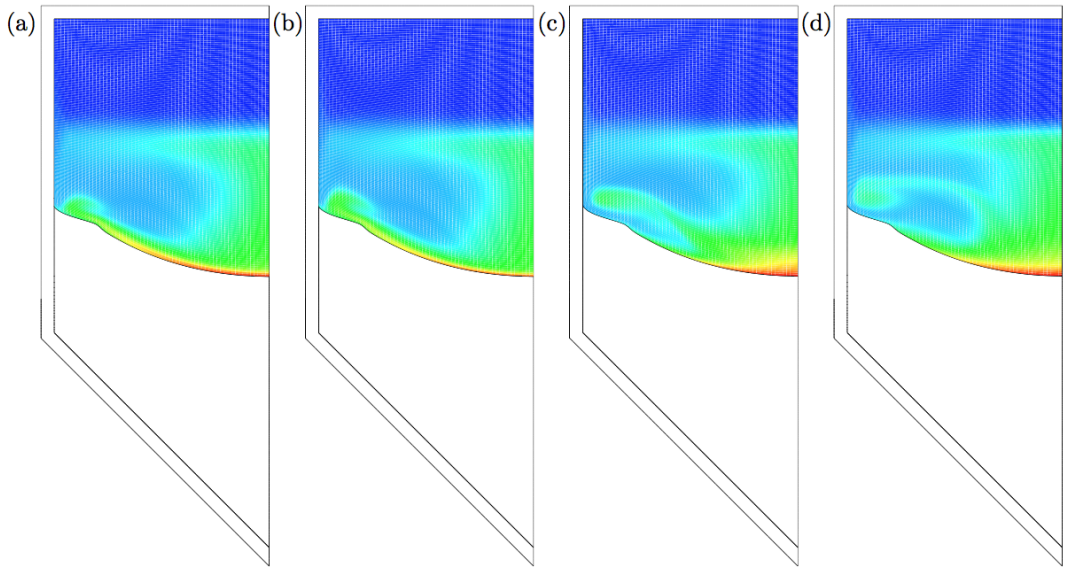

Figure 9.9: Tellurium concentration for 30 K/cm case during the first applied ACRT cycle with the following timepoints: (a) acceleration, (b) constant rotation, (c) deceleration, and (d) zero rotation. $C_{min} = 54.50at\%$, $C_{max} = 56.14at\%$.

significantly reducing its deflection that had arisen in prior cases due to compositional effects. The Te concentration near the interface in the 30 K/cm case is still significantly higher than in the 10 K/cm case, which produces a higher magnitude of supercooling (-1.931 versus -2.272K, respectively).

The volume of supercooling in both cases has shrunk from their initial conditions, which demonstrates that the application of crucible rotation via ACRT is effective for stabilizing growth, compared to the cases with no rotation. In contrast to convention wisdom surrounding ACRT, however, neither case exhibits full homogenization of the melt nor complete elimination of supercooling, even after 30 cycles. Rather, both retain the shear layer between the upper and lower vortices and a significant amount of supercooling.

Although the scope of this test is limited in the application of only 30 cycles, we observe that the 10 K/cm system continues to have less severity of supercooling. Intriguingly and against common wisdom, the system with the lower axial thermal gradient is likely to be more stable and less prone to inclusion formation. However, this could

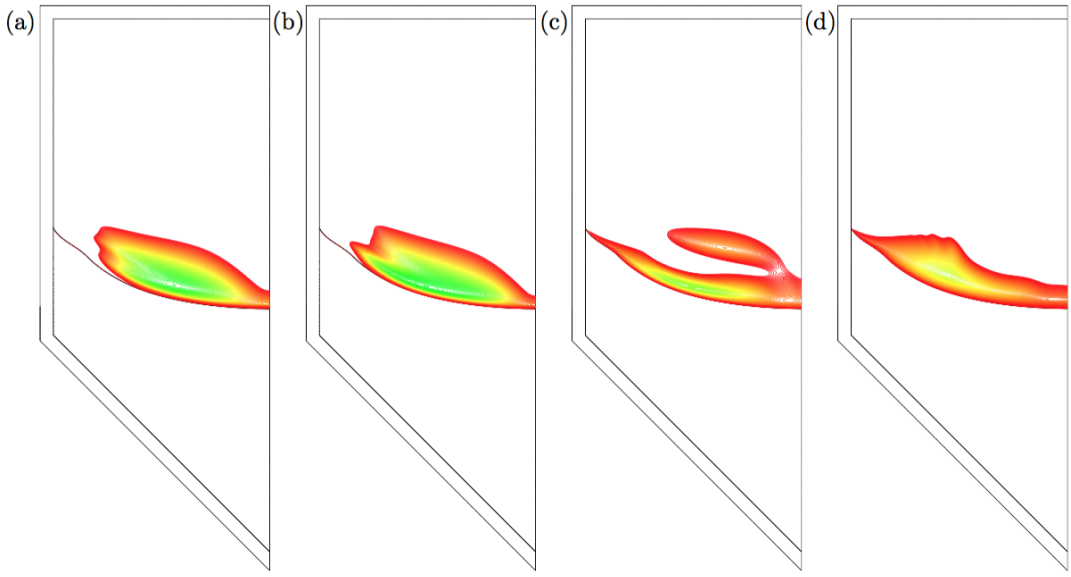

Figure 9.10: Undercooling for 10 K/cm case during the first applied ACRT cycle with the following timepoints: (a) acceleration, (b) constant rotation, (c) deceleration, and (d) zero rotation. $\Delta T_{min} = -7.0K$, $\Delta T_{max} = 0K$.

simply be an artifact of the lower effective growth rate that occurs in the 10K/cm system. As discussed, a slower growth rate will accumulate tellurium and subsequently supercooled regions slower.

9.5 Conclusion

In this chapter we have presented the numerical analysis of ACRT applied to the gradient freeze growth of CZT under two differing furnace profiles. A linear profile with a gradient of 10 K/cm or 30 K/cm was applied to the system and translated at a constant rate of 2mm/hr to achieve directional solidification. While both cases showed qualitatively similar thermal-buoyancy driven flow structures, a significantly stronger flow occurred in the 30 K/cm case. A transient simulation of growth without rotation was presented and analyzed to reveal faster interface growth rates for the 30 K/cm case, along with subsequently higher tellurium concentration gradients. Undercooling was present for both cases, but was higher in magnitude in the 30 K/cm case. Under application of

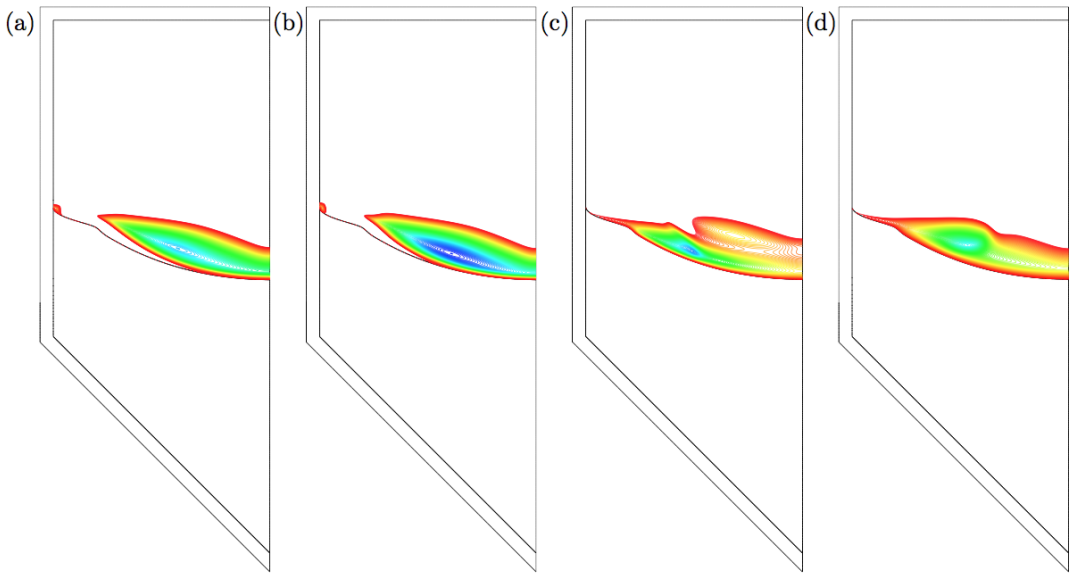

Figure 9.11: Undercooling for 30 K/cm case during the first applied ACRT cycle with the following timepoints: (a) acceleration, (b) constant rotation, (c) deceleration, and (d) zero rotation. $\Delta T_{min} = -7.0K$, $\Delta T_{max} = 0K$.

an identical ACRT schedule, the 10 K/cm case allowed for fully developed Ekman flow while the 30 K/cm case's strong underlying flow structure counteracted the Ekman flow. This resulted in worse mixing of the concentration field in the 30 K/cm case and subsequently higher supercooling. Neither case exhibited full homogenization of the melt after 30 cycles; rather, both retained the shear layer between two vortices.

The two largest impacts the differing gradients made were on the local interface velocity and the flow structure. The higher gradient promoted a faster response of the system to the translating temperature field and a much higher growth velocity. The higher velocity, in turn, resulted in higher rejection of Te at the growth interface, which increased the severity of the supercooling. This could of course be ameliorated by simply lowering the applied furnace translation rate, which has been conclusively shown to always produce higher quality material.

The impact of the strong furnace gradient extends further; under the stronger gradient, the Ekman flows were not able to be fully developed, which prevented the overall effectiveness of the tested ACRT schedule. For the conditions examined here, the lower

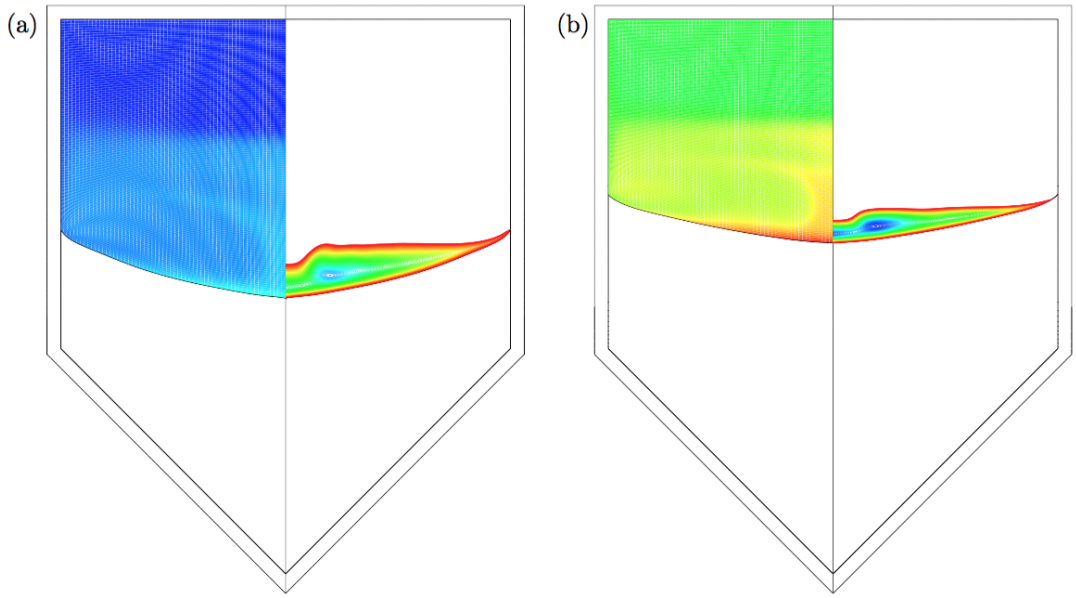

Figure 9.12: Contour plots of tellurium concentration (left) and supercooling isotherms (right) after 30 ACRT cycles for (a) 10K/cm and (b) 30K/cm cases. $C_{min} = 54.30at\%$, $C_{max} = 56.41at\%$, $\Delta T_{min} = -2.272K$, $\Delta T_{max} = 0K$

gradient system is less likely to be affected by supercooling and more likely to produce higher quality material with fewer inclusions.

We have thus far presented a significant amount of material elucidating the effects of rotation, local tellurium concentration, and furnace gradients on the VGF-ACRT system. In the next chapter, we discuss the influence of initial tellurium concentrations on the interface velocities. Additionally, we present two experimental results that provide evidence of the model's accurate representation of the physics. Although exact quantitative agreement is not uniformly found, the qualitative effects of segregation under ACRT with tellurium are reproducible.

Chapter 10

Model Validation

Model verification and validation are critical to a model's effectiveness and utility. Model verification, i.e., tests to ensure the code functions as desired, has been performed with various cases and will not be discussed here. Model validation, i.e., tests to ensure the model is representing the real system, requires comparison of model results to experimental results. All experiments were performed by collaborators at Washington State University, namely Jedidiah McCoy and Santosh Swain under the advisement of Professor Kelvin Lynn. Their results [139–141] are included with their permission.

The model at hand is loosely based on the work done by Zhang et al [4], who also worked with the same collaborators on a similar system. Most of the material properties are identical, with slight differences in geometry and furnace profiles to more accurately match the current WSU system. A validation experiment was performed and published in 2011 in which the zinc distribution in the grown crystal was compared to the model predictions. The results, reproduced in Figure 10.1, show very good qualitative and quantitative agreement between the experiment and the model. This close agreement indicates that Zhang's model — and subsequently ours — can be confidently used to predict future behavior.

That being said, two validation experiments were designed to test the current model's functionality, particularly with the incorporation of crucible rotation into the model. The first, described in section 10.1 is a growth run that repeatedly turned rotation on and off for long periods of time in order to assess the changes ACRT made to an identical system (i.e. this removed variability between separate experiments). The

second, described in section 10.2 is a comparison of rotation schedules to assess the utility of the metric developed in section 8.

10.1 Patterned rotation schedule experiment

With the limited physical resources and lengthy time to complete a growth experiment, a validation experiment was designed in order to accomplish two goals. The first and original aim of the experiment was to compare the impact of rotation to steady growth with all other parameters being held constant. Rotation would be turned on and off over long periods of time to grow discrete regions of material. Cubic centimeter-sized pieces could be cut out of each region and tested for its mobility-lifetime product, which a measure of the detector performance. This was important to test because significant variability exists between experimental runs, even while holding all conditions the same. This is partially due to the stochastic nature of the nucleation event that makes each run uniquely different. The second aim of the experiment was to compare the zinc distribution in the grown crystal to the model results for validation purposes.

The experiment went as follows: after nucleation, one quarter of the boule would be grown until the interface passed the cone region. At that point, 5 hours of ACRT would be applied, followed by 5 hours of steady (non-ACRT) growth, with this repeating a total of 4 times. For an applied translation rate of 2 mm/hr, 5 hours of growth should yield 10 mm bands. The following rotation schedule was selected for the periods of growth with ACRT: 60 seconds of acceleration, 120 seconds of constant rotation, 30 seconds of deceleration, and 0 seconds of rest. A maximum rotation rate of 10 RPM was selected.

10.1.1 Experimental results

A photoluminescence (PL) map indicating the presence of zinc is shown in Figure 10.2 for the experiment described above. During the experiment, nucleation must have occurred later than anticipated, and thus rotation was applied before the interface passed through the conical region. Regardless, clear bands of high and low zinc concentration are apparent in the grown crystal. This indicates that the alternating periods of rotation and steady growth had differing impacts on the zinc distribution. Seven bands are

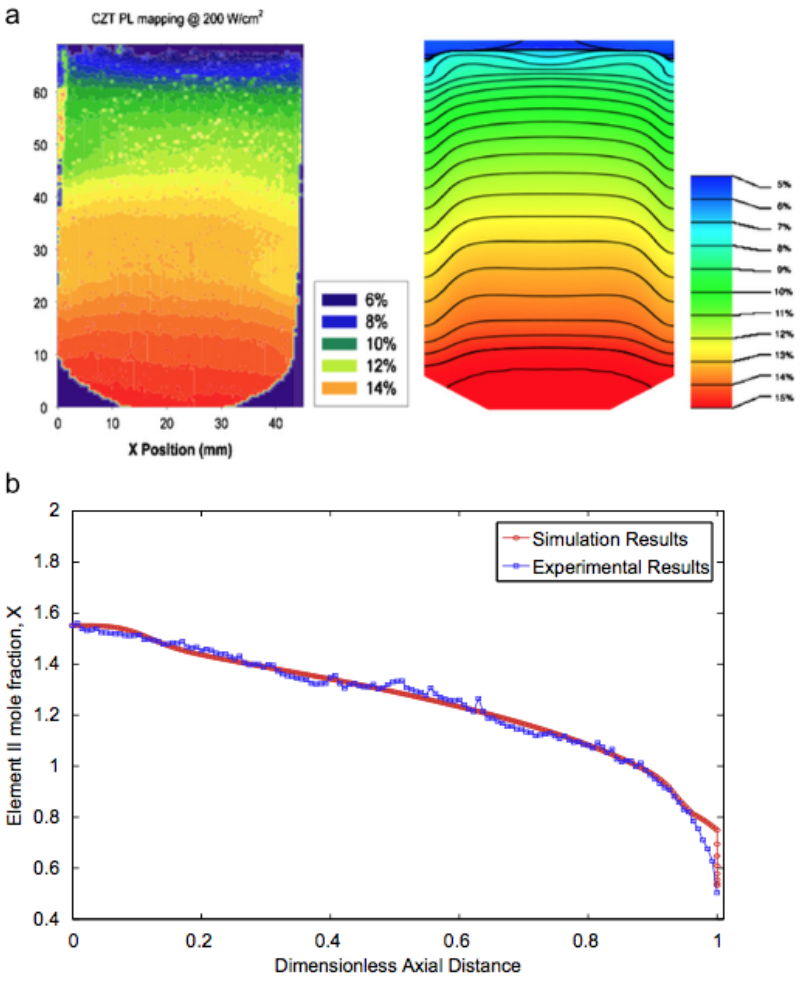

Figure 10.1: (a) A comparison of the photoluminescence map from the growth experiment to the simulation, where red and blue correspond to higher and lower zinc compositions in the melt. (b) Good agreement is observed in the numerical values and trend of the axial centerline zinc distribution. Reproduced from [4].

observed instead of the eight intended. The nucleation event likely occurred during or just after the first period, which explains the missing band. The bands are an average of 2.5 mm wide, which is four times smaller than the anticipated 10 mm. This indicates that growth was occurring approximately four times slower than the applied rate, thus at an average interface velocity of 0.5 mm/hr instead of 2 mm/hr. Unfortunately, these bands were too small to cut out cubic centimeter sized pieces from for further testing. However, the unanticipated outcome of the experiment was the ability to estimate the actual interface growth rate. The discrepancy between the applied translation rate and the actual interface velocity is hypothesized to be the consequence of tellurium suppressing the actual interface velocity. This is expanded upon with a discussion of the computational results in section 10.1.2.

Interpretation of the color distribution is straightforward. Under steady conditions, the segregation of zinc results in a depletion layer in front of the growing interface, which gets solidified as low-concentration regions in the solid. During periods of ACRT, the enhanced transport of zinc to the interface as a consequence of strong rotational flows increases the zinc composition near the interface, which solidify into regions of higher composition in the solid. Thus, the red bands correspond to regions of ACRT while green bands and the large region of green in the bulk correspond to regions of steady growth.

10.1.2 Computational results

Interface velocity

Due to the unexpected results of the experiment, two simulations were designed to explore the observed phenomena. First to be addressed is the discrepancy between the applied translation rate and the actual interface velocity. Although these values are not expected to be identical due to lagging thermal gradients, a discrepancy of four times is so large it must have an alternate explanation.

A steady (i.e. non-ACRT) simulation was performed for the following cases in order to determine the influence of tellurium on the interface velocity: no excess tellurium (i.e. a total fraction of 50% Te, the congruent composition, selected as an initial condition), 3.24% excess tellurium (i.e. a total fraction of 51.62% selected as an initial condition),

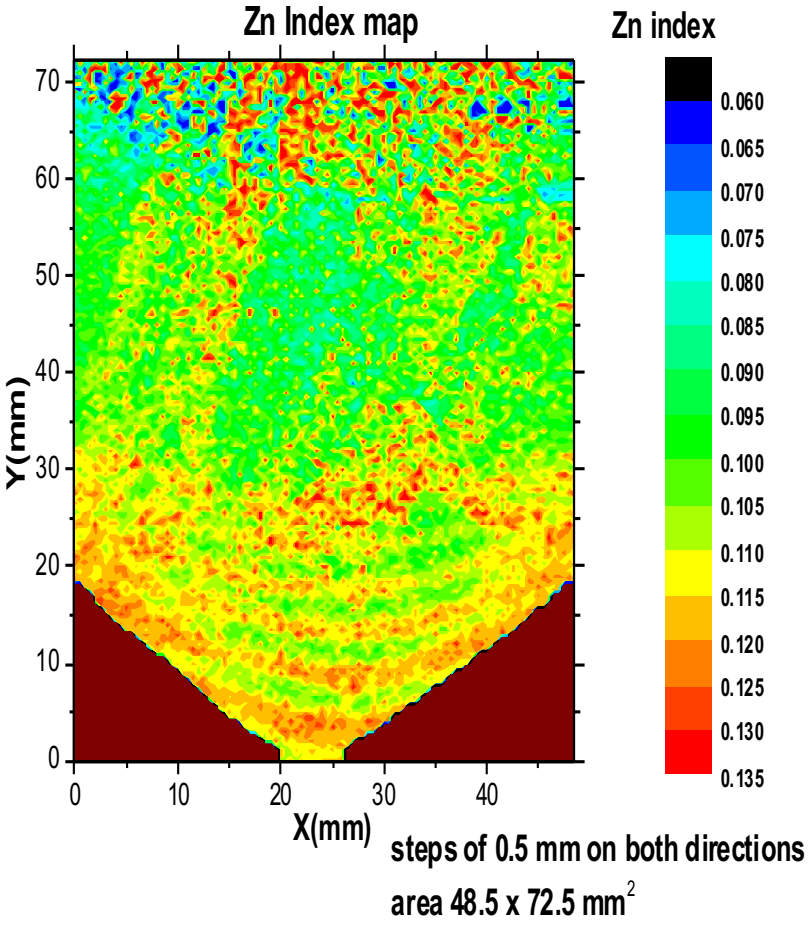

Figure 10.2: Photoluminescence map indicating presence of zinc in the grown boule. Four repeated cycles of 5 hours of ACRT followed by 5 hours of non-ACRT Red and blue correspond to high and low values of zinc in the crystal.

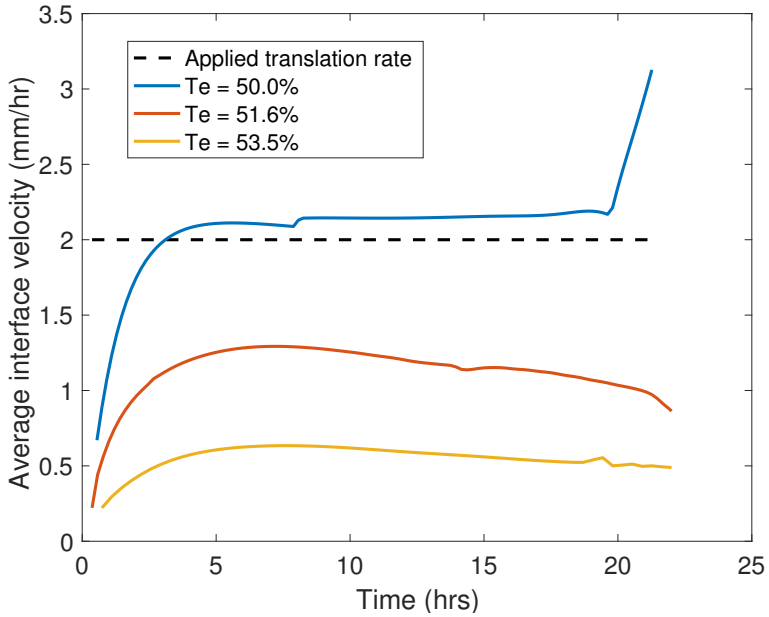

Figure 10.3: Average interface velocity for a growth system with varying levels of tellurium and an applied furnace translation rate of 2mm/hr.

and 7% excess tellurium (i.e. a total fraction of 53.5% Te selected as an initial condition). Their centerline velocities over 22 hours of growth are plotted in Figure 10.3.

Without any excess tellurium, the solidification temperature remains at the congruent temperature, and the melting point is not depressed due to compositional effects. Subsequently, the interface moves at an average velocity of 2.08 mm/hr, which is within 5% of the applied translation rate of 2 mm/hr. The dynamics of the interface velocity are shown with the blue curve in Figure 10.3. The interface velocity begins close to zero due to the initial condition of zero growth, but quickly speeds up to reach the applied translation rate of 2 mm/hr. This remains fairly steady throughout growth until the interface spikes to 3 mm/hr after 22 hours of growth. This occurs because the interface has approached the top of the ampoule, as apparent from the contour plot in 10.4, and the melt region has diminished such that the two-vortex flow structure has merged into one. This rearrangement of the flow convects warm fluid away from the interface such that the centerline grows faster.

An identical computation was performed with the addition of 51.62% tellurium

added to the melt as an initial condition. The centerline interface velocity is plotted in red in Figure 10.3. Again, an initial transient response occurs for the same reasons as the control. However over the course of the first 7 hours, the velocity slowly rises to "catch up" to the applied pull rate, however it plateaus at a maximum of approximately 1 mm/hr. This is still well below the applied translation rate of 2 mm/hr. During those first few hours of growth, tellurium is being segregated at a rate proportional to the excess tellurium in the melt. This accumulates tellurium in front of the growing interface, which, in turn, lowers the solidification temperature as determined by the liquidus line. The reduction of the solidification temperature retards the growth such that the interface can match the thermal field. This segregation effect paired with the competing growth effects create a fairly steady interface velocity value that is held constant for the remainder of the simulation. The reduction of the interface velocity also means that after 20 hours, the interface has not reached the top of the ampoule, as apparent from the interface location in Figure 10.4. Moreover, a significant amount of supercooled liquid has accumulated in the center as a consequence of tellurium accumulation. Since the interface has not yet reached the top of the ampoule, the spike seen in the previous case is not observed here. An average velocity of 0.877 mm/hr is calculated over 22 hours.

Lastly, an identical computation was performed with 53.5% tellurium added to the melt as an initial condition. This value was chosen because it most reflects the experimental conditions used. The centerline velocity for this case is plotted in yellow in Figure 10.3. The 53.5% case exhibits qualitatively similar behavior as the 51.62% case, however, at even lower interface velocity values. This is because more tellurium is segregated over the same period of time due to a larger driving force. This accumulates more tellurium in front of the growing interface, which in turn suppresses the solidification temperature more significantly. This effect is clear from the location and shape of the interface in Figure 10.4. The interface is not only lower than the zero tellurium case, it is more deformed than both the zero and 51.62% case. This is because more tellurium has accumulated. There is a slight spike of velocities near the end of 20 hours; unlike the control case, however, this is a consequence of changes in the interface shape since it has not reached the top of the ampoule.

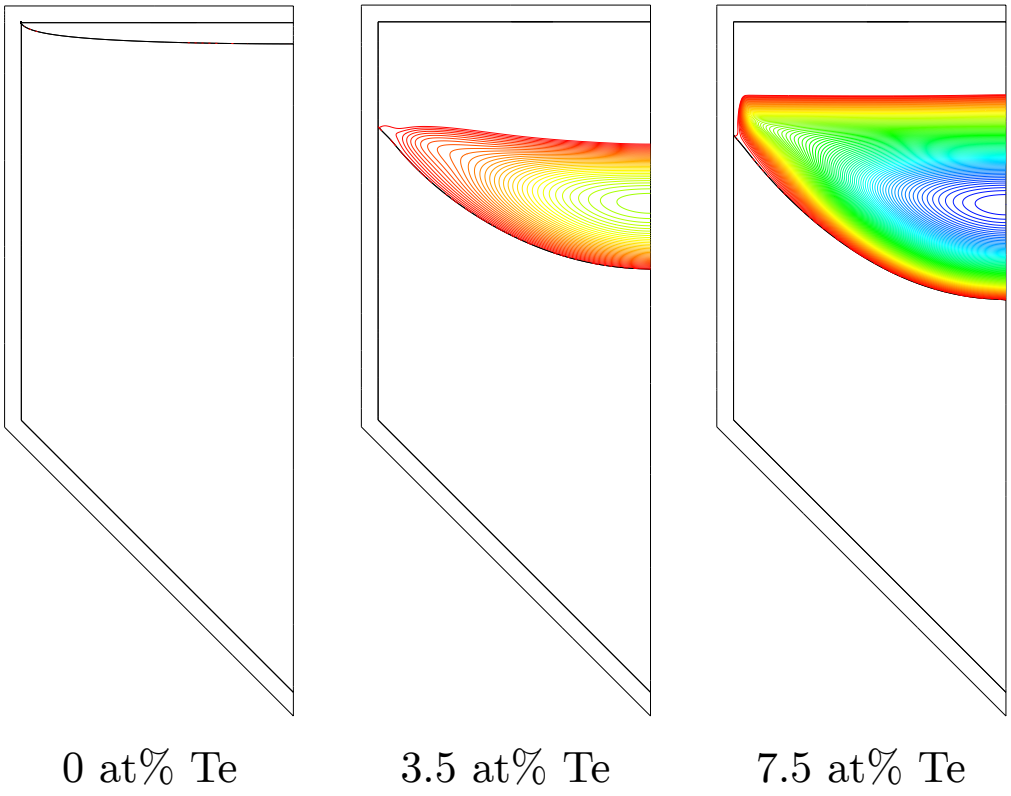

Figure 10.4: Contour plots of the supercooling after 22 hours of growth under steady conditions for varying levels of tellurium. $\Delta T_{min} = -9.95$ K, $\Delta T_{max} = 0$ K.

The average interface velocity calculated from the 53.5% case is 0.473 mm/hr. Although the exact velocity of the experimental result is not known, and compounded by the influence of rotation, the approximate 2.5 mm bands over the course of 5 hours suggests the interface moved at an average velocity of 0.5 mm/hr. The computational results are within 0.06% of the estimated experimental value, suggesting that the incorporation of tellurium leads to a reduction of interface velocities. Moreover, this quantitative agreement provides evidence that the model is accurately representing the growth phenomena in the real system.

Zinc composition

In order to also assess the influence of the rotation schedule on the zinc composition within the solid, a simulation was performed tracking the zinc in the solid [37] while turning rotation on and off. As this is the first time zinc has been incorporated into the current model, it warrants a brief discussion.

The movement of zinc within the liquid and solid is governed by the following differential equations:

$$\frac{\partial C_l}{\partial t} + \mathbf{u} \cdot \nabla C_l = D_l \nabla^2 C_l \tag{10.1}$$

$$\frac{\partial C_s}{\partial t} = D_s \nabla^2 C_s \tag{10.2}$$

where C_l and C_s represent the zinc composition in the liquid and the solid, and D_l and D_s represent the diffusion coefficient of zinc in the liquid and the solid, respectively. The diffusion coefficient of zinc in solid CZT has been experimentally found to be within the range of 1×10^{-13} and $1 \times 10^{-15}\mathrm{m}^2/\mathrm{s}$ [142]. However, such small values require intense mesh refinement and an increase in the number of unknowns. To circumvent a computationally expensive simulation, the solid state diffusion constant is artificially increased to 1×10^{-12} m^2/s. Although this may slightly overestimate the diffusion, any gradients observed in the simulation will more pronounced in the real system.

Segregation of zinc is represented by a flux balance across the interface:

$$D_l \mathbf{n} \cdot \nabla C_l - D_s \mathbf{n} \cdot \nabla C_s = -C_l(1 - k_p)\mathbf{n} \cdot \dot{\mathbf{x}}. \tag{10.3}$$

The flux of zinc generated by segregation is linearly dependent on the interface growth velocity, $\dot{\mathbf{x}}$, and the segregation coefficient, k_p. The discontinuous concentration profile is accounted for by the following equation:

$$C_s = k_p C_l. \tag{10.4}$$

Lastly, a no-flux condition is applied to all ampoule walls and the centerline that ensures mass is conserved within the system:

$$D_l \mathbf{n} \cdot \nabla C_l = 0. \tag{10.5}$$

Unfortunately, tellurium was not also incorporated into the model, so no thermodynamic effects on the solidification effects were included. Zinc only was computed in both the liquid and the solid. While this renders this validation effort marginally useful, we believe the qualitative effects of transport can still be addressed. Two full cycles were repeated.

A plot of the zinc composition in the crystal after two full cycles is shown in figure 10.5. Regions of ACRT and steady growth are accentuated by the superposition of the interface boundaries after each segment. It is clear there are compositional discrepancies between each region, although they are not as dramatic as the experimental results. This could be for a variety of reasons: growth in the simulation began past the cone region while the experiment occurred within the cone region; an idealized diffusion constant was used in the solid, overestimating the spread; and the exclusion of tellurium precluded the thermodynamic effects on the solidification temperature.

The computed centerline zinc concentration in the solid is shown in figure 10.6, which is compared to a steady (non-ACRT) case under the same conditions. With all other parameters held the same, there is a clear difference between the two cases. As the system begins to grow from a zero-velocity initial condition, the depletion of zinc results in a dramatic dip in the concentration. This is reflected in both patterned and steady cases. However, after the interface has translated to approximately 4 cm, ACRT is turned on, at which point the zinc composition spikes. The initial cycles of ACRT sweep higher concentrated fluid towards the interface, which solidifies into the crystal. As the melt becomes more homogenized with respect to concentration, the

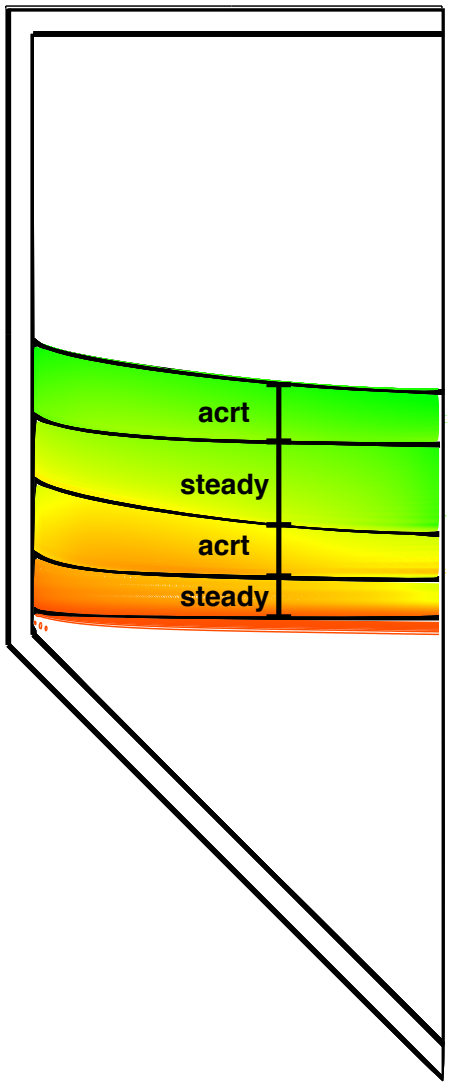

Figure 10.5: Simulation results of the zinc composition in the grown crystal for the patterned experiment. Red corresponds to high concentrations of 0.135 at% and green corresponds to low concentrations of 0.105 at%.

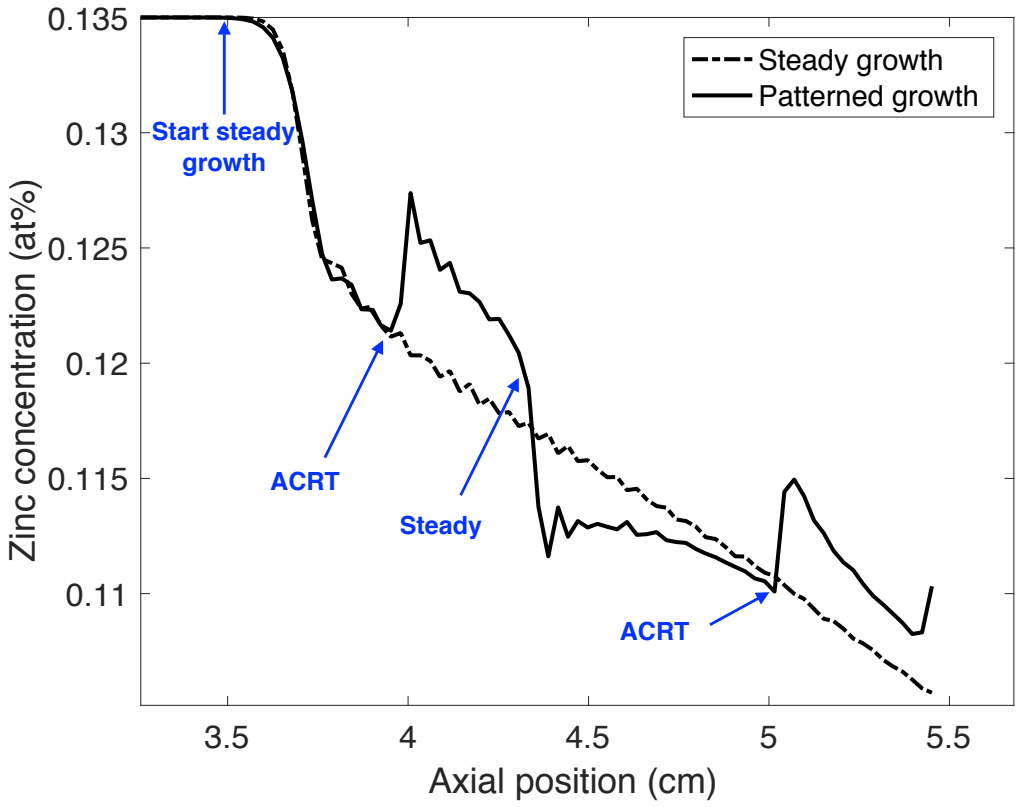

Figure 10.6: Centerline composition of zinc in the grown solid during growth with periods of rotation (indicated by the solid black line) compared to a steady growth without rotation (indicated by the dashed line).

average composition near the interface decreases from its peak value. This is reflected in the decreasing composition at later points during the ACRT regime. Once rotation is stopped and steady growth is allowed to proceed, the composition drops precipitously as a depletion boundary layer is formed in front of the interface. This is exacerbated as time goes on, and reflected in the steadily decreasing composition in the solid. This phenomena is repeated during the second cycle.

These values are not quantitatively compared to the experimental results due to the lack of faithful representation of the real system. However, consistent between the experiment and the simulations are the sharp increases in concentration that occurs at the onset of ACRT. We believe this is an important finding to not only explain the experimental results but also provide evidence that ACRT is effective in transporting zinc throughout the system. This can be improved upon in the future by incorporating the effects of zinc and tellurium simultaneously, and repeating the experiment in the cone region to assess the quantitative behavior.

10.2 Metric validation

Validation of the metric proposed in Chapter 8 is required if it is to be applied to other systems as a measure of schedule effectiveness. The M-value is a measure of the overall stability of the interface throughout multiple cycles of ACRT. Although the metric has no ability to quantitatively predict the number and size of inclusions experimentally, it can differentiate between better and worse rotation schedules. From the statistical analysis proposed in Chapter 8, an ideal rotation schedule was identified that promoted the most interface stability with respect to time and space. This schedule, which will be referred to as RS-A, is summarized in Table 10.1 and resulted in a positive M-value. This indicates that majority of growth was spent under fully stabilizing conditions. This is compared to a second rotation schedule, RS-B, which has a negative M-value, suggesting that the majority of growth was spent under destabilizing conditions. Analysis of the M-value alone would suggest that RS-A would yield better material quality compared to RS-B.

These schedules were also applied experimentally to the WSU system in two separate runs, and were analyzed via infrared microscopy to indicate the size and distribution

Table 10.1: Summary of rotation schedules tested in the model with respective M-values calculated via algorithm 1 after 1.6 hours of simulation.

Rotation Schedule	Ω_0 (RPM)	τ_a (s)	τ_r(s)	τ_d(s)	$\tau_s(s)$	M-value after 1.6 hours	Mean inclusion diameter (μm)
RS-A	3	60	15	60	60	0.1168	2.74
RS-B	10	60	0	30	0	-0.5773	3.38

of tellurium particles. The mean diameter of inclusion sizes for each experiment is summarized in Table 10.1. The RS-A boule yielded smaller inclusions than the RS-B boule (2.74 μm versus 3.38 μm, respectively). With smaller inclusions, material grown under RS-A is likely to yield better detector performance. This promising result leads us to believe the metric has value in at least predicting the relative efficacy of rotation schedules.

There are several improvements that can be made to the metric in order to account for the kinetic effects of cellular growth. A critical timescale can be identified and incorporated into the model such that it can better predict how likely the system is to entrap liquid, and computations of the cellular morphology can predict the relative size of inclusions. This and other areas for future work is discussed in the next chapter.

Chapter 11

Conclusion

11.1 Summary

The research presented in this thesis is aimed at improving the quality of detector-grade cadmium zinc telluride crystals grown via the vertical gradient freeze (VGF) method. The application of the accelerated crucible rotation technique (ACRT) during growth is posited to increase the monocrystallinity, improve the distribution of species, and of particular interest, reduce the size and density of inclusions. These inclusions, which act as electron traps in the device, are consequences of a morphological instability caused by the presence of constitutional supercooling. From its conception in the 1970s, ACRT has been proven to be an effective means of improving material quality via disruption of the solute and thermal fields, and much of the important rotational fluid phenomena have been identified both through experimental and computation means. However despite this progress, how ACRT works to reduce inclusions is still not well understood, and few guidelines exist to aid the selection of rotation schedules that will produce high quality material. Through computational modeling of the continuum transport of the VGF-ACRT system, we have developed an improved understanding of why ACRT works and how we can best design the system properties to improve material quality.

For the first time, we have shown that the segregation of tellurium drives constitutional supercooling during the growth of CZT. We propose a hypothetical mechanism to explain that, while ACRT does not eliminate the supercooling, it periodically sweeps it away, allowing the interface to re-stabilize and heal itself. With these periodic changes,

the interface velocity can become significantly altered, which can have a detrimental impact on the interface stability. While some recommendations specific to this system are presented here to manage the interface velocity, future work should be directed towards preventing large oscillations in the local interface velocity for this and other systems. In particular, weaker flows, reduced thermal gradients, and slower translation rates correlate with improvements in the interface stability. While the conventional intent to homogenize the melt is feasible through fast rotation rates, these rotation schedules yield poor interface stability and should be avoided. An optimal rotation schedule is identified for the current system that has been corroborated by preliminary experimental results, but future work should assess these recommendations in the context of different physical properties and geometries. Ideally, the large-scale testing of rotation schedules with various properties can yield recommendations in terms of dimensionless groups such as the rotational Reynolds number, the Rayleigh number, and the Ekman timescale. These recommendations can then be applied to almost any system with any material of interest.

In Chapter 2, we describe the equations and boundary conditions that govern the momentum, heat, and solute transport within the VGF-ACRT system. Heat transfer is determined by a translating furnace profile that is based on the experimental set up of our collaborators at Washington State University (WSU). Thermal gradients drive melt convection due to buoyancy forces which interact with the azimuthal flow specified by an time-dependent rotation schedule along solid boundaries. Segregation and transport of tellurium is, for the first time, incorporated into the model, with a polynomial fit to the liquidus line on the phase diagram. The combined thermal and solute effects determine the melt-crystal interface shape. The model is solved through implementation of a Galerkin finite element software, Cats2D, the details of which are described in Chapter 3.

In Chapter 4, we describe the results of a base case transient calculation of growth under steady (i.e. non-ACRT) conditions. A steady-state initial condition is presented from which all transient calculations begin. A sample transient calculation is presented with an emphasis on the effects of segregation and constitutional supercooling during growth, the latter of which can be calculated from the phase diagram. Although the current model does not have the capacity to compute the cellular morphology, the

presence of constitutional supercooling is an indicator that an instability will occur.

A similar analysis is performed in Chapter 5 for a base case transient calculation under ACRT. The five operating parameters of a rotation schedule are discussed (maximum rotation rate, acceleration interval, constant interval, deceleration interval, and stopped interval) and applied to the VGF system. The flow field is discussed, with particular attention paid to the azimuthal flow field during the four intervals of rotation. Ekman transport and Taylor-Görtler instabilities, which are consequences of acceleration and deceleration, are introduced and visualized with contours of the streamlines.

Under steady conditions, segregation of tellurium at the melt-crystal interface causes the accumulation of tellurium in the melt near the growing interface as discussed in Chapter 6. This drives constitutional supercooling, which begins to appear just minutes into growth, and increases in size and magnitude as growth continues. To the best of our knowledge, this is the first calculation showing that segregation of tellurium drives constitutional supercooling in the growth of CZT. In contrast to conventional wisdom, ACRT does not homogenize the solute field in the melt, and strong concentration gradients still persist. We show that supercooled fluid is not eliminated under ACRT but is rather periodically swept across the interface in phase with the Ekman flow. This preliminary but important result motivated the need for better quantification of the dynamics along the interface.

To address this need, a metric based on the seminal work by Mullins and Sekerka [126] is developed to assess the overall stability of the interface at a particular point in time. Plotting this value versus time elucidates how each regime works to ameliorate or exacerbate the supercooling. Periods of acceleration work to sweep supercooled fluid away from the interface, improving the stability of the interface. However, as the system decelerates, supercooled fluid is brought back to propagate across the interface, momentarily exacerbating the overall stability.

This metric is employed in a comparison of two rotation schedules determined using recommendations put forth by Capper [51]. One rotation schedule is designed to maximize the convective transport with a maximum rotation rate of 30 RPM. The other is designed to stabilize the Ekman flow a maximum rotation rate of 3 RPM. After 20 minutes of ACRT, the flow maximizing schedule yields a mostly homogeneous distribution of tellurium in the melt, indicating the schedule is effective in its purpose. However,

assessment of the supercooling indicates that the region of supercooled fluid is larger in strength and size as compared to the steady case. This is because the strong flows not only homogenize the solute field, but also the strongly mix the thermal field such that the supercooling conditions are exacerbated. On the other hand, the Ekman stabilizing schedule barely adjusts the solute and supercooling fields from the steady case. While the Ekman flow is not strong enough to homogenize the solute and thermal fields, it is still effective in sweeping away supercooled material from the interface during periods of acceleration. A plot of the metric described in Chapter 6 confirms this, with longer periods of stabilization in the Ekman stabilizing case.

These interesting results prompt further investigation of the influence of rotation schedules. In Chapter 8, we present a new iteration on the metric described in Chapter 6 that incorporates the temporal changes in stability into a single value. This value is applied to a factorial design of experiments that elucidate the relative importance of the maximum rotation rate over all other schedule parameters. Further study is performed systematically varying the maximum rotation rate, the time to accelerate, and the time at constant rotation over a range of values. Dramatic changes in the interface velocity are found with higher rotation rates which worsen the interface stability. These calculations support the selection of rotation rates that are strong enough to enhance Ekman flow during acceleration, but are not so strong they significantly alter the interface velocities.

Further optimization of the system through changes in the applied furnace profile is discussed in Chapter 9. In place of the realistic furnace profile presented in Chapter 2, a linear profile is applied to the system. The effects of a low furnace gradient (10 K/cm) are compared to a high gradient (30 K/cm). Under steady conditions, the high gradient system results in higher local interface velocities due to a stronger driving force for growth. Subsequently, the magnitude of supercooled fluid within the system is worsened. Under ACRT, the Ekman flow in the high gradient case is not fully developed due to strong underlying buoyancy-driven flows. This paired with higher interface velocities yield worse supercooling. While these results suggest that lower thermal gradients result in improved supercooling, a similar effect can also be achieved by simply lowering the translation rate.

Lastly, two validation experiments are discussed in Chapter 10. First, model and experimental results are compared for a growth that periodically turned rotation on

and off. Our model is able to verify the actual growth rate found in the experiment and qualitatively predict the patterns of zinc distribution within the solid. Second, the metric's experimental utility is assessed through the comparison of two rotation schedules. The metric accurately predicted an improvement in tellurium inclusion particle size. Although the metric has no ability to determine the size or density of inclusions, these preliminary results suggest it is useful in assessing the relative efficacy of rotation schedules.

11.2 Directions for future work

11.2.1 Additional tests

There are a whole host of additional tests that can be made with model as it currently stands. First, much longer simulations should be tested to observe the longer term effects of rotation on the interface velocities, supercooling, and stability. Additionally, as motivated in Chapter 10, both zinc and tellurium should be incorporated into the model simultaneously. This way the thermodynamic effects of tellurium can be faithfully represented with the tracking of zinc in the solid. This will allow for better comparison to experimental results.

A different initial condition for growth should be selected, ideally within the cone region. While nucleation is not feasible to represent for the reasons mentioned in Chapter 2, beginning with a centimeter or two of growth within the cone region would more faithfully represent the real system. This will be particularly useful for comparison of zinc distributions with experimental results, as the dynamics within the cone region can be quite different than in the bulk.

Ideally, the factorial analysis will be replicated for various geometries, viscosities, densities, and thermal gradients. While somewhat computationally expensive, this would provide a large data set from which more generalized trends can be extrapolated. Instead of plotting the metric against the maximum rotation rate, it can be plotted against the rotational Reynolds number to see if a scaling analysis will pop out. Similarly, the metric can be plotted against a dimensionless time period scaled with the Ekman timescale to see if the behaviors collapse to a simple scaling analysis. If successful, this would provide recommendations that would be generalizable to all systems and

materials, which would be incredibly powerful. If nothing else, it would provide more insight into the nonlinear effects of ACRT.

11.2.2 Modeling the dynamics of a cellular interface

The current model as described by Chapter 2 does not have the ability to compute the cellular morphology that is likely to occur in the presence of constitutional supercooling. Thus far, any amount of supercooled melt is interpreted as a proxy for an instability. Moreover, the metric defined in Chapter 8 excludes any notion of the timescales over which cells develop or shrink.

A cellular interface can be computed with the incorporation of the Gibbs-Thomson effect, which incorporates curvature effects to the determination of the interface. This is accomplished by replacing the isotherm condition in Equation 2.14 with the following:

$$T_{int} = T_0 + mC + T_0\Gamma(\mathscr{H}), \tag{11.1}$$

where T_0 is the melting temperature of the planar interface without compositional effects, m is the local slope of the liquidus curve, and Γ is the surface free energy that is a function of $\mathscr{H}$, the mean curvature of the interface. If the interface height is described by $h(x,t)$, the mean curvature of the interface is defined by

$$\mathscr{H} \equiv \frac{1}{2}\frac{d^2h/dx^2}{[1+(dh/dx)^2]^{3/2}}. \tag{11.2}$$

Additionally, the mesh must be discretized such that the element size is smaller than the anticipated wavelength of the cell. Ungar and Brown [5, 143–145] performed idealized growth calculations for a lead-antimony system where they were able to calculate the steady state morphology of the interface under destabilizing conditions. The interface morphology at various thermal gradients is reproduced in Figure 11.1, where deep cells can be observed at lower thermal gradients. From these calculations it is easy to predict the inevitable pinching off of cells to form pockets of trapped liquid. This liquid solidifies into the aforementioned inclusions that are deleterious to detector performance.

This work can be made relevant to the WSU system by first reproducing the Ungar and Brown results with properties of CZT to identify the conditions under which the cells grow. However, these steady state calculations do not capture the transient effects

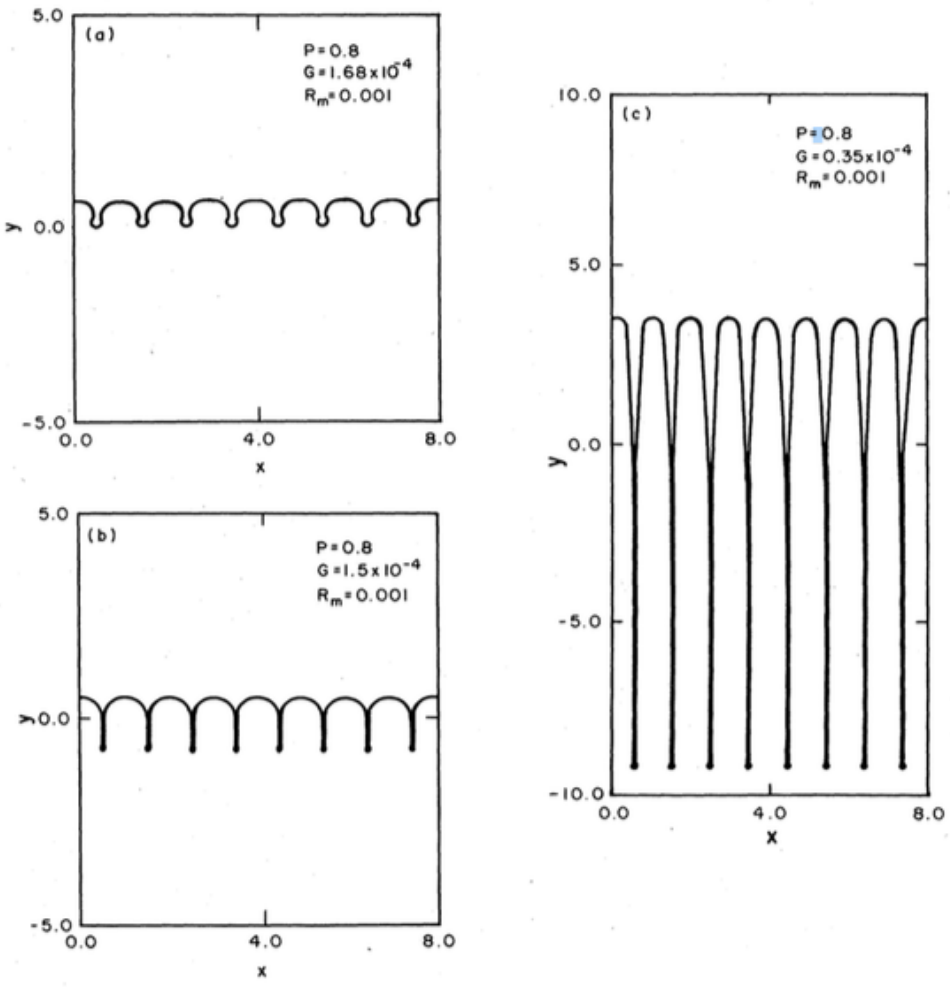

Figure 11.1: Sample interface shapes for various thermal gradients (G) applied to the system. Reproduced from [5].

of a cell developing; rather they are representative of the interface shape within a fixed thermal and concentration gradient. (As a note, they also neglect flow.) To observe a response in the interface morphology to changing solute fields, far-field boundary conditions can impose a time-dependent forcing function on the concentration field. The transient adjustment of the concentration field and the subsequent impact on the interface morphology can be measured, and a timescale of cellular growth development can be inferred for a given change in concentration fields. This calculation can provide an estimate for how long a cell takes to return to a planar configuration given a step change in concentration gradients. We learned in Chapter 6 that the Ekman flow can momentarily improve the stabilizing conditions along the interface; with a healing timescale in hand, we can better assess the length of time to allow for this Ekman flow.

Then, to mimic the effect that ACRT has on the solute field, a sinusoidal forcing function can be applied as a far-field boundary condition. This will allow for the real-time visualization of cells forming and retreating. We can apply various rotation schedules by way of different forcing functions to observed how the interface responds over many cycles of ACRT, and make a stronger connection between the changes in supercooled material and the propensity of the interface to form inclusions.

11.2.3 Metric development

With the timescale information determined by the calculations in the above section in hand, we can further refine the metric presented in Chapter 8. Currently, the metric counts one time step at $> 85\%$ stable able to re-stabilize one time step at $<15\%$ stable. This is problematic if say, the cell takes on the order of 15 seconds to develop, but a minute to recede back to a planar configuration. Moreover, it neglects any cells that are too far gone to be re-stabilized. A new metric can take these arguments into account by ensuring that the amount of time spent under stabilizing or destabilizing conditions is compared to the timescales of cell growth and abatement.

11.2.4 Influence of tellurium composition

Tellurium is added in excess amounts for its ability to improve the resistivity of the detector. However, the connection between the amount of excess tellurium and the

propensity of the system to form inclusions is not well understood. This was briefly touched upon in Chapter 10 where the local interface velocity was suppressed with higher tellurium compositions. However, it would be instructive to assess the interface stability at various tellurium compositions, particularly with the incorporation of the Gibbs-Thomson effect to compute cellular interfaces. Higher concentration values would yield stronger driving forces for segregation, which would likely lead to stronger concentration gradients. This line of thinking would suggest that higher tellurium compositions would result in worse supercooling. However, as discussed in Chapter 10, an increase in tellurium concentration actually retards the local growth velocity, which would reduce the driving force for segregation. This could, in turn, reduce the accumulation of tellurium and yield less severe supercooling. This would have an opposite effect than anticipated, and perhaps, under certain conditions, be encouraged. Further studies of varied tellurium compositions with ACRT would elucidate if the suppression of the growth velocity would be enough to counteract the increased effect of segregation.

11.2.5 Changes in interface concavity

The concavity of the interface is primarily determined by the thermal field and the ratio of thermal conductivities as described in Chapter 4. For the current system, this creates a concave interface. This concavity is exacerbated during growth as tellurium accumulates and suppresses the solidification temperature. When ACRT is applied, the Ekman flow can draw from some of the superheated fluid that sits near the centerline to sweep away the supercooled material, thus promoting a stable interface. However, these effects all change with a change in interface concavity.

A change in interface shape is likely to have a multitude of effects. A convex interface is known to reduce the number of grains [146] by propagating any defects from the interface outwards towards the sidewalls. Indeed, much effort has been applied to designing growth systems that promote a concave interface [147–154]. Additionally, a change in concavity reverses the radial thermal gradient near the interface, which drives one large clockwise vortex within the melt. This alone changes the solute transport within the system, particularly under steady conditions. With the current system, the two-vortex structure creates a strong shear layer through which only diffusion of species is allowed. This problem is eliminated with a convex interface.

As tellurium segregates next to a convex interface, it is likely to accumulate in different locations than in the current system. This can cause suppression of the interface velocity at different locations and result in a new distribution of supercooled fluid. This could accumulate near the side walls, in which case inclusions would be more likely to form near the walls. Alternatively, it could accumulate near the center, which would further influence the concavity of the interface.

The dynamics of the the flow and solidification would also be highly affected under ACRT. The Ekman flow near the solid liquid interface during acceleration, which is responsible for sweeping away supercooled material, is counteracted by the underlying buoyant flows in the current system. With a rearrangement of buoyant flows, however, Ekman flow during acceleration may only be strengthened. Additionally, the Ekman flows that occur during deceleration are enhanced by the underlying buoyant flows in the current system. Again, with a reversal of underlying flows this could ameliorate the destabilization that is observed during deceleration. This could improve outcomes for ACRT.

However, promoting a concave interface is challenging to accomplish via rearrangement of the furnace profile alone. Often alternate structures or materials must be added to the system, like a cold finger [38] to draw heat fluxes downward. Moreover, segregation of tellurium will continue to occur and suppress the solidification temperature. This, along with ACRT's tendency to flatten any interface shape, will likely decrease the convexity of the interface further, and significant changes will have to be applied to maintain a fully convex shape throughout growth.

The factorial analysis presented in Chapter 8 could be repeated with an artificial change in interface shape. This would elucidate the combined effect of the interface shape with rotation schedule parameters. It is likely that the change in concavity will also alter the system's response in interface velocity, which may have a significant impact on the propensity to form inclusions. As in-situ assessments of the interface becomes more ubiquitous with neutron imaging [155], tailored recommendations can be made that incorporate accurate interface shapes.

References

[1] Amlan Datta, Santosh Swain, Yunlong Cui, Arnold Burger, and Kelvin Lynn, "Correlations of Bridgman-Grown CdZnTe Properties with Different Ampoule Rotation Schemes", *Journal of Electronic Materials* **42**(11), pp. 3041–3053 (2013).

[2] U. N. Roy, S. Weiler, and J. Stein, "Growth and interface study of 2 in diameter CdZnTe by THM technique", *Journal of Crystal Growth* **312**(19), pp. 2840–2845 (2010).

[3] V. N. Guskov and A. D. Izotov, "Thermodynamic principles of the synthesis of CdTe, ZnTe, and CdZnTe solid solutions", *Inorganic Materials* **44**(13), pp. 1409 (2008).

[4] Nan Zhang, Andrew Yeckel, Arnold Burger, Yunlong Cui, Kelvin G. Lynn, and Jeffrey J. Derby, "Anomalous segregation during electrodynamic gradient freeze growth of cadmium zinc telluride", *Journal of Crystal Growth* **325**(1), pp. 10–19 (2011).

[5] Lyle H. Ungar and Robert A. Brown, "Cellular interface morphologies in directional solidification. The one-sided model", *Physical Review B* **29**(3), pp. 1367–1380 (1984).

[6] Jesse Lee, "Fulfilling a Promise from Prague", *White House Blog* (2010), https://www.whitehouse.gov/blog/2010/04/06/fulfilling-a-promise-prague.

[7] Gunnar Maehlum, "Integrated Detector Electronics (IDEAS) ASIC product update", *Integrated Detector Electronics AS* (2014), https://www.slideshare.net/maehlum/ideas-atesspresentation.

[8] GE Healthcare, "CZT Technology: Fundamentals and Applications (White Paper)", (2009), http://bit.ly/2njm6CD.

[9] Francesco Nudi and Giuseppe Biondi-Zoccai, "Cadmium-zinc-telluride myocardial perfusion imaging: The dream of a single test gets nearer", *Journal of Nuclear Cardiology* , pp. 1–5 (2017).

[10] Ali B. Alenazy, R. Glenn Wells, and Terrence D. Ruddy, "New solid state cadmium-zinc-telluride technology for cardiac single photon emission computed tomographic myocardial perfusion imaging", *Expert Review of Medical Devices* **14**(3), pp. 213–222 (2017).

[11] T. E Schlesinger, J. E Toney, H Yoon, E. Y Lee, B. A Brunett, L Franks, and R. B James, "Cadmium zinc telluride and its use as a nuclear radiation detector material", *Materials Science and Engineering: R: Reports* **32**(4), pp. 103–189 (2001).

[12] Jack F. Butler, Boris A. Apotovsky, A. Niemela, and Heikki Sipila, "Sub-keV resolution detection with CdZnTe detectors", volume 2009 , pp. 121–128. Proc. SPIE 2009, X-Ray Detector Physics and Applications II (1993).

[13] Oluseyi Babalola, *Surface and bulk defects in cadmium zinc telluride and camium manganese telluride crystals*, PhD thesis Graduate School of Vanderbilt University Nashville, TN (2009).

[14] F. P. Doty, H. B. Barber, F. L. Augustine, J. F. Butler, B. A. Apotovsky, E. T. Young, and W. Hamilton, "Pixellated CdZnTe detector arrays", *Nuclear Instruments and Methods in Physics Research Section A: Accelerators, Spectrometers, Detectors and Associated Equipment* **353**(1), pp. 356–360 (1994).

[15] F. P. Doty, J. F. Butler, J. F. Schetzina, and K. A. Bowers, "Properties of CdZnTe crystals grown by a high pressure Bridgman method", *Journal of Vacuum Science & Technology B* **10**(4), pp. 1418–1422 (1992).

[16] Fred H. Pollak, "Semiconductors and Semimetals, Vol. 13 (Book Review)", *Physics Today* **31**(8), pp. 53 (1978).

[17] E. Raiskin and J.F. Butler, "CdTe low level gamma detectors based on a new crystal growth method", *IEEE Transactions on Nuclear Science* **35**(1), pp. 81–84 (1988).

[18] E. Saucedo, P. Rudolph, and E. Dieguez, "Modified Bridgman growth of CdTe crystals", *Journal of Crystal Growth* **310**(7), pp. 2067–2071 (2008).

[19] S. Sen, W. H. Konkel, S. J. Tighe, L. G. Bland, S. R. Sharma, and R. E. Taylor, "Crystal growth of large-area single-crystal CdTe and CdZnTe by the computer-controlled vertical modified-Bridgman process", *Journal of Crystal Growth* **86**(1), pp. 111–117 (1988).

[20] P. Rudolph, "Fundamental studies on Bridgman growth of CdTe", *Progress in Crystal Growth and Characterization of Materials* **29**(14), pp. 275–381 (1994).

[21] Tao Wang, Wanqi Jie, Jijun Zhang, Ge Yang, Dongmei Zeng, Yadong Xu, Shuying Ma, Hui Hua, and Ke He, "Study on the behaviors of impurities in cadmium zinc telluride", *Journal of Crystal Growth* **304**(2), pp. 313–316 (2007).

[22] Percy W. Bridgman, "Crystals and their manufacture" (1931), US 1793672 A.

[23] Carmen Stelian and Thierry Duffar, "Modeling effects of solute concentration in Bridgman growth of cadmium zinc telluride", *Journal of Crystal Growth* **446**, pp. 42–49 (2016).

[24] R. Triboulet, "Fundamentals of the CdTe and CdZnTe bulk growth", *Physica Status Solidi (c)* **2**(5), pp. 1556–1565 (2005).

[25] R. Triboulet, Y. Marfaing, A. Cornet, and P. Siffert, "Undoped highresistivity cadmium telluride for nuclear radiation detectors", *Journal of Applied Physics* **45**(6), pp. 2759–2765 (1974).

[26] P. Rudolph, S. Kawasaki, S. Yamashita, S. Yamamoto, Y. Usuki, Y. Konagaya, S. Matada, and T. Fukuda, "Attempts to growth of undoped CdTe single crystals with high electrical resistivity", *Journal of Crystal Growth* **161**(1), pp. 28–33 (1996).

[27] Peter Rudolph and Manfred Mhlberg, "Basic problems of vertical Bridgman growth of CdTe", *Materials Science and Engineering: B* **16**(1), pp. 8–16 (1993).

[28] Peter Rudolph, "Melt growth of II-VI compound single crystals", *Recent Development of Bulk Crystal Growth, Research Signpost, Trivandrum, India* (1998).

[29] P. Rudolph, "Non-stoichiometry related defects at the melt growth of semiconductor compound crystals a review", *Crystal Research and Technology* **38**(7-8), pp. 542–554 (2003).

[30] P. Rudolph, U. Rinas, and K. Jacobs, "Systematic steps towards exactly stoichiometric and uncompensated CdTe Bridgman crystals", *Journal of Crystal Growth* **138**(1), pp. 249–254 (1994).

[31] V. Babentsov, J. Franc, A. Fauler, M. Fiederle, and R. B. James, "Distribution of zinc, resistivity, and photosensitivity in a vertical Bridgman grown CdZnTe ingot", *Journal of Crystal Growth* **310**(15), pp. 3482–3487 (2008).

[32] Satheesh Kuppurao, Simon Brandon, and Jeffrey J. Derby, "Modeling the vertical Bridgman growth of cadmium zinc telluride II. Transient analysis of zinc segregation", *Journal of Crystal Growth* **155**(12), pp. 103–111 (1995).

[33] Satheesh Kuppurao, Simon Brandon, and Jeffrey J. Derby, "Modeling the vertical Bridgman growth of cadmium zinc telluride I. Quasi-steady analysis of heat transfer and convection", *Journal of Crystal Growth* **155**(12), pp. 93–102 (1995).

[34] Qiang Xiao, Satheesh Kuppurao, Andrew Yeckel, and Jeffrey J. Derby, "On the effects of ampoule tilting during vertical Bridgman growth: three-dimensional computations via a massively parallel, finite element method", *Journal of Crystal Growth* **167**(1), pp. 292–304 (1996).

[35] Krisanne Edwards and Jeffrey J. Derby, "Understanding horizontal Bridgman shelf growth of cadmium telluride and cadmium zinc telluride. I. Heat and momentum transfer", *Journal of Crystal Growth* **179**(1), pp. 120–132 (1997).

[36] Krisanne Edwards, Simon Brandon, and Jeffrey J. Derby, "Transient effects during the horizontal Bridgman growth of cadmium zinc telluride", *Journal of Crystal Growth* **206**(1), pp. 37–50 (1999).

[37] Lisa Lun, Andrew Yeckel, Prodromos Daoutidis, and Jeffrey J. Derby, "Decreasing lateral segregation in cadmium zinc telluride via ampoule tilting during vertical Bridgman growth", *Journal of Crystal Growth* **291**(2), pp. 348–357 (2006).

[38] Nan Zhang, Andrew Yeckel, and Jeffrey J. Derby, "Maintaining convex interface shapes during electrodynamic gradient freeze growth of cadmium zinc telluride using a dynamic, bell-curve furnace profile", *Journal of Crystal Growth* **355**(1), pp. 113–121 (2012).

[39] U. N. Roy, A. Burger, and R. B. James, "Growth of CdZnTe crystals by the traveling heater method", *Journal of Crystal Growth* **379**, pp. 57–62 (2013).

[40] Jeffrey H. Peterson, Michael Fiederle, and Jeffrey J. Derby, "Analysis of the traveling heater method for the growth of cadmium telluride", *Journal of Crystal Growth* **454**, pp. 45–58 (2016).

[41] Esteban Meca and Mathis Plapp, "Phase-Field Study of the Cellular Bifurcation in Dilute Binary Alloys", *Metallurgical and Materials Transactions A* **38**(7), pp. 1407–1416 (2007).

[42] Yiwen Ma and Mathis Plapp, "Phase-field simulations and geometrical characterization of cellular solidification fronts", *Journal of Crystal Growth* **385**, pp. 140–147 (2014).

[43] A. E. Bolotnikov, N. Abdul-Jabber, S. Babalola, G. S. Camarda, Y. Cui, A. Hossain, E. Jackson, H. Jackson, J. James, K. T. Kohman, A. Luryi, and R. B. James, "Effects of Te inclusions on the performance of CdZnTe radiation detectors", In *2007 IEEE Nuclear Science Symposium Conference Record* volume 3 , pp. 1788–1797 (2007).

[44] W. A Tiller, K. A Jackson, J. W Rutter, and B Chalmers, "The redistribution of solute atoms during the solidification of metals", *Acta Metallurgica* **1**(4), pp. 428–437 (1953).

[45] H.J Scheel, "Accelerated crucible rotation: A novel stirring technique in high-temperature solution growth", *Journal of Crystal Growth* **13-14**, pp. 560–565 (1972).

[46] E. O. Schulz-Dubois, "Accelerated crucible rotation: Hydrodynamics and stirring effect", *Journal of Crystal Growth* **12**(2), pp. 81–87 (1972).

[47] Fritz V. Wald and Richard O. Bell, "Natural and forced convection during solution growth of CdTe by the Traveling Heater Method (THM)", *Journal of Crystal Growth* **30**(1), pp. 29–36 (1975).

[48] R. U. Bloedner and P. Gille, "Growth of HgCdTe single crystals by travelling heater method under accelerated crucible rotation conditions", *Journal of Crystal Growth* **130**(1), pp. 181–187 (1993).

[49] P. Capper, J. J. G. Gosney, and C. L. Jones, "Application of the accelerated crucible rotation technique to the Bridgman growth of CdHgTe: Simulations and crystal growth", *Journal of Crystal Growth* **70**(1), pp. 356–364 (1984).

[50] P. Capper, J. J. Gosney, C. L. Jones, and I. Kenworthy, "Bridgman growth of CdHgTe using ACRT", *Journal of Electronic Materials* **15**(6), pp. 371–376 (1986).

[51] P. Capper, J. C. Brice, C. L. Jones, W. G. Coates, J. J. G. Gosney, C. Ard, and I. Kenworthy, "Interfaces and flow regimes in ACRT grown CdHgTe crystals", *Journal of Crystal Growth* **89**(23), pp. 171–176 (1988).

[52] P. Capper, "The role of accelerated crucible rotation in the growth of HgCdTe and CdTe/CdZnTe", *Progress in Crystal Growth and Characterization of Materials* **28**(12), pp. 1–55 (1994).

[53] J. C. Brice, P. Capper, C. L. Jones, and J. J. G. Gosney, "ACRT: A review of models", *Progress in Crystal Growth and Characterization* **13**(3), pp. 197–229 (1986).

[54] James Coble Brice, *Crystal growth processes*, Halsted Press (1986).

[55] Peter Capper and Evgeny Zharikov, "24 - Oscillatory-Driven Fluid Flow Control during Crystal Growth from the Melt", In Peter Rudolph, editor, *Handbook of Crystal Growth* , pp. 951–993. Elsevier Boston 2nd edition (2015).

[56] C. W Lan and J. H Chian, "Effects of ampoule rotation on vertical zone-melting crystal growth: steady rotation versus accelerated crucible rotation technique (ACRT)", *Journal of Crystal Growth* **203**(12), pp. 286–296 (1999).

[57] Andrew Yeckel, F. Patrick Doty, and Jeffrey J. Derby, "Effect of steady crucible rotation on segregation in high-pressure vertical Bridgman growth of cadmium zinc telluride", *Journal of Crystal Growth* **203**(12), pp. 87–102 (1999).

[58] Andrew Yeckel and Jeffrey J. Derby, "Effect of accelerated crucible rotation on melt composition in high-pressure vertical Bridgman growth of cadmium zinc telluride", *Journal of Crystal Growth* **209**(4), pp. 734–750 (2000).

[59] Liu Xiaohua, Jie Wanqi, and Zhou Yaohe, "Numerical analysis of CdZnTe crystal growth by the vertical Bridgman method using the accelerated crucible rotation technique", *Journal of Crystal Growth* **219**(12), pp. 22–31 (2000).

[60] Xiaohua Liu, Wanqi Jie, and Yaohe Zhou, "Numerical analysis on HgCdTe growth by ACRT-VBM", *Journal of Crystal Growth* **209**(4), pp. 751–762 (2000).

[61] Andrew Yeckel and Jeffrey J. Derby, "Buoyancy and rotation in small-scale vertical Bridgman growth of cadmium zinc telluride using accelerated crucible rotation", *Journal of Crystal Growth* **233**(3), pp. 599–608 (2001).

[62] Seung Jae Moon, Charn-Jung Kim, and Sung Tack Ro, "Effects of buoyancy and periodic rotation on the melt flow in a vertical Bridgman configuration", *International Journal of Heat and Mass Transfer* **40**(9), pp. 2105–2113 (1997).

[63] Y. C. Liu, B. Roux, and C. W. Lan, "Effects of cycle patterns of accelerated crucible rotation technique (ACRT) on the flows, interface, and segregation in vertical Bridgman crystal growth", *International Journal of Heat and Mass Transfer* **50**(2526), pp. 5031–5040 (2007).

[64] Liu Juncheng, "ACRT forced convection and its effects on solute segregation and heat and mass transfer during single crystal growth", *Crystal Research and Technology* **43**(4), pp. 396–408 (2008).

[65] M. P. Bellmann, E. A. Meese, and L. Arnberg, "Effect of accelerated crucible rotation on the segregation of impurities in vertical Bridgman growth of multicrystalline silicon", *Journal of Crystal Growth* **318**(1), pp. 239–243 (2011).

[66] Liying Yin, Wanqi Jie, Tao Wang, Boru Zhou, and Fan Yang, "The transport phenomena during the growth of ZnTe crystal by the temperature gradient solution growth technique", *Journal of Crystal Growth* **461**, pp. 16–24 (2017).

[67] Liying Yin, Wanqi Jie, Tao Wang, Boru Zhou, Fan Yang, and Ruihua Nan, "The Effects of ACRT on the Growth of ZnTe Crystal by the Temperature Gradient Solution Growth Technique", *Crystals* **7**(3), pp. 82 (2017).

[68] V. E Distanov and A. G Kirdyashkin, "The influence of accelerated crucible rotation mode on the melt temperature field in the Stockbarger technique", *Journal of Crystal Growth* **222**(3), pp. 607–614 (2001).

[69] T. Wang, W.-Q. Jie, Y.-D. Xu, G.-Q. Zha, and L. Fu, "Characterization of CdZnTe crystal grown by bottom-seeded Bridgman and Bridgman accelerated crucible rotation techniques", *Transactions of Nonferrous Metals Society of China (English Edition)* **19**(SUPPL. 3), pp. s622–s625 (2009).

[70] Amlan Datta, Santosh Swain, Yunlong Cui, Arnold Burger, and Kelvin Lynn, "Preliminary results on Bridgman grown CdZnTe detector crystals assisted by ampoule rotation", volume 8507. Proc. SPIE 8507, Hard X-Ray, Gamma-Ray, and Neutron Detector Physics XIV, 850711 (2012).

[71] K. Mochizuki, K. Masumoto, and K. Miyazaki, "Melt growth of CdTe single crystals with controlled deviation from stoichiometry", *Materials Letters* **6**(4), pp. 119–122 (1988).

[72] A. Haloui, Y. Feutelais, and B. Legendre, "Experimental study of the ternary system CdTeZn", *Journal of Alloys and Compounds* **260**(12), pp. 179–192 (1997).

[73] A. Laugier, "Thermodynamics and phase diagram calculations in II-VI and IV-VI ternary systems using an associated solution model", *Revue de Physique Applique* **8**(3), pp. 259–270 (1973).

[74] Dirk de Nobel, *Phase Equilibria and Semiconducting Properties of Cadmium Telluride*, S.L. N.D. (1958).

[75] Jacques Steininger, Alan J. Strauss, and Robert F. Brebrick, "Phase Diagram of the ZnCdTe Ternary System", *Journal of The Electrochemical Society* **117**(10), pp. 1305–1309 (1970).

[76] T.-C. Yu and R. F. Brebrick, "The Hg-Cd-Zn-Te phase diagram", *Journal of Phase Equilibria* **13**(5), pp. 476–496 (1991).

[77] J. H. Greenberg, "P-T-X phase equilibrium and vapor pressure scanning of non-stoichiometry in CdTe", *Journal of Crystal Growth* **161**(14), pp. 1–11 (1996).

[78] P. M. Gresho and R. L. Sani, *Incompressible flow and the finite element method. Volume 1: Advection-diffusion and isothermal laminar flow*, John Wiley and Sons, Inc. (1998).

[79] P. M. Gresho, "Some Interesting Issues in Incompressible Fluid Dynamics, Both in the Continuum and in Numerical Simulation", In John W. Hutchinson and Theodore Y. Wu, editors, *Advances in Applied Mechanics* volume 28 , pp. 45–140. Elsevier (1991).

[80] B. A. Finlayson and L. E. Scriven, "The method of weighted residuals and its relation to certain variational principles for the analysis of transport processes", *Chemical Engineering Science* **20**(5), pp. 395–404 (1965).

[81] Alan Jeffrey and Hui Hui Dai, *Handbook of Mathematical Formulas and Integrals*, Academic Press (2008).

[82] K. N. Christodoulou and L. E. Scriven, "Discretization of free surface flows and other moving boundary problems", *Journal of Computational Physics* **99**(1), pp. 39–55 (1992).

[83] P. Hood, "Frontal solution program for unsymmetric matrices", *International Journal for Numerical Methods in Engineering* **10**(2), pp. 379–399 (1976).

[84] Andrew Yeckel and Ralph T. Goodwin III, "Cats2d (Crystalization and Transport Simulator) User Manual" (2003).

[85] Parthiv Daggolu, Andrew Yeckel, Carl E. Bleil, and Jeffrey J. Derby, "Thermal-capillary analysis of the horizontal ribbon growth of silicon crystals", *Journal of Crystal Growth* **355**(1), pp. 129–139 (2012).

[86] David Gasperino, Mary Bliss, Kelly Jones, Kelvin Lynn, and Jeffrey J. Derby, "On crucible effects during the growth of cadmium zinc telluride in an electrodynamic gradient freeze furnace", *Journal of Crystal Growth* **311**(8), pp. 2327–2335 (2009).

[87] D.J. Gasperino, *Modeling of transport processes during solution, melt and colloidal crystal growth, Ph.D. Thesis.*, PhD thesis University of Minnesota Minneapolis, MN (2008).

[88] Arun Pandy, Andrew Yeckel, Michael Reed, Csaba Szeles, Marc Hainke, Georg Mller, and Jeffrey J. Derby, "Analysis of the growth of cadmium zinc telluride in an electrodynamic gradient freeze furnace via a self-consistent, multi-scale numerical model", *Journal of Crystal Growth* **276**(1), pp. 133–147 (2005).

[89] Yutao Tao, Andrew Yeckel, and Jeffrey J. Derby, "Analysis of particle engulfment during the growth of crystalline silicon", *Journal of Crystal Growth* **452**, pp. 1–5 (2016).

[90] Yutao Tao, Tina Sorgenfrei, Thomas Jaub, Arne Croll, Christian Reimann, Jochen Friedrich, and Jeffrey J. Derby, "Particle engulfment dynamics under oscillating crystal growth conditions", *Journal of Crystal Growth* **468**, pp. 24–27 (2017).

[91] Yutao Tao, Andrew Yeckel, and Jeffrey J. Derby, "Steady-state and dynamic models for particle engulfment during solidification", *Journal of Computational Physics* **315**, pp. 238–263 (2016).

[92] Jeffrey J. Derby, Yutao Tao, Christian Reimann, Jochen Friedrich, Thomas Jaub, Tina Sorgenfrei, and Arne Croll, "A quantitative model with new scaling for

silicon carbide particle engulfment during silicon crystal growth", *Journal of Crystal Growth* **463**, pp. 100–109 (2017).

[93] Zaoyang Li, Jeffrey H. Peterson, Andrew Yeckel, and Jeffrey J. Derby, "Analysis of the effects of a rotating magnetic field on the growth of cadmium zinc telluride by the traveling heater method under microgravity conditions", *Journal of Crystal Growth* **452**, pp. 17–21 (2016).

[94] Jeffrey H. Peterson, Andrew Yeckel, and Jeffrey J. Derby, "A fundamental limitation on growth rates in the traveling heater method", *Journal of Crystal Growth* **452**, pp. 12–16 (2016).

[95] Andrew Yeckel, Robert S. Feigelson, and Jeffrey J. Derby, "Analysis of scintillator crystal production via the edge-defined film-fed growth method", volume 88520V. Proc. SPIE 8852, Hard X-Ray, Gamma-Ray, and Neutron Detector Physics XV (2013).

[96] Jeffrey J. Derby, Nan Zhang, and Andrew Yeckel, "Modeling insights on the melt growth of cadmium zinc telluride", *Journal of Crystal Growth* **379**, pp. 28–33 (2013).

[97] Nan Zhang, Hyun Gyoon Park, and Jeffrey J. Derby, "Simulation of heat transfer and convection during sapphire crystal growth in a modified heat exchanger method", *Journal of Crystal Growth* **367**, pp. 27–34 (2013).

[98] Andrew Yeckel and Jeffrey J. Derby, "The prospects for traveling magnetic fields to affect interface shape in the vertical gradient freeze growth of cadmium zinc telluride", *Journal of Crystal Growth* **364**, pp. 133–144 (2013).

[99] Thomas J. R. Hughes, *The Finite Element Method: Linear Static and Dynamic Finite Element Analysis*, Courier Corporation (2012).

[100] Ivo Babuka, "Error-bounds for finite element method", *Numerische Mathematik* **16**(4), pp. 322–333 (1971).

[101] O.A. Ladyzhenskaya, *The mathematical theory of viscous incompressible flow*, Gordon and Breach, (1963).

[102] Franco Brezzi, "On the existence, uniqueness and approximation of saddle-point problems arising from lagrangian multipliers.", *Analyse Numrique,* **8 (R2)**, pp. 129–151 (1974).

[103] D. N. Arnold, F. Brezzi, and M. Fortin, "A stable finite element for the stokes equations", *Calcolo* **21**(4), pp. 337–344 (1984).

[104] Eugene L. Allgower and Kurt Georg, *Numerical Continuation Methods: An Introduction*, Springer Science & Business Media (2012).

[105] Dale R. Durran, "The Third-Order Adams-Bashforth Method: An Attractive Alternative to Leapfrog Time Differencing", *Monthly Weather Review* **119**(3), pp. 702–720 (1990).

[106] Francis Bashforth and John Couch Adams, *An Attempt to Test the Theories of Capillary Action*, University Press (1883).

[107] Kai Diethelm, Neville J. Ford, and Alan D. Freed, "A Predictor-Corrector Approach for the Numerical Solution of Fractional Differential Equations", *Nonlinear Dynamics* **29**(1-4), pp. 3–22 (2002).

[108] S. F. Kistler and L. E. Scriven, "Coating Flows", In *Computational Analysis of Polymer Processing* , pp. 243–299. Springer, Dordrecht (1983).

[109] Kostas N. Christodoulou, Stephan F. Kistler, and P. Randall Schunk, "Advances in Computational Methods for Free-Surface Flows", In *Liquid Film Coating* , pp. 297–366. Springer, Dordrecht (1997).

[110] Ekman, V. W., "On the influence of the earth's rottaion on ocean currents", *Arkiv. Math. Astron. Physik* **2**(11) (1905).

[111] Harvey Philip Greenspan, *The theory of rotating fluids*, CUP Archive (1968).

[112] Alan J. Faller, "An experimental study of the instability of the laminar Ekman boundary layer", *Journal of Fluid Mechanics* **15**(4), pp. 560–576 (1963).

[113] Alan J. Faller and Robert E. Kaylor, "A Numerical Study of the Instability of the Laminar Ekman Boundary Layer", *Journal of the Atmospheric Sciences* **23**(5), pp. 466–480 (1966).

[114] Robert Kaylor and Alan J. Faller, "Instability of the Stratified Ekman Boundary Layer and the Generation of Internal Waves", *Journal of the Atmospheric Sciences* **29**(3), pp. 497–509 (1972).

[115] A. B. Arons, A. P. Ingersoll, and T. Green, "Experimentally Observed Instability of a Laminar Ekman Flow in a Rotating Basin", *Tellus* **13**(1), pp. 31–39 (1961).

[116] E. T. Eady, "Long Waves and Cyclone Waves", *Tellus* **1**(3), pp. 33–52 (1949).

[117] Olivier Czarny, Eric Serre, Patrick Bontoux, and Richard M. Lueptow, "Ekman vortices and the centrifugal instability in counter-rotating cylindrical Couette flow", *Theoretical and Computational Fluid Dynamics* **18**(2-4), pp. 151–168 (2004).

[118] Douglas K. Lilly, "On the Instability of Ekman Boundary Flow", *Journal of the Atmospheric Sciences* **23**(5), pp. 481–494 (1966).

[119] P. R. Tatro and E. L. Mollo-Christensen, "Experiments on Ekman layer instability", *Journal of Fluid Mechanics* **28**(3), pp. 531–543 (1967).

[120] Lord Rayleigh, "On the Dynamics of Revolving Fluids", *Proceedings of the Royal Society of London. Series A, Containing Papers of a Mathematical and Physical Character* **93**(648), pp. 148–154 (1917).

[121] A. Recktenwald, M. Lcke, and H. W. Mller, "Taylor vortex formation in axial through-flow: Linear and weakly nonlinear analysis", *Physical Review E* **48**(6), pp. 4444–4454 (1993).

[122] G. P. Neitzel and Stephen H. Davis, "Centrifugal instabilities during spin-down to rest in finite cylinders. Numerical experiments", *Journal of Fluid Mechanics* **102**, pp. 329–352 (1981).

[123] P. J. Blennerhassett and P. Hall, "Centrifugal instabilities of circumferential flows in finite cylinders: linear theory", *Proc. R. Soc. Lond. A* **365**(1721), pp. 191–207 (1979).

[124] C. David Andereck, S. S. Liu, and Harry L. Swinney, "Flow regimes in a circular Couette system with independently rotating cylinders", *Journal of Fluid Mechanics* **164**, pp. 155–183 (1986).

[125] Mia S. Divecha and Jeffrey J. Derby, "Analysis of the accelerated crucible rotation technique applied to the gradient freeze growth of cadmium zinc telluride", *Journal of Crystal Growth* **468**, pp. 630–634 (2017).

[126] W. W. Mullins and R. F. Sekerka, "Stability of a Planar Interface During Solidification of a Dilute Binary Alloy", *Journal of Applied Physics* **35**(2), pp. 444–451 (1964).

[127] W. W. Mullins and R. F. Sekerka, "Morphological Stability of a Particle Growing by Diffusion or Heat Flow", *Journal of Applied Physics* **34**(2), pp. 323–329 (1963).

[128] Sam R. Coriell and Robert L. Parker, "Stability of the Shape of a Solid Cylinder Growing in a Diffusion Field", *Journal of Applied Physics* **36**(2), pp. 632–637 (1965).

[129] S. H. Davis and T. P. Schulze, "Effects of flow on morphological stability during directional solidification", *Metallurgical and Materials Transactions A* **27**(3), pp. 583–593 (1996).

[130] Jeffrey J Hoyt, *Phase transformations*, McMaster University Bookstore Hamilton, Ontario, Canada (2011).

[131] J. S. Langer, "Instabilities and pattern formation in crystal growth", *Reviews of Modern Physics* **52**(1), pp. 1–28 (1980).

[132] R. F. Sekerka, "A Stability Function for Explicit Evaluation of the MullinsSekerka Interface Stability Criterion", *Journal of Applied Physics* **36**(1), pp. 264–268 (1965).

[133] R. Trivedi and W. Kurz, "Morphological stability of a planar interface under rapid solidification conditions", *Acta Metallurgica* **34**(8), pp. 1663–1670 (1986).

[134] Mia S. Divecha and Jeffrey J. Derby, "Towards optimization of ACRT schedules applied to the gradient freeze growth of cadmium zinc telluride", *Journal of Crystal Growth* **480**, pp. 126–131 (2017).

[135] P. Capper, J. E. Harris, E. O'Keefe, C. L. Jones, C. K. Ard, P. Mackett, and D. Dutton, "Bridgman growth and assessment of CdTe and CdZnTe using the accelerated crucible rotation technique", *Materials Science and Engineering: B* **16**(1), pp. 29–39 (1993).

[136] R. J. Lingwood, "An experimental study of absolute instability of the rotating-disk boundary-layer flow", *Journal of Fluid Mechanics* **314**, pp. 373–405 (1996).

[137] Douglas C. Montgomery, *Design and analysis of experiments*, John Wiley & Sons Hoboken, NJ 6th ed edition (2005).

[138] Mia S. Divecha and Jeffrey J. Derby, "Mechanistic study of the accelerated crucible rotation technique applied to vertical Bridgman growth of cadmium zinc telluride", volume 103920T. Proc. SPIE 10392, Hard X-Ray, Gamma-Ray, and Neutron Detector Physics XIX (2017).

[139] Santosh K. Swain, Yunlong Cui, Amlan Datta, Sachin Bhaladhare, Manchanahalli Rohan Rao, Arnold Burger, and Kelvin G. Lynn, "Bulk growth of uniform and near stoichiometric cadmium telluride", *Journal of Crystal Growth* **389**, pp. 134–138 (2014).

[140] Santosh Swain, Jedidiah McCoy, and Kelvin Lynn, "Influence of accelerated crucible rotation on defect distribution and detector characteristics of melt grown CdZnTe (Conference Presentation)", volume 996806. Proc. SPIE 9968, Hard X-Ray, Gamma-Ray, and Neutron Detector Physics XVIII (2016).

[141] S. K. Swain, K. A. Jones, A. Datta, and K. G. Lynn, "Study of Different Cool Down Schemes During the Crystal Growth of Detector Grade CdZnTe", *IEEE Transactions on Nuclear Science* **58**(5), pp. 2341–2345 (2011).

[142] N. Aslam, E. D. Jones, T. C. Q. Noakes, J. B. Mullin, and A. F. W. Willoughby, "The diffusion of zinc in cadmium telluride", *Journal of Crystal Growth* **117**(1), pp. 249–253 (1992).

[143] Lyle H. Ungar and Robert A. Brown, "Cellular interface morphologies in directional solidification. II. The effect of grain boundaries", *Physical Review B* **30**(7), pp. 3993–3999 (1984).

[144] Lyle H. Ungar and Robert A. Brown, "Cellular interface morphologies in directional solidification. IV. The formation of deep cells", *Physical Review B* **31**(9), pp. 5931–5940 (1985).

[145] Lyle H. Ungar, Mark J. Bennett, and Robert A. Brown, "Cellular interface morphologies in directional solidification. III. The effects of heat transfer and solid diffusivity", *Physical Review B* **31**(9), pp. 5923–5930 (1985).

[146] John Joseph Gilman, *The art and science of growing crystals*, John Wiley & Sons (1963).

[147] Satheesh Kuppurao and Jeffrey J. Derby, "Designing thermal environments to promote convex interface shapes during the vertical Bridgman growth of cadmium zinc telluride", *Journal of Crystal Growth* **172**(34), pp. 350–360 (1997).

[148] Jeffrey H. Peterson and Jeffrey J. Derby, "An axial temperature profile curvature criterion for the engineering of convex crystal growth interfaces in Bridgman systems", *Journal of Crystal Growth* (2017).

[149] Nobuyuki Kobayashi and Tetsuya Arizumi, "The Numerical Analyses of the Solid-Liquid Interface Shapes during the Crystal Growth by the Czochralski Method", *Japanese Journal of Applied Physics* **9**(4), pp. 361 (1970).

[150] P. S. Dutta, K. S. Sangunni, H. L. Bhat, and Vikram Kumar, "Growth of gallium antimonide by vertical Bridgman technique with planar crystal-melt interface", *Journal of Crystal Growth* **141**(1), pp. 44–50 (1994).

[151] F. R. Szofran and S. L. Lehoczky, "A method for interface shape control during Bridgman type crystal growth of HgCdTe alloys", *Journal of Crystal Growth* **70**(1), pp. 349–355 (1984).

[152] Kenji Kitamura, Shigeyuki Kimura, and Kazushi Watanabe, "Control of interface shape by using heat reservoir in FZ growth with infrared radiation convergence type heater", *Journal of Crystal Growth* **57**(3), pp. 475–481 (1982).

[153] M. Pfeiffer and M. Muhlberg, "Interface shape observation and calculation in crystal growth of CdTe by the vertical Bridgman method", *Journal of Crystal Growth* **118**(3), pp. 269–276 (1992).

[154] T. Jasinski and A. F. Witt, "On control of the crystal-melt interface shape during growth in a vertical Bridgman configuration", *Journal of Crystal Growth* **71**(2), pp. 295–304 (1985).

[155] Anton S. Tremsin, Didier Perrodin, Adrian S. Losko, Sven C. Vogel, Takenao Shinohara, Kenichi Oikawa, Jeff H. Peterson, Chang Zhang, Jeffrey J. Derby, Alexander M. Zlokapa, Gregory A. Bizarri, and Edith D. Bourret, "In-Situ Observation of Phase Separation During Growth of CsLiLaBr:Ce Crystals Using Energy-Resolved Neutron Imaging", *Crystal Growth & Design* , pp. 1528–7505 (2017).

[156] Crystal Growth Laboratory, "CrysMAS User Manual and Tutorial" (2013), https://download.iisb.fraunhofer.de/downloads/Manual/index.html.

Appendix A

Furnace Profiling Experiments

A.1 Summary

The aim of this chapter is to discuss the furnace validation experiments that were performed to validate the furnace model created in CrysMAS, a finite volume furnace modeling software developed by the Fraunhofer institute. For details regarding the CrysMAS code, please refer to [156]. Agreement between the experiments and the CrysMAS model was found within 15%. With the model validated, data from the model were extracted to generate a piecewise polynomial fit that was applied as a radiative heat boundary condition to the Cats2D finite element model.

A.2 Experimental design

The furnace is a 43-zone Mellen cylindrical furnace depicted in Figure A.1. During growth, a charge of material is placed in the quartz ampoule, which is placed upon a pedestal connected to a motor that can drive rotation. Power is directed to each heating element, located along the side walls, until a prescribed set point next to the heating element is reached. The set points vary with time in order to encourage the directional solidification of material. Since the full transient evolution of the temperature within the furnace is logistically challenging to measure experimentally, the following approach was taken. The system was brought to a profile representative of one point in time during growth. With the furnace held fixed at this state, thermocouples were

lowered down inside the furnace with quartz tubes to guide them. The temperature was recorded at various axial and radial positions, with additional measurements taken between zones 8-34 where the growth occurs. This was performed first with an empty bore, i.e. the pedestal and ampoule were removed. The experiment was then repeated with the pedestal, ampoule, and a dummy charge of mullite placed inside the furnace in order to capture their influence on the radiative heat transport. Mullite was chosen as its thermal conductivity is similar to that of cadmium zinc telluride (4 W/mK versus 2 W/mK, respectively).

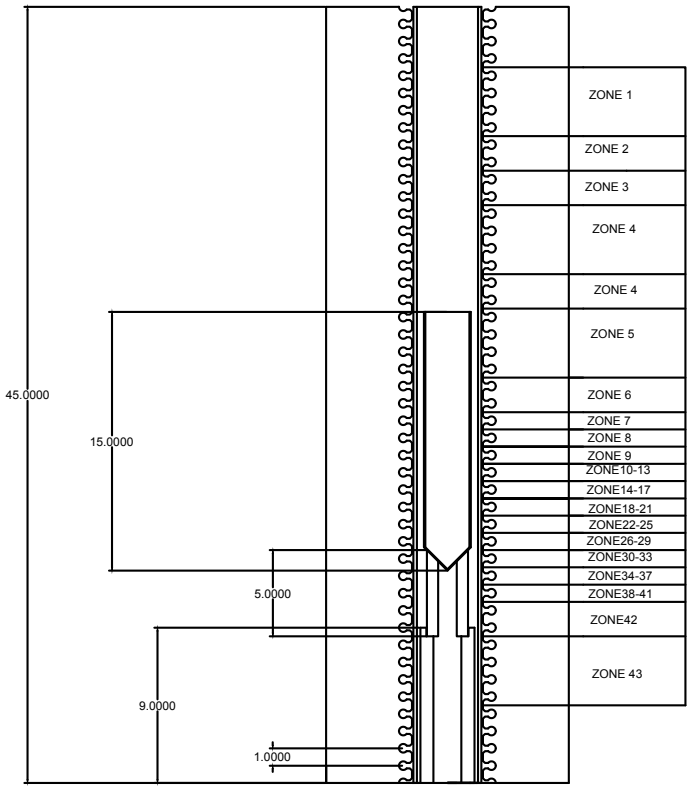

Figure A.1: Dimensions and geometry of the CrysMAS model used. All dimensions are in inches.

At each axial location, the thermocouples were allowed 5 minutes to equilibrate. This was found to be an acceptable time for the temperature to stop fluctuating within

0.1%. This was an appropriate amount of time given the following reasoning: the thermal diffusivity of the $\sim$ 2 mm stainless steel sheath that surrounds the thermocouple is approximately $\alpha = 3.36 \times 10^{-6}$ m^2/s. Heat transfer through this material via conduction has a characteristic timescale of $L^2/\alpha \sim 1$ second, indicating the choice of 5 minutes was more than enough time to equilibrate the thermocouples.

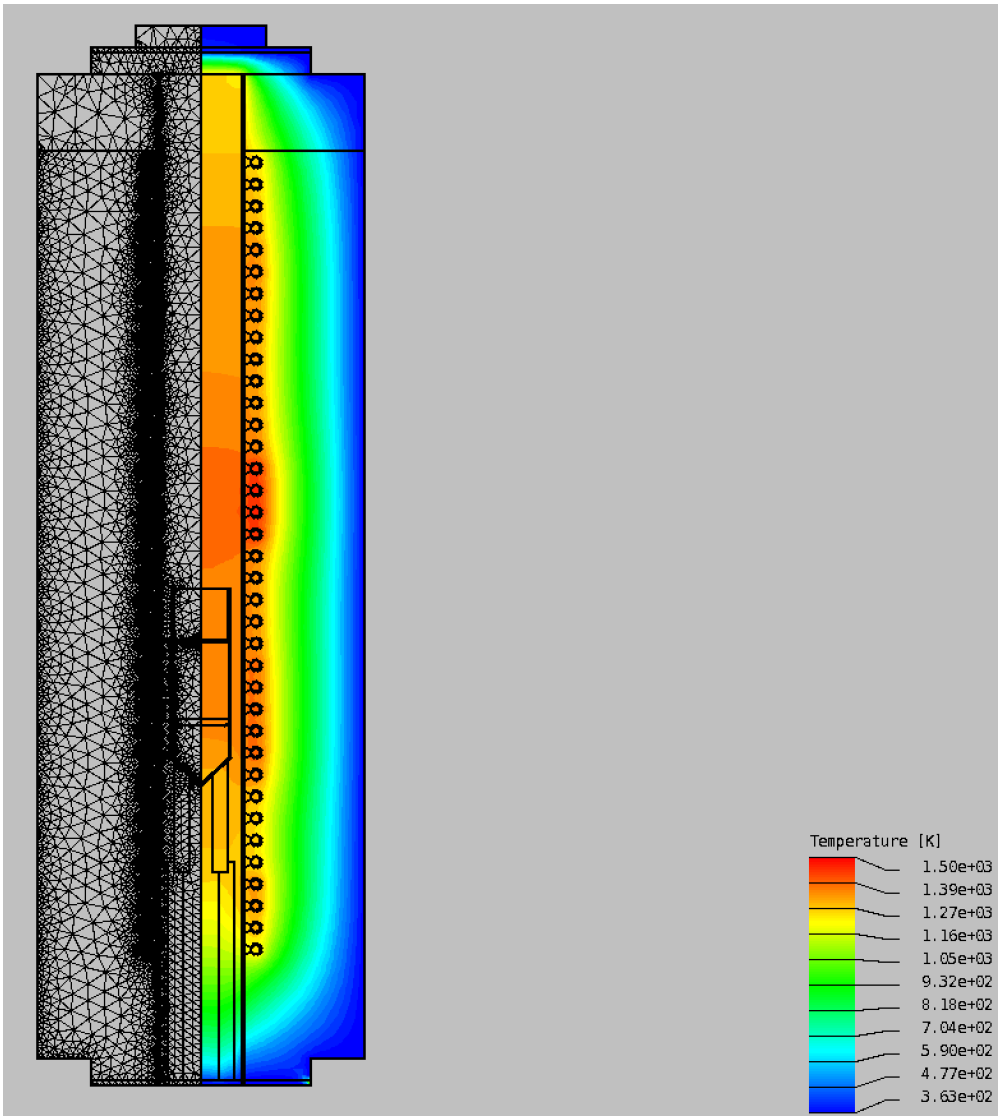

Figure A.2: Representative result of the temperature distribution in the furnace. Triangular mesh elements are shown on the left and temperature is shown on the right.

A.3 CrysMAS model

According to the experimental design, two CrysMAS models were created. The open bore model was comprised only of insulating elements and heating coils, which were assigned realistic material properties, available in [87]. From the open bore model, the mullite model was built by adding the pedestal, the ampoule, and mullite inside the ampoule to represent a charge. Realistic set points were specified in the system, and the power supplied to each heating element was adjusted until the set points were reached. This was solved iteratively via an enclosure method that ensured that all view factors from a given surface summed to one. A sample result of the unstructured mesh (left) and the temperature field (right) for a converged solution is shown in Figure A.2. Convergence was determined when the L2 norm of the residuum reached a tolerance of 1×10^{-12}.

Once the simulation converged, centerline data were extracted from the simulation and compared to the centerline data from the relevant experiment. Comparison for the open bore and mullite models are shown in Figures A.3 and A.4, respectively.

For the open bore experiment, there is a significant offset of around 40 K along the centerline between the experimental and CrysMAS calculations. This can be explained by a number of reasons. First, the material properties assigned to the model are estimations of the real values. For example, the thermal properties for the insulating material may have changed over the course of the furnace's lifetime. Additionally, the thermal field is very sensitive to changes in the physical locations of the set point thermocouples in the experiment. If these were moved even a few millimeters, it could change the power supplied to the heating elements dramatically. Moreover, the model did not incorporate the effect of moving the thermocouples throughout the experiment, which is sure to adjust the radiative heat transfer depending on its location. While we did our best to estimate the actual location of the thermocouple within the furnace, error on the order of ± 1 cm is introduced, which also is likely to explain the offset in temperatures.

However, we are ultimately not concerned with a temperature offset since we will extracting a temperature gradient and translating it in time. Thus, what is more important is good congruence between the temperature gradient within the growth region

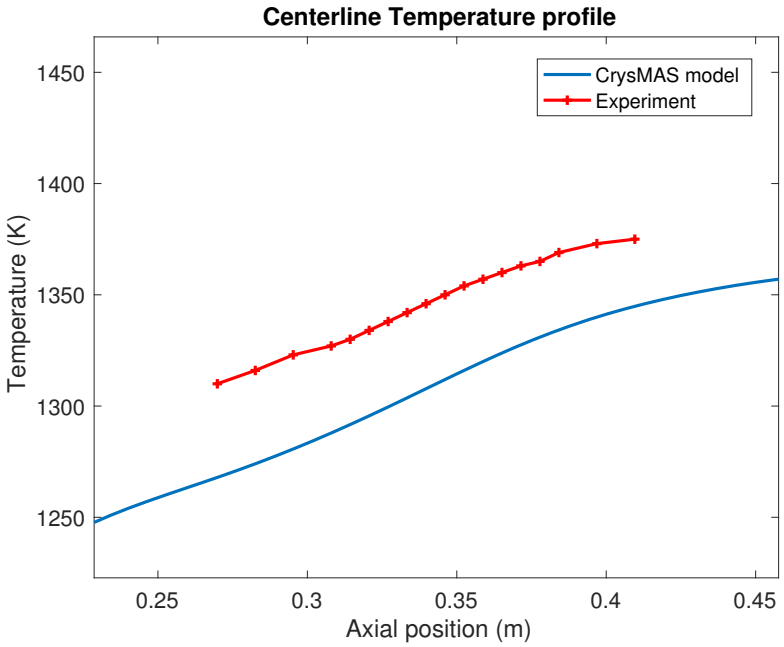

Figure A.3: Temperature versus axial position at the centerline for the experiment (red) versus the CrysMAS model (blue) for the open bore experiment.

(approximately between 0.35 and 0.4 m in axial position). For the open bore experiment, a gradient of 5.0 K/cm was found experimentally within the growth region. For the simulation, a gradient of 5.5 K/cm was calculated, which is within 10% of the experimental value.

For the mullite experiment, the same analysis applies. While a 20 K difference in the temperatures is observed, the gradients agreed within 15% in the growth region. The experimental gradient was found to be 8.2 K/cm, and the simulation yielded a gradient of 9.2 K/cm. We assert that this an acceptable representation of heat transfer within the furnace.

At this point, temperature data from the exterior edge of the ampoule are extracted. This profile is plotted in Figure A.5 against the piecewise polynomial fit to the data, described in Equation 2.18. Parameters extracted from the data are found in Table 4.2. This profile is translated in time and applied as a radiative heat boundary condition along the outer ampoule walls described by Equation 2.7. This is a simplified representation of the furnace dynamics since the gradients are likely to change throughout

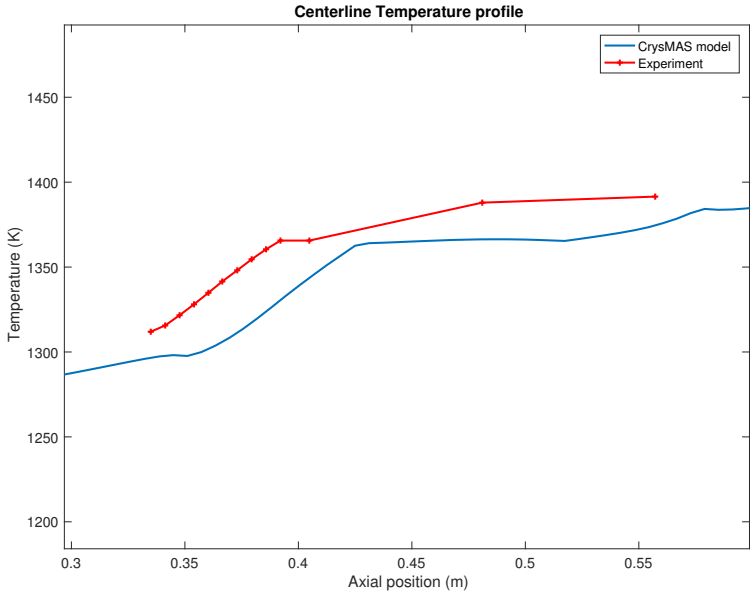

Figure A.4: Temperature versus axial position at the centerline for the experiment (red) versus the CrysMAS model (blue) for the mullite experiments

.

growth. However, few long-term calculations are performed such that this approximation is reasonable in representing the heat transfer within the range of a few hours.

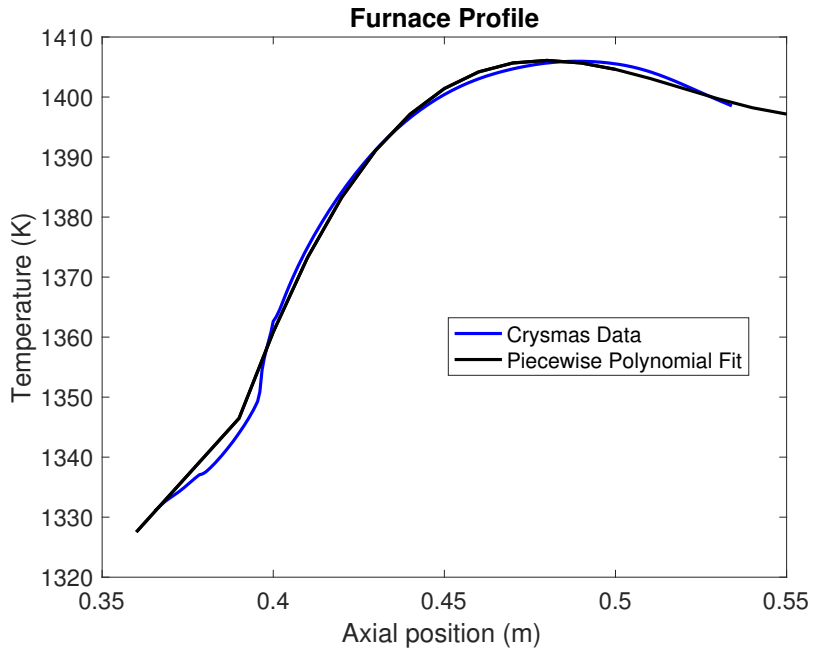

Figure A.5: Comparison of CrysMAS data extracted from the ampoule wall and polynomial fit described in Equation 2.18

.